EVALUATION OF 4D RECONSTRUCTION METHODS FOR GATED CARDIAC SPECT IMAGING IN OBESE PATIENTS

Sunita Sayeram

A dissertation submitted to the faculty of the University of North Carolina at Chapel Hill in partial fulfillment of the requirements for the degree of Doctor of Philosophy in the Department of Biomedical Engineering.

Chapel Hill
2009

Approved by:

David S. Lalush, Ph.D.

Marijana Ivanovic, Ph.D.

Arif Sheikh, M.D.

William P. Segars, Ph.D.

Carol Lucas, Ph.D.

ii

To the Eternal One

To my loving, ever-supportive parents
Rema and Krishna Sayeram

ABSTRACT

Sunita Sayeram
Evaluation of 4D Reconstruction Methods for
Gated Cardiac SPECT Imaging in Obese Patients
(Under the direction of David S. Lalush)

The purpose of this study is to evaluate 4D reconstruction methods for the processing of gated cardiac single photon emission computed tomography (SPECT) images from obese patients. Gated SPECT on obese patients is extremely noisy and often clinically useless; it is hypothesized that 4D reconstruction methods may help. The methods compared are the ordered-subsets expectation-maximization (OS-EM) algorithm with a 3D Gaussian filter, OS-EM with a 3D Gaussian combined with a time-domain Butterworth filter, and the rescaled block-iterative maximum *a posteriori* (RBI-MAP) algorithm with Gibbs priors for spatial and time-domain smoothing. Clinical gated SPECT data were used to derive a table of Tc-99m tetrofosmin activity uptake ratios. Moderately and morbidly obese male and female phantom models were created for the 4D NURBS-based Cardiac Torso (NCAT) phantom, and mild and severe motion defects were generated in addition to a normal heart model. A blood pool phantom study enabled optimization of reconstruction parameters for the methods so they result in similar noise statistics in the heart. Poisson noise was added to the projection data (including the effects of detector response, attenuation and scatter) generated from the phantoms. The noisy phantom and patient projection data were reconstructed with the three methods, and imported onto the clinical workstations, to be analyzed with the Quantitative Gated

SPECT (QGS) software. Quantitative parameters (chamber volumes) were recorded for the phantom and patient data. Statistical analysis led to the conclusion that OS-EM with 4D filtering was markedly different, a result confirmed in the normal phantom models, with better quantitation. Visually, RBI-MAP appeared to result in smoother, more realistic cardiac motion. A preference study was performed with four physicians who read the patient images using QGS and rated them on a 7-point scale to indicate which method most improved their confidence in the diagnoses. The one-way ANOVA showed no significant difference in preference for the processing methods. The conclusion is that the choice of reconstruction method may make more of a difference in patients with greater heart motion, and that the OS-EM method with 4D filtering may have an advantage over the other methods when it comes to LV chamber volume quantification.

CONTENTS

LIST OF TABLES

LIST OF FIGURES

LIST OF ABBREVIATIONS

3D	Three-Dimensional
4D	Four-Dimensional
ANOVA	Analysis Of Variance
BMI	Body Mass Index
CAD	Coronary Artery Disease
CT	Computerized Tomography
ECG	Electrocardiogram
EDV	End-Diastolic Volume
EF	Ejection Fraction
ESV	End-Systolic Volume
FBP	Filtered Backprojection
FWHM	Full-width-at-half-maximum
HLA	Horizontal Long Axis
LV	Left Ventricle or Left Ventricular
MRI	Magnetic Resonance Imaging
OS-EM	Ordered-Subset-Expectation-Maximization
RBI-MAP	Rescaled Block-Iterative Maximum *a posteriori*
ROI	Region of Interest
SA	Short Axis
SPECT	Single Photon Emission Computed Tomography
VLA	Vertical Long Axis

LIST OF SYMBOLS

cm   centimeter

kg   kilogram

mCi   milliCurie

mL   milliliter

Tc-99m   Technetium-99m

Chapter 1

Introduction

1.1 Significance

Cardiovascular disease is the leading cause of death in North America, and it is very prevalent in the obese population. Obesity, defined as a body mass index (BMI) of 30 kg/m^2 or greater (*Bigaard et al.*), is fast reaching epidemic proportions in the U.S. with nearly 70% of adults being classified as obese or overweight compared with fewer than 25% around 40 years ago (*LavieMilani, 2003, Manson, 2003 #118*). Excessive weight is an established risk factor for cardiovascular disease, type 2 diabetes mellitus, osteoarthritis and several medical conditions, and can lead to premature mortality (*MansonBassuk, 2003*). With regards to cardiovascular disease, obese patients are more likely to be hypertensive than lean patients, leading to increased arterial pressure and increased risk of left ventricular hypertrophy. Obesity is proven to have adverse effects on both diastolic and systolic ventricular function (*LavieMilani, 2003*).

Early diagnosis of disease can improve the prognosis for the patient. Given the prevalence of obesity and its cardiovascular effects leading to premature mortality, obese patients make up increasing numbers of the population being evaluated for cardiovascular disease (CAD) with the aid of various imaging modalities. Myocardial single photon emission computed tomography (SPECT) is a technique frequently used to evaluate left ventricular (LV) perfusion, which with the addition of gating, can evaluate LV function as well.

Obesity causes some challenges in the interpretation of these studies. Hansen et al. (*Hansen et al.*)studied the effects of obesity (including patient weight and body surface area) on the accuracy of quantitative SPECT Thallium-201 (Tl-201) perfusion imaging, and found that the accuracy was significantly reduced. It has been suggested that the use of Technetium-99m (Tc-99m) agents may improve the accuracy of myocardial perfusion imaging. Prone imaging has been shown to reduce inferior wall attenuation artifacts, and results in improved specificity and accuracy for CAD diagnosis as compared to supine imaging (*Perault C, 1995*). There are also challenges from the artifacts produced by the excess soft-tissue attenuation in obese patients, which can affect the diagnostic accuracy of myocardial perfusion SPECT. An approach that minimizes the impact of soft-tissue attenuation by adding useful information for the interpretation of attenuation artifacts, is the technique of using echocardiography (ECG) to gate the SPECT acquisition (*Lima et al., 2003*). However, even with this technique, there are challenges due to the noisy nature of the images, which can reduce the utility of gated SPECT imaging in obese patients. This dissertation will explore the problem, and look at three-dimensional (3D) versus four-dimensional (4D) reconstruction methods for gated SPECT imaging of obese patients.

1.2 Organization

This dissertation is structured into five chapters, with subsections for each of the three main projects. Chapter Two covers background material introducing gated SPECT imaging and its techniques, the processing methods being evaluated, and tools that will be used to investigate the different methods. Chapter Three describes in detail the

experimental design and methodology for each of the projects. Chapter Four presents the results of the studies performed with the patient and simulated phantom data, with Chapter Five providing discussion and conclusions.

Chapter 2

Background

2.1 Basic SPECT Theory and Myocardial Imaging in Obese Patients

2.1.1 SPECT Imaging

The science of nuclear medicine involves the administration of radioactive-labeled pharmaceuticals which emit gamma rays or positrons from within the patient as they decay. The pharmaceuticals are chosen so as to concentrate the radioactivity within the organ of interest in the body. A position-sensitive gamma camera designed to record the decays can then be used to capture images of the distribution of the radionuclide within the patient. Single photon emission computed tomography (SPECT) and positron emission tomography (PET) are two broad classes of nuclear medicine imaging modalities.

SPECT employs gamma-ray emitting radionuclides, and is a tomographic mode of imaging where several equally spaced planar views are acquired from an 180° or 360° orbit as the detector moves around the patient. A lead collimator in front of the crystal limits the acceptance angle for photons hitting the detector. There is a scintillation event in the crystal for each photon that has an interaction with it, and the light produced is transmitted to the photomultiplier tubes via a light pipe, where amplification of the signal occurs in the form of tens to hundreds of thousands of electrons per gamma photon. Circuits for pulse-height analysis and positioning behind the photomultiplier tubes provide the energy and position information for each gamma ray interaction in the

detector. This information is then transmitted to the display and analysis station, the computer, for further processing of the multitude of planar views or projection data into cross-sectional images of the radioactivity distribution within the patient.
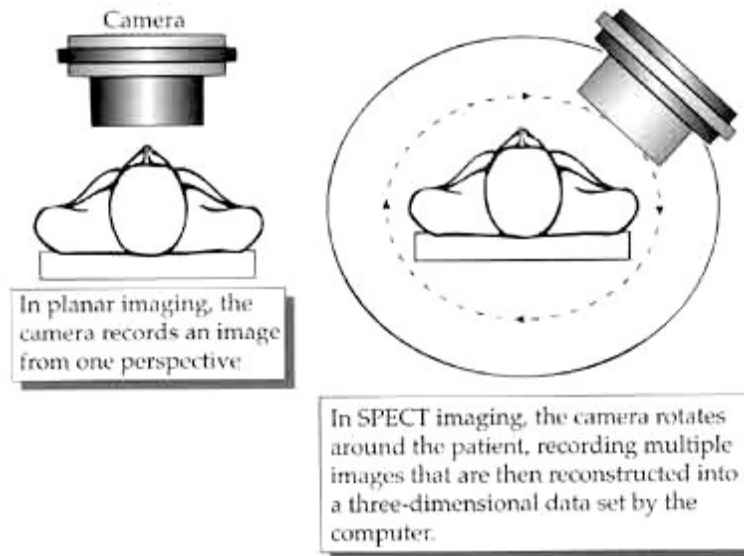
Figure 2.1: Image from http://us.myoview.com/tech/diagtest.html depicts SPECT imaging

There are three commonly used radioactive tracers for myocardial perfusion imaging. Thallium-201 has been available for over 25-30 years, and thus most experience has been gained with this tracer, but is not considered ideal because of a low gamma photopeak energy (69-83 keV) that limits resolution, and a relatively long half-life that limits the activity administered (*Higley et al., 1993*). Technetium-99m methoxyisobutylisonitrile (MIBI) and technetium-99m-1,2-bis[bis(2-ethoxyethyl) phosphino] ethane (tetrofosmin) have been introduced since then, and are used in an increasing proportion of studies (*Higley et al., 1993; Kapur et al., 2002*). The three tracers have been compared in clinical studies, and while some reported no significant differences between the tracers for summed uptake scores (*Reyes E, 2006*), others

5

discovered that the differing statuses of myocardial viability caused variations in both initial uptake and delayed retention of the tracers, and that tetrofosmin showed the least amount of tracer redistribution over time (*Takahashi et al., 1996*). Still others reported that overall image quality was superior with the technetium tracers which were deemed equal, and this was thought to be due to the reduced low-count artifact in the high-count resting images, and reduced attenuation artifact in women (*Kapur et al., 2002*). This study also confirmed higher heart-to-liver ratios for thallium than technetium, but reports conflicting results in other studies where the time of imaging was found to matter as it was noted that tetrofosmin has faster clearance from the liver than MIBI. The study reported higher heart-to-lung ratios for both technetium tracers over thallium, confirmed by other studies (*Manka-Waluch et al., 2006*) including preclinical trials in rat, guinea pig, and minipig (*Higley et al., 1993*). Ultimately, several studies concluded that technetium is preferred for obese patients, in women with large breasts, and in patients with impaired ventricular function where ECG-gated myocardial SPECT is indicated.

At UNC's Memorial Hospital, there is a choice between the Lantheus Medical Imaging product Cardiolite® labeled with Tc-99m sestamibi, or the GE Healthcare imaging agent Myoview® used with Tc-99m tetrofosmin, for gated myocardial SPECT imaging. The latter product is more often chosen for its rapid lung and liver clearance as compared to Tc-99m sestamibi, combined with a similar heart uptake and retention, and blood clearance kinetics, which offers the option of earlier imaging or higher quality images in earlier sessions (*Higley et al., 1993; Jain, 1999*). There currently is not a model for tetrafosmin uptake in the computerized phantom populations that have been used in myocardial imaging studies, so this dissertation aims to develop one.

2.1.2 ECG-Gated Myocardial SPECT Imaging

Left ventricular (LV) function is a very important diagnostic and prognostic indicator in patients with coronary artery disease (CAD). The assessment of LV volumes and LV ejection fraction (LVEF) is of great importance in the evaluation of CAD, and in determining the prognosis. LVEF is important enough to be used as an initial measure in clinical decision making, as well as being used to monitor LV remodeling after myocardial infarction, and to select patients for various kinds of therapies (*Baur, 2008; CacciabaudoSzulc, 2001*). Thus, evaluation of left ventricular function, particularly in quantifying the extent and degree of left ventricular defects, is crucial in providing the physician with the information needed to stratify risks and develop a therapeutic strategy best suited to the disease (*PaulNabi, 2004*).

There are several techniques that are of use in acquiring different facets of information about left ventricular function. Echocardiography, nuclear imaging, magnetic resonance imaging (MRI), computed tomography (CT) of the heart and contrast angiography, in particular, are useful in measuring left ventricular ejection fraction. Echocardiography is the most commonly used technique as it is widely available, costs the least, imparts no radiation, has moderate spatial resolution and is easily performed, but is highly operator and patient-dependent. LV function is frequently measured with three-dimensional structure extrapolated with measurements using two-dimensional techniques, which leads to sub-optimal accuracy and reproducibility for quantitative measurements. There are also acoustic window limitations and the analysis is highly subjective, which are all reasons that contribute to this technique being less than ideal (*Baur, 2008; CacciabaudoSzulc, 2001; Sciagra, 2007*). While the cardiac CT technique

measuring left ventricular function is very reproducible in 3D, acquired in 10-15 seconds and yields high spatial resolution, it comes with a considerable radiation exposure. MRI, by contrast, imparts no radiation to the patient and has good spatial resolution, but is more difficult to perform and more expensive, in addition to requiring long acquisition times (difficult for claustrophobic patients) and being contraindicated in patients with pacemakers and implantable cardioverter defibrillators (*Baur, 2008; Sciagra, 2007*). There are two main nuclear imaging techniques that can be used, radionuclide angiography being one, and gated myocardial SPECT being the other. First-pass radionuclide angiography (FPRNA) and equilibrium-gated radionuclide angiography (ERNA) are two of the former kind of technique used to measure left ventricular function. FPRNA is preferred for assessing peak-exercise ventricular function and measuring right ventricular function, while ERNA is an equilibrium technique considered to be the most accurate for estimating left ventricular systolic function. Gated myocardial SPECT imaging is the preferred imaging method for the simultaneous assessment of ventricular perfusion and function (*PaulNabi, 2004*). Gated SPECT is widely available and is considered the only technique that allows reliable evaluation of myocardial perfusion during dynamic exercise (*Sciagra, 2007*).

The stress technique used in the rest-stress study may involve either maximal dynamic exercise, which is physiological and provides hemodynamic data with prognostic value, or pharmacological stress using a vasodilator agent (like adenosine or dipyridamole) or beta-agonist, which is useful in patients with restricted exercise tolerance (*Prvulovich, 2006*). Commonly used rest-stress study protocols are shown in Figure 2.2, where the gated SPECT study is shown to be administered either after the rest

or the stress portion of the study, depending on the protocol used. Patients are imaged supine with arms raised above the head to avoid causing attenuation in lateral projections, and to allow greater proximity of the camera to the chest wall. Homogeneous myocardial uptake in the rest and stress images is typical of normal perfusion, while a defect in the stress images that normalizes in the rest images (i.e. a reversible defect) indicates an inducible perfusion abnormality which may be caused by a coronary stenosis (*Prvulovich, 2006*). The presence of a defect in both the stress and rest images (a fixed defect) corresponds to an area of infarction in the heart. The location of the defect is symptomatic of the vessels involved, and the physician has to distinguish true defects from artifacts arising from raised diaphragms in men and attenuation artifacts from large breasts in women.

Cardiac gating adds a vital dimension to myocardial imaging, enabling the diagnosticians to distinguish real defects from artifactual ones, in addition to empowering them to visualize cardiac motion and wall thickening (by means of cine-loop displays), and assess cardiac function quantitatively by means of calculations of chamber volumes by clinical software packages. The most commonly used ones are Quantitative Gated SPECT (QGS) developed at Cedars-Sinai Medical Center (*Germano et al., 1997; Germano et al., 1995*), 4D-MSPECT from the University of Michigan Medical Center (*Nakajima et al., 2001; Schaefer WM, 2004*), and Emory University's Emory Cardiac Toolbox (*Faber et al., 1999*). The largest volume of the heart (which occurs when the myocardium relaxes in preparation for refilling) and the smallest volume (which occurs during myocardial contraction in the ejection phase) represent the end-diastolic volume (EDV) and end-systolic volume (ESV) respectively, while left-ventricular ejection

fraction (LVEF) is estimated using the formula (EDV – ESV) / EDV x 100 (*PaulNabi, 2004*). As seen in Figure 2.3, gating is accomplished by means of an ECG signal that is used to trigger acquisition of the images. Acquisition starts with the R wave of the ECG, and images during one cardiac cycle (represented by the R-R interval) are divided into frames of equal duration – usually 8 or 16 (*PaulNabi, 2004*).

An attempt to reach a consensus worldwide on the normal range of LV ejection fraction at rest and during exercise, that pooled data of 1200 subjects from 28 centers in nuclear cardiology, revealed that the lowest and highest normal values of EF were considered to be around 47-50% and 70-77% (*Pfisterer ME, 1985*). During exercise, these numbers were expected to increase more than 5 absolute EF percent over a normal resting value. Physicians in the Nuclear Medicine clinic at UNC Hospital also confirmed that they considered these ranges to be normal.
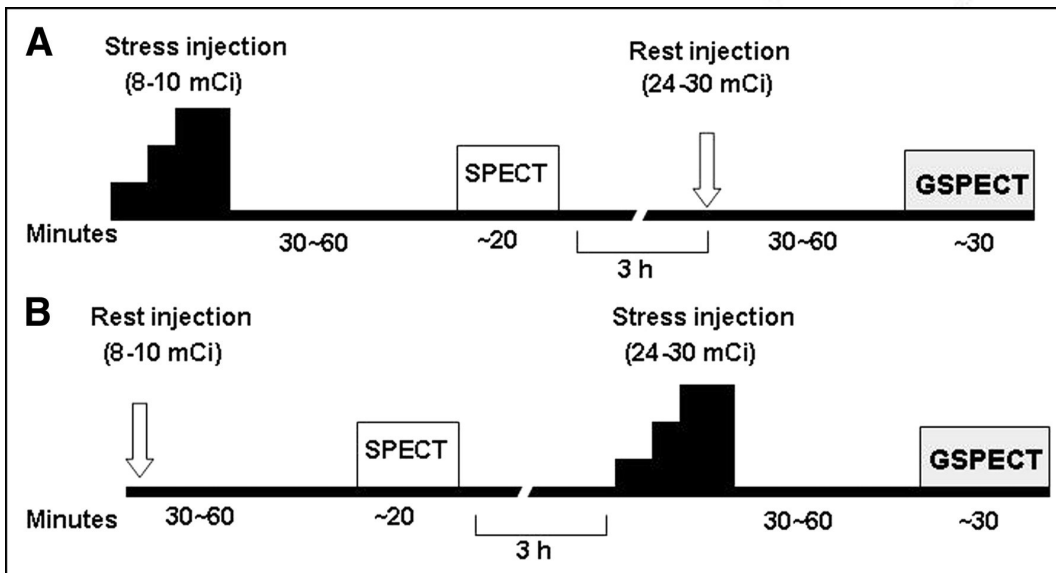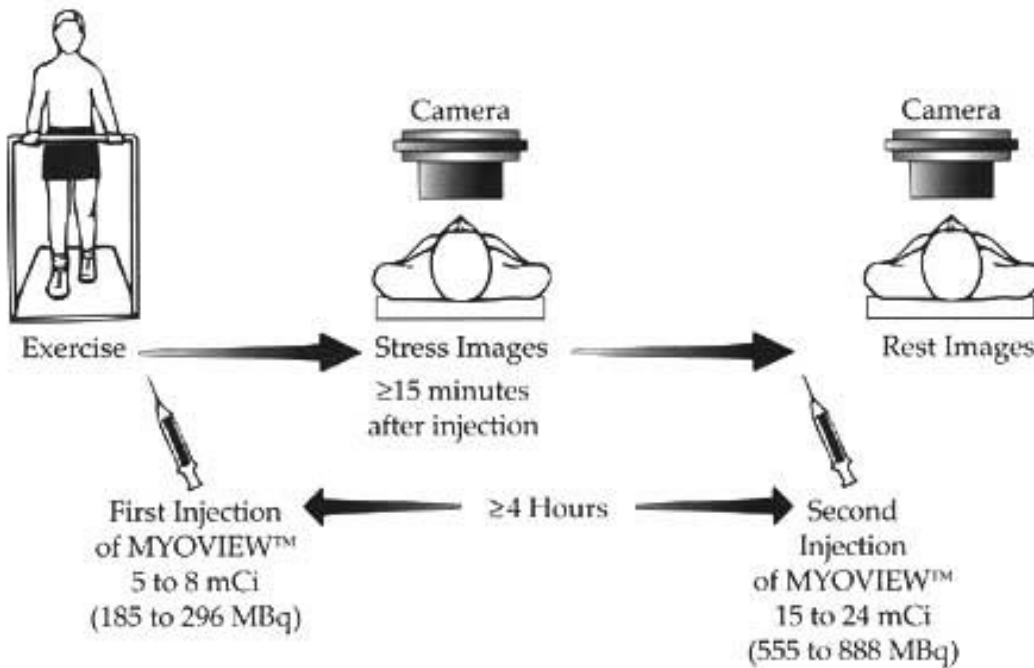
Figure 2.2: Figures from http://us.myoview.com/tech/diagtest.html and (*PaulNabi, 2004*), show typical gated SPECT imaging protocols using Technetium-99m tetrofosmin (Myoview™).
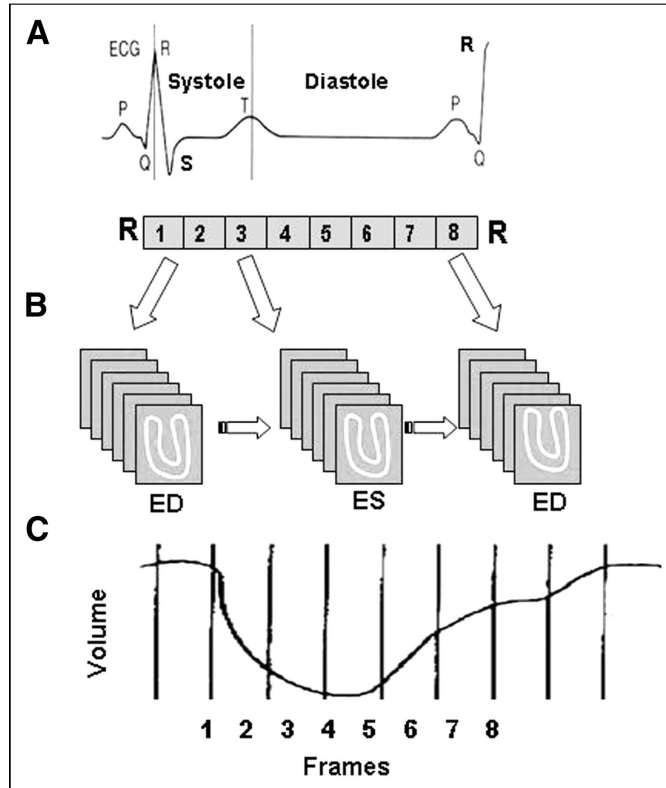
Figure 2.3: This schematic (*PaulNabi, 2004*) shows the principle of ECG-gating, tying the phases of the cardiac cycle to the SPECT image acquisition, and subsequent identification of the end-diastole (ED) and end-systole (ES) positions of the heart.

2.1.3 Imaging of Obese Patients

A principal problem with gated SPECT images is the increase in noise due to the division of total acquired counts for each view into time frames, and this issue is magnified in the case of obese patients, due to excess soft-tissue attenuation of the radioactivity that produces artifactual defects and can result in "flashing" artifacts that can appear as streak defects in reconstructed images (*PaulNabi, 2004*). Obese patients are those with a body mass index (BMI) of greater than 30, in whom the gated SPECT data is found to be too noisy to be useful for diagnostic purposes. Despite the additional information that ECG-gating can provide (toward distinguishing real defects from attenuation-related artifacts), and techniques like prone imaging that may be used (to

12

reduce inferior wall attenuation) (*Berman et al., 2006*), the increase in noise from gating can be substantial enough for clinicians to discount 4D data altogether in this population of patients. Thus, physicians are rendered incapable of adequately assessing the left ventricular function in the population of patients who are at greatest risk for abnormalities in this area.

2.2 Image Processing

One place where the problem of noisy images can be compensated to some extent is the reconstruction process. The projection data acquired during the SPECT imaging is reconstructed to provide a 3D distribution of activity (stack of two-dimensional transaxial slices) than can be viewed and assessed for defects. In the case of gated SPECT studies, reconstruction yields 4D images (which are a collection of 3D images at each time frame), which depict the radioactivity distribution in the moving heart (when images from each of the frames are interleaved in a cine format), and thus allow the physician to view any motion defects that may be present.

The reconstruction methods that will be evaluated in this dissertation are: the iterative OS-EM algorithm (*HudsonLarkin, 1994*) combined with a 3D post-reconstruction Gaussian filter (abbreviated OS3D), the OS-EM algorithm with 4D filtering with a Gaussian filter for smoothing in the spatial domain and then a Butterworth filter for smoothing in the time domain (abbreviated OS4D), and finally, a 4D RBI-MAP algorithm (*LalushTsui, 1992*) which incorporates different Gibbs priors for differential smoothing in the spatial and time domains (abbreviated RBM). It is of great interest to

see how they compare at the task of reconstructing noisy gated SPECT images from obese patients and phantoms.

2.2.1 3D Filtering

There are two basic types of filters used in SPECT imaging: smoothing and enhancement filters. Smoothing filters are low-pass filters that allow the user the option of selecting a filter cutoff frequency where the filter rolls off, while the enhancement and restoration filters attempt to recover resolution by exceeding unity gain over a desired frequency band (*Gilland et al., 1988*). The Hanning and Butterworth filters are smoothing filters, while the Metz filter is an enhancement filter.

The Nuclear Medicine clinic at UNC Hospital uses 3D Gaussian filters on gated SPECT images, so they were chosen for the purposes of this study. The Gaussian filter is a low-pass filter specified by the sigma (σ) of the Gaussian convolution kernel in terms of number of pixels or millimeters (mm), and can be applied in either the spatial or frequency domains to the data. The area of the spatial domain Gaussian is normalized to one to preserve total image intensity. The equation of the isotropic Gaussian point response in 3D is:

$$G(x, y, z) = \frac{1}{2\sigma^2} \exp(-\frac{x^2 + y^2 + z^2}{2\sigma^2}),$$

where x, y, and z represent the distances from the origin in the three axes, while σ is the width parameter of the Gaussian distribution. Gaussian blur is primarily used to decrease image noise by reducing the noise-dominated high-frequency components of an image, and could be useful in smoothing the noise in gated SPECT images.

14

2.2.2 4D Filtering

4D Linear filters are similar to 3D and 2D filters in how they work. The smoothing filter is a low-pass filter that is applied to the 4D image, considering the image as a 3D image (in the spatial dimension), with an additional temporal dimension. The cut-off frequencies are defined separately for the spatial and temporal domains. In this dissertation, a 3D Gaussian filter will be used first for spatial domain filtering in *x*, *y*, and *z*, and then a one-dimensional Butterworth filter will be applied in the time domain.

The Butterworth filter defines its cutoff frequency as the point where the gain is down to 0.707, and it maintains a value close to 1 at low frequencies, with a steep rolloff that is determined by a parameter *n*. It is defined in the frequency domain as follows:

$$B(v) = \left(1 + \left(\frac{v}{v_c} \right)^{2n} \right)^{-\frac{1}{2}},$$

where v is the spatial frequency, and v_c is the cutoff frequency. As with any filter, there is a tradeoff between resolution and noise with different filter cutoffs – lower cutoffs result in smooth images with worse resolution while higher cutoffs lead to better resolution with more noise (*Gilland et al., 1988*).

2.2.3 Ordered-Subsets Expectation-Maximization

In contrast to simple filtering, iterative reconstruction algorithms are attractive for their ability to model image degrading effects such as attenuation, collimator-detector response and scatter, but may take time to converge to a solution if such compensations are applied. Ordered-subset expectation-maximization (OS-EM) is one of the dominant

15

iterative reconstruction algorithms for its ability to suppress noise, its speed, and simplicity of implementation (*LalushTsui, 2000*).

The OS-EM reconstruction algorithm may be written in the following form:

$$x_i^{new} = \frac{x_i^{old}}{\sum_{j \in S_n} c_{ji}} \sum_{j \in S_n} c_{ji} \frac{p_j}{\sum_k c_{jk} x_k^{old}},$$

where p_j denotes the projection data, i.e. the measured events in projection bin j, c_{ji} represents the probability of photons emitted in pixel i being detected in projection bin j, and x_i represents the estimated intensity at pixel i. Previous and new iterated estimates are indicated by the *old* and *new* superscripts. The projection matrix elements, c, may be used to model non-uniform attenuation, detector response, or scatter.

Backprojection is performed for a subset S_n of the projection bins, and with each subset, an update is made to the estimate. All the subsets are thus used to generate the iteration, which is completed when all of the projection data have been used. This process of backprojection and updating repeats, always starting with the first subset, to generate more iterations (*HudsonLarkin, 1994*).

2.2.4 Rescaled Block-Iterative Maximum a Posteriori

The rescaled block iterative maximum *a posteriori* (RBI-MAP) algorithm, a relative of the rescaled block-iterative expectation-maximization (RBI-EM) algorithm, was developed a few years earlier, in response to the need to have an algorithm where noise smoothing is applied to the 4th dimension without a significant reconstruction time cost. The RBI-MAP algorithm can be written as follows:

16

$$x_i^{new} = x_i^{old} + \left[\frac{1}{t_n}\right]\left[\frac{x_i^{old}}{\sum_j c_{ji} + \frac{\partial}{\partial x_i}\log P[\mathbf{x}]}\right]\left[\left\{\sum_{j\in S_n} c_{ji}\left(\frac{p_j}{\sum_k c_{jk} x_k^{old}} - 1\right)\right\} - \frac{\partial}{\partial x_i}\log P[\mathbf{x}]\right]$$

where x_i^{new} and x_i^{old} are the new and previously iterated estimates of the intensity at pixel i, c_{ji} represents the probability of photons emitted from pixel i being detected in bin j, $P[x]$ is the prior density function, and t_n is the step size, which is a scalar that is computed for each subset (*LalushTsui, 1998*). The step size t_n is given by:

$$t_n = \max_i \left[\frac{\sum_{j\in S_n} c_{ji} + \frac{\partial}{\partial x_i}\log P[\mathbf{x}]}{\sum_j c_{ji} + \frac{\partial}{\partial x_i}\log P[\mathbf{x}]}\right]$$

The 4D RBI-MAP algorithm includes smoothing constraints in the form of 4D Gibbs priors (*LalushTsui, 1996*) that accomplish smoothing in the time dimension by extending the smoothing to 'space-time voxels' defined similarly to the relationships between voxels that are close spatially (*LalushTsui, 1998; 1998*), except that these voxels are part of a lattice that has 3 spatial dimensions with 1 temporal dimension. The Gibbs priors are designed to retain edge features while smoothing noise, and this is what makes them very useful in gated SPECT studies, particularly when it comes to smoothing in the time domain. Potential functions useful for time domain smoothing require that two neighboring voxels should have similar intensity levels; if the difference between the voxels is extreme and is supported by neighboring pixels, the difference is likely to represent an edge; these voxels are then decoupled from smoothing (*LalushTsui, 1998*). For the prior, the potential function for spatial-only cliques used in this study employed

the Green function (*Green, 1990; LalushTsui, 1992*), while the potential for time-space cliques was the generalized potential function (*LalushTsui, 1996*).
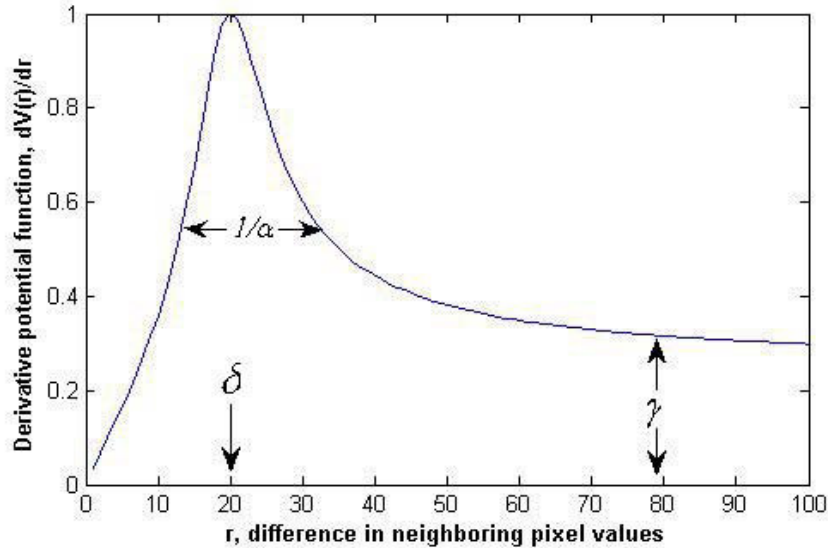
Figure 2.4: The derivative potential function of the generalized prior (shown) determines the relative strength of smoothing pixel differences by the MAP-EM algorithm (*LalushTsui, 1996*).

There are a few important parameters native to the potential functions used for smoothing, and their weighting is determined by the β parameter in the reconstruction procedure; under-weighting leads to noisy images while over-weighting a prior can result in image degradation (*LalushTsui, 1992*). The properties of the smoothing by the potential function are determined by the parameters α, γ and δ, which determine the shape of the derivative potential function, shown in Figure 2.4. Increasing the α parameter decreases the peak width, thus determining the selectivity of the algorithm in smoothing various intensity differences. The parameter δ determines the location of the peak with respect to *r*, the difference in intensity values between neighboring pixels, and is the most important parameter in determining the properties of the smoothing applied. The parameter has to be selected so as to place the peak of the function below image edges

18

that denote organ edges moving over time (*LalushTsui, 1996*). The γ parameter determines the height of the tail and the convergence of the algorithm.

2.3 Tools and Techniques Used in the Study

There are several important tools that will be used for the evaluation of the reconstruction methods in this study, and they are described below.

2.3.1 4D Anthropomorphic Phantom

One of the tools that is invaluable in this study, is the 4D Extended Non-Uniform Rational B-Splines-(NURBS)-based Cardiac Torso (formerly NCAT, now known as XCAT) phantom. The XCAT phantom is a geometry-based computerized phantom which includes realistic models of cardiac and respiratory motion, allows for the modeling of perfusion and motion defects of the myocardium, for the modeling of different organ and body sizes, as well as for the modification of radioactivity uptake ratios and attenuation maps (*Segars, 2001; Veress AI, 2006*). It is thus a very powerful tool that provides the researcher with a gold standard with which to evaluate medical imaging techniques and reconstruction methods.

The beating heart motion in the original 4D NCAT phantom was based on cardiac motion documented in a set of gated tagged MRI data in a normal volunteer, which did not allow for realistic modifications to LV motion. Recently, this problem was overcome by the incorporation of a physiologically-based finite-element mechanical heart model in the 4D NCAT that is capable of accurately simulating LV motion (*Veress AI, 2006*). The updated NCAT phantom with the finite-element model allows for the simulation of a

19

wide variety of motion abnormalities, and motion defects of any size and shape. It will be used to generate a population of obese phantoms for the study that can be used to validate the differences between the EDV, ESV, and EF using the software analysis package on the clinical computer.
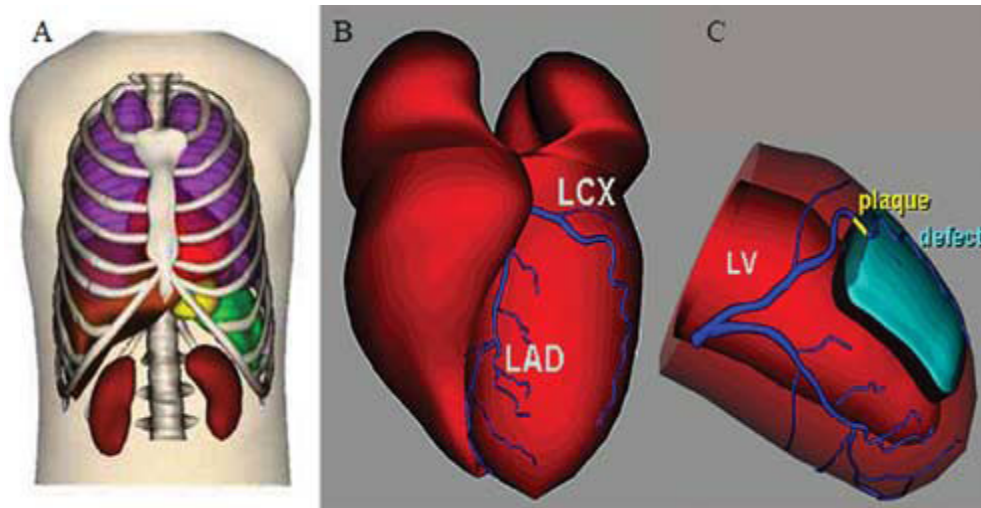
Figure 2.5: Image from (*Veress AI, 2006*) shows A) Anterior view of the 4D NCAT phantom, B) 3D model of the heart in the NCAT with branches of the coronary artery labeled, and C) 3D model of the left ventricle showing the inner and outer surfaces with coronary arteries overlaid, as well as simulated plaques and a defect.

2.3.2 Medical Image Format

The National Electrical Manufacturer's Association (NEMA) created the Digital Imaging and Communications in Medicine (*Committee*) Standard in the late 1980s to aid in a standard method for the transmission of medical images and associated information. The DICOM Standard defined the operation of Service Classes beyond the simple transfer of data, and created a mechanism for uniquely identifying Information Objects as they are acted upon across the network (*Committee, 2008*).

A DICOM file consists of header or metadata (that stores information such as patient name, ID number, type of scan, date and time of scan, image dimensions, imaging modality, pixel size, etc.) as well as all of the image data, typically in grayscale format. Patient data from the clinic is usually in this standardized DICOM format, and must be converted to the .im format used with most of the reconstruction software programs used in the Laboratory for Emerging Imaging Technologies at UNC.

The .im image format and a whole library of commands and subroutines built to handle images in this format, were developed by Zimmerman, Entenman, Fitzpatrick and Whang. Version 2 of the library was furthered by John Gauch in 1987, revised by Graham Gash in 1989, and once again by Luc Florack in 2007 (*Florack, 2007*). Images created and manipulated by the library are stored in standard UNIX files, and can be broken down into 3 sections including an image header, the pixel data of the image, and the image information field which has ASCII strings that describe various properties of the image (*Florack, 2007*).

The image format of the .im image is sufficiently different from that of the DICOM image, and a conversion is necessary of the DICOM patient data to enable one to take advantage of all the reconstruction algorithms and other functions available in the .im image library. Once the processing is completed, a re-conversion is necessary, to enable the import of the reconstructed data back onto the clinical workstations, so as to facilitate data analysis using the clinical software packages.

2.3.3 Quantitative Analysis using Software Tools

There are several commercially available software analysis tools for working with 4D gated SPECT images. Emory Cardiac Toolbox (ECT), 4D-MSPECT, and

Quantitative Gated SPECT (QGS) are the most frequently used software packages, though there are others such as MultiDim (from Stanford University), the W-L CQ (from Yale University), the Left Ventricular Global Thickening Fraction (LVGTF) and the Perfusion and Functional Analysis for Gated SPECT (pFAST), from Sapporo Medical University in Japan (*Sciagra, 2007*).

The algorithms for calculating left ventricular function parameters in the Emory Cardiac Toolbox were developed in the late 1990s. A new modeling method (in contrast to the geometric approximation or 3D surface detection techniques that were in use at the time) was introduced by the researchers that estimates the 3D endocardial and epicardial surfaces of the LV in gated perfusion tomograms for all frames through the cardiac cycle. The EDV and ESV are calculated from these boundaries, as well as the myocardial mass and the EF, and the volumes were validated using correlated MRI studies (*Faber et al., 1999*). Since then, further evaluations of the algorithms using FPRNA, ERNA, ECG, and gated blood pool have been conducted, and the conclusion was that ECT was good in terms of reproducibility and correlated well with the studies. ECT was found to slightly overestimate EF in small hearts and patients without perfusion defects, however (*Nakajima et al., 2001; Sciagra, 2007*).

The semi-automated 4D-MSPECT software developed at the University of Michigan's Medical Center makes estimates of the ventricle from a two-dimensional gradient image, and uses a series of one-dimensional and two-dimensional weighted splines to refine the endocardial and epicardial surfaces (*Ficaro et al., 1999; Schaefer WM, 2004*). An interactive quality assurance module allows the user to adjust the estimated basal plane when the algorithm does not adequately detect the estimated plane.

22

As in the case of ECT, the reliability of the algorithm was tested with comparisons to ERNA and MRI studies (*Nakajima et al., 2001; Schaefer et al., 2005*). A few comparative papers (comparing analysis software) have reported no significant differences in EDV estimation between ECT and 4D-MSPECT (*Nakajima et al., 2001; Schaefer et al., 2005*)

This dissertation focuses solely on the QGS analysis package, however, as it is the one most frequently used in the Nuclear Medicine clinic at UNC. QGS is a stand-alone application distributed by the Cedars-Sinai Medical Center. It estimates boundaries by first determining the maximal-count mid-myocardial surface, subtending rays to it normally, and extracting count profiles for each ray. Asymmetric Gaussian fits on the count profiles then aid in the detection of the endocardial and epicardial boundaries (*Germano et al., 1995; Schaefer WM, 2004*). Initial validation was done with results from FPRNA, and subsequent ones with data from ERNA, ECG and MRI, and good correlation was found (*Nakajima et al., 2001; Schaefer WM, 2004; Schaefer et al., 2005*). QGS is reputed to have a high reproducibility in inter-institutional studies as well (*Nakajima et al., 2001; NakajimaNishimura, 2006*). Comparison studies with other methods revealed however, that estimations of EDV by QGS are often lower than with 4D-MSPECT or ECT (*Schaefer et al., 2005*). Underestimation of chamber volumes was found to be particularly severe in small hearts, up to 75% for a 50 mL volume and 50% for a 37 mL volume chamber in one of the studies that explored this phenomenon (*Nakajima et al., 2000*).

QGS, as a software package, has several user-friendly features, including the automatic generation of left ventricle inner and outer surfaces, the ability to display the

datasets in both static and cine mode, the ability to display up to 4 datasets side-by-side, static or interleaved, the computation of the functional metrics EDV, ESV, EF, and left ventricular volume/time curves. It also allows the user the option of manually fitting contours if the automatic segmentation is unable to accurately identify the endocardial and epicardial surfaces. QGS has display modes that are quite sophisticated, including a Slice mode which displays a vertical long-axis (VLA) and horizontal long-axis (HLA) image, with three short-axis (SA) slices at specifiable locations on the VLA image, a Splash mode that displays a whole series of VLA, HLA and SA slices from each method, a Surface mode that displays a 3D rendered gated image of the left ventricle within a meshwork frame, and a Views mode which displays three different views of the 3D rendered gated image. These are illustrated below in Figures 2.6 and 2.7 using reconstructed images from a patient in the study, where three datasets are shown, one from each of the three processing methods evaluated in this dissertation.
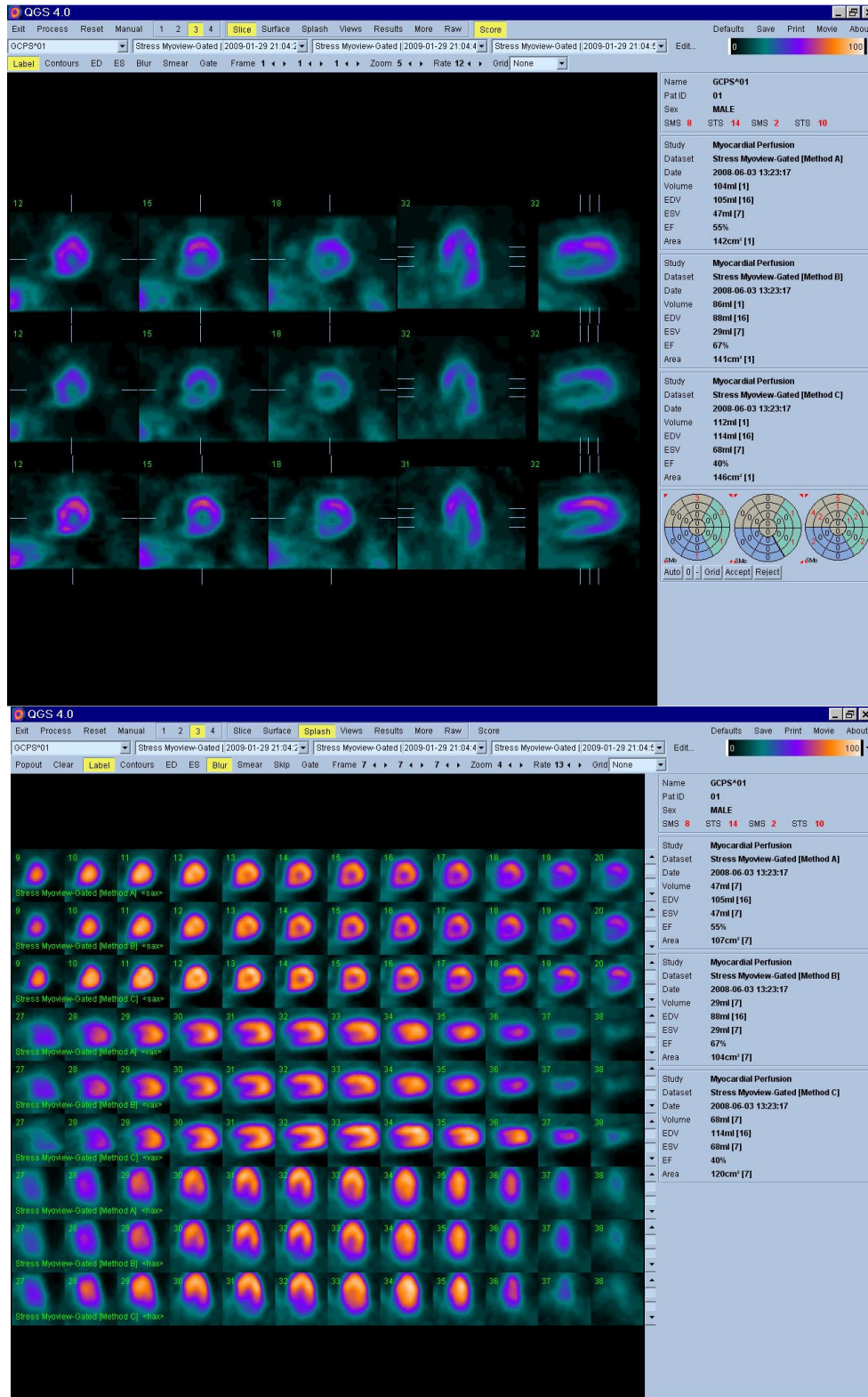
Figure 2.6: The screencaps above illustrate two display and analysis modes in QGS. The image at the top is a 'Slice' display mode showing images from 3 processing methods for a study patient at end-diastole, while the image on the bottom is the 'Splash' view where a series of SA, VLA and HLA slices can be seen from each method.
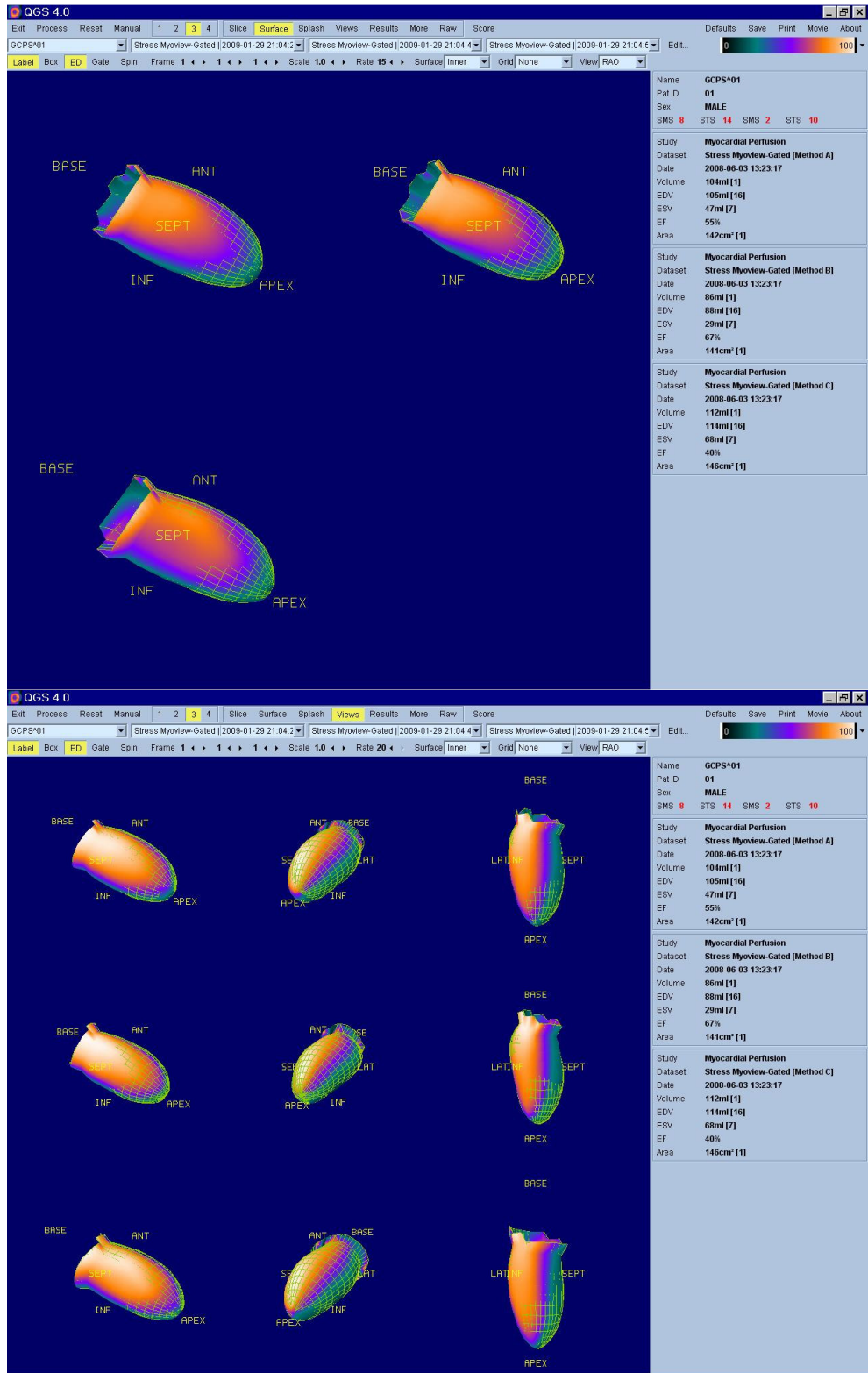
Figure 2.7: The images above illustrate two of the display and analysis modes in the QGS software. The image on the top is the 'Surface' mode that can be gated, as can the 'View' mode on the bottom, which shows different orientations of the 3D rendered heart.

2.3.4 Preference Studies

When it comes to comparing two or more different imaging modalities or reconstruction algorithms, observer studies are routinely conducted with a set of data with known diagnoses, receiver operating characteristic (ROC) curves drawn up comparing the true positive fraction to the false positive fraction, and a judgment made as to the efficacy of the imaging or reconstruction methods under question. Standard observer studies display 2D images, while a motion observer study which displays 4D images (that are a series of 3D images animated over the frames of the cardiac cycle) is better suited to viewing dynamic images. A motion observer study was successfully performed a few years ago, to evaluate the differences in motion defect detection between 8 frame gating and 16 frame gating (*Lalush et al., 2005*).

In gated myocardial SPECT, a key feature is the information that 4D data can provide, which is not gleaned from a myocardial perfusion SPECT study. This data takes the form of chamber volumes provided by the clinical software packages, that the physicians may rely on to make diagnoses, as also cine-loop displays that depict the motion of the heart, which are useful in enabling them to distinguish attenuation artifacts from real motion defects that need to be treated.

The bottom line of this study is to determine if the 4D reconstruction methods RBI-MAP and 4D filtering are able to improve the noise properties of the image adequately without resulting in a loss of temporal information, so the physician feels that it has solidly impacted the ability to make an accurate diagnosis, as compared to using images reconstructed with the 3D OS-EM algorithm with 3D smoothing filters. The

preference of the physician is crucial and the best way to evaluate this intangible element is to do a preference study.

These studies have professionals for observers (in this case, nuclear medicine physicians), employ a side-by-side review of pairs of images and subject the observer to using a discrete rating scale to record the preference. Preference studies have been employed in radiology, in several studies on digital mammography to determine radiologists' preferences for display and analysis methods (*Good et al., 1999; Pisano ED, 2000*), but have not been used in nuclear medicine thus far.

In a preference study, the observer is presented with the case history at the outset, asked to review the pairs of images side-by-side (if the design calls for it, or separately), and is then asked to rate which image of each pair s/he thinks was more useful in leading to the diagnosis. The variance in the different methods among physicians can then be analyzed using an ANOVA technique described below.

2.3.5 ANOVA

The data from the preference study is analyzed by means of analysis of variance (ANOVA) techniques to determine whether the null hypothesis (that there is no difference among the techniques being compared) is to be accepted or rejected. A one-way, repeated-measures ANOVA will be used, as there is only one primary source of variance (i.e. the reconstruction method), and all the members of the population are reconstructed using the same methods (repeated measurements on one sample).

ANOVA is a widely used technique for separating the observed variance in a group of samples into portions that are traceable to different sources. If all the samples are lumped together into one large sample, the observed variance will be partly due to the

differences between the individual members of the same original sample, and partly due to the effects of the different treatments. The ANOVA method enables us to estimate how much of the variance is attributable to the one cause, and how much to the other, so as to enable a decision on whether the treatments have produced any significant effects (*Keeping, 1995*).

The purpose of an ANOVA is to test for significant differences between population means by analyzing the variances. The test assumes that the residuals are normally distributed, and that they have equal variances. In a one-way analysis of variance, the total variance of a set of scores is partitioned into two components: a between-groups component and a within-groups component. The ratio of these two components (between-groups over within-groups) is the test statistic F. If the null hypothesis (that there is no difference among the groups) is true, then F will have an expected value of about 1 and a random sampling distribution that is described by one member of the family of F-distributions. If the null hypothesis is false, the expected value of F will be greater than 1, and the random sampling distribution of F is shifted to the right. Using the appropriate F-distribution, we can calculate a p-value for the F-test, i.e. the probability of obtaining an F-value that is large or larger, given that the null hypothesis is true. If the p-value is sufficiently low (.05 or less), we may reject the null hypothesis (*Keeping, 1995; Montgomery, 1997*).

Chapter 3

Methods

3.1 Development of an Obese Phantom Population for Gated Myocardial SPECT Imaging with Tc-99m Tetrofosmin

Studies that compare reconstruction algorithms for use on clinical data are best done using patient data so that the impact of the study can be best judged within the context of its utility to clinical studies. However, it is very time-consuming to accumulate adequate clinical data acquired under a desired set of conditions or parameters. It is much more practical to have a mathematical tool as a gold standard that is useful for quick comparisons and large-scale studies not as easily possible with patient data. Toward this end, it is proposed to build a standard obese male and female phantom that can be modified as desired for use in this study. As the results of this study would be most useful when it is easily applicable to clinical data, it is desired to closely match the physical and physiological characteristics of the clinical population in the phantoms. Before the phantom population can be generated, some parameter optimization is required.

3.1.1 Reconstruction Parameter Optimization Study

In a study where there are multiple reconstruction methods being compared, it is vital to choose the parameters native to each algorithm carefully in the interests of standardization, so there is some solid basis for comparison rather than a random

selection of parameters. In this study, it was decided that the reconstruction parameters for each processing method (or combination of methods) would be chosen such that the noise standard deviation is the same for the final image from each method, as calculated from the same transaxial slice of blood pool images.

An obese male phantom was created (having a BMI of 40 with a body weight of 122.6 kg spread over a 175 cm frame) with simulated Tc-99m tetrofosmin activity concentrated in the heart muscle and chambers (blood pool) and all other organs set to background activity. Projection data including the effects of attenuation, detector response, and scatter, were generated from this phantom in a matrix of 64x64 with 64 views over 180° and a pixel size of 6.5913 mm, gated to 16 frames. The volume of blood pool activity in a 10 cm section of the trunk including the heart was found to be 2.5 times the volume of total heart activity (in a typical tetrofosmin study where the uptake concentrates in the cardiac muscle), and so the counts in the noisefree data were scaled down accordingly, and Poisson noise was simulated.

The projection data were reconstructed with each of the reconstruction methods as follows. Comparable to clinical processing, the first method used was the iterative OS-EM algorithm with 8 subsets, up to 6 iterations, followed by a 3D Gaussian filter with FWHMs of 2, 4, 6, 8, 10, 12, 14, 16, 18, 20 mm, applied to the 3rd, 4th and 5th iterations. The 1st and 2nd iterations were found to be too smooth while the 5th and 6th were found a bit too noisy, which is why the rest of the study focused on applying filters to the 3rd and 4th iterations. The second reconstruction method was the OS-EM algorithm with 8 subsets, where the 3rd and 4th iterations were followed by a 3D Gaussian filter with FWHM of 16 mm, and order 8 Butterworth filter applied in the time domain, with filter

cutoffs of 0.2, 0.3, 0.325, 0.35, 0.4 cycles/pixel. The third method explored the parameters native to the RBI-MAP algorithm (with 8 subsets and 6 iterations), including values of 1, 2, 3, 5, 10 for the spatial prior's δ parameter with fixed time δ, spatial and time β parameters; values of 5, 10, 15 and 20 for the time δ (with all the other parameters fixed), values of 0.0015, 0.0020, 0.0025 for the spatial β (with everything else fixed), and values of 0.0007, 0.0015, 0.0022 for the time β parameter. The spatial α and γ parameters were not varied as they were fixed at 1.0 and 0.50, respectively, while the time α and γ parameters were kept at 2.0 and 0.10, respectively.

After each of these processing methods were applied, the images were inspected visually for image-degrading artifacts that might rule out any set or sets of values, and for general image quality as compared to the other processing methods. The noise standard deviation was also calculated on the same selected transaxial slice from each set of reconstructed data. This study allowed a selection of parameters for each reconstruction method that resulted in very similar noise statistics in the reconstructed blood pool images.

3.1.2 Patient Database

A database of clinical gated SPECT data was created with patient projection data obtained from 28 obese patients in the Nuclear Medicine clinic at UNC Hospital. Patient names and other protected health information were removed by authorized clinic personnel before the data transfer, and all procedures were approved by the institutional review board. The patients had been administered technetium Tc-99m tetrofosmin, and

the images had been acquired in matrix sizes of 64x64 (with a pixel size of 6.5913 mm), with 64 views and gating into 16 frames.

The projection data were reconstructed with the OS-EM and RBI-MAP reconstruction algorithms, each of them with 8 subsets, up to 5 iterations. The data reconstructed with the OS-EM algorithm were further processed with 3D and 4D filters. A 3D Gaussian filter with FWHM of 18 mm was used (similar to the Gaussian with FWHM of 17 mm used in the clinic) as one post-processing method, while the 4D filtering was accomplished with a 3D Gaussian filter with FWHM of 16 mm followed by an order 8 Butterworth filter applied in the time dimension with a filter cutoff of 0.325 cycles/pixels. These cutoffs were determined from a separate study described in the previous section.

The projection data and reconstructed data were analyzed to derive relative distributions of quantitative uptake ratios for various organs. Noise levels and noise standard deviations were calculated for 9.89 cm (or 15 slices, each with 6.5913 x 6.5913 x 6.5913 mm^3 voxels) sections of the torso including the heart from each frame of 16 frames of projection data for each of the 28 patients in the study. The average counts per slice in those 15 frames (around 61,440 pixels) came to around 123,000 counts, while the average counts in the noisier datasets was around 85,000 counts.

3.1.3 Phantom Simulation

Anthropometric data was used to obtain a distribution of body dimensions across populations that included people of both genders from different races and ethnic backgrounds (*Pheasant, 1996*). This information was used to determine appropriate body

sizes to use in building obese male and female NCAT phantoms. The phantoms were modeled at heights considered average for the Americans in the anthropometric study, which worked out to 175 cm (or 5 feet, 9 inches) for the male, and 163 cm (or 5 feet, 4 inches) for the female (*Pheasant, 1996*). Since it is desired to study the effects of the extent of obesity on the comparison of the performance of the reconstruction methods, it was decided to model two different body sizes for each gender of obese phantom. A BMI of 40 was selected for the morbidly obese variant, and a BMI of 34 for the moderately obese variant. This translated to weights of 122.6 kg (or 270.3 lbs) and 106.4 kg (or 234.6 lbs) for the morbidly obese male and female phantoms, and 104 kg (or 229.3 lbs) and 90.4 kg (or 199.3 lbs) for the moderately obese male and female phantoms, as seen in Table 1 below. An average noise level of 120,000 counts per slice in the heart region (as determined from the patient database) was chosen for the simulation, with three noise realizations of Poisson noise simulated for each phantom.

Table 3.1: Body sizes of the obese male and female phantoms

Phantom	BMI	Height (cm)	Weight (kg)
Morbidly Obese Male	40	175	122.6
Morbidly Obese Female	40	163	106.4
Moderately Obese Male	34	175	104
Moderately Obese Female	34	163	90.4

Once body sizes were selected, the heart sizes were scaled to fit the body sizes for each of the phantoms, and the breasts in the female phantoms were also simulated to be realistic in size and orientation to mimic patients lying supine on pallets.

A couple of different motion defects were also generated in addition to a physiologically normal case for each phantom (with an EF of 60%). There were two hypokinetic variations simulated in the form of a motion defect in the chamber walls of the phantoms. The more severe variant was designed to yield an EF of around 28%,

while the milder variant was designed to be borderline with an EF of around 44%. The table below shows the parameters of the defect simulation.

Table 3.2: Physical characteristics of the motion defect phantom models

Parameter	Less Hypokinetic	Very Hypokinetic
Chamber Walls Affected by Motion Defect	Lateral	Anterior, Lateral, Inferior
Radial Extent of Each Defect (deg)	60	120
Width along long-axis (mm)	40	80
Fraction of outer wall transgressed	1.0	1.0
Lesion motion (% of normal)	0	0

Using the knowledge gleaned from the analysis on patient projection and reconstructed data, and published literature on tetrofosmin uptake kinetics(*Higley et al., 1993*), several uptake distributions were modeled in the organs of the obese 4D NCAT phantoms. Tetrofosmin uptake ratios were then modeled in the obese phantoms, and projection data including the effects of non-uniform attenuation, detector response and scatter, were generated from the obese male and female phantoms, in matrix sizes of 64x64, with 64 views over 180° (from the Right Anterior Oblique (RAO) to the Left Posterior Oblique (LPO)), in 16 bins representing the phases of the cardiac cycle, with pixel sizes of 6.5913 mm, in the interests of mimicking clinical study settings. The noisefree projection data generated were scaled to 120,000 counts (in the stack of 15 transaxial slices including the heart), and Poisson noise was simulated to create noisy data. Six different random seeds were used to generate three noise realizations of noisy data for every phantom in the study. The noisy data were reconstructed with OS-EM with 3D and 4D filters, with no correction for attenuation, detector response or scatter as in the clinic, and 4D RBI-MAP; the parameters for the reconstruction matched the optimal results as determined in the study in 3.1.1.

The projection data and reconstructed data from the patients were compared to those from the phantoms, and the images reconstructed with 3D OS-EM were compared

to those reconstructed with 4D RBI-MAP, to evaluate subjectively the image quality in terms of image contrast and noise.

From each of the reconstructed sets of images of the patient and the phantom, the central slice of the heart image was extracted, and the same views from each of the 16 time frames were compiled into a movie in audio video interleave (AVI) format. These were then subjectively compared to judge the fidelity of cardiac motion preserved by the different reconstruction methods.

3.2 Evaluation of Quantitative Accuracy and Motion Fidelity

The next step to the evaluation of the reconstruction methods for gated studies is to judge the accuracy of the parameters calculated by clinical software packages. One basis of comparison is the qualitative, using clinical patient data reconstructed with the different types of methods and analyzing them visually for differences in resolution, contrast, noise, and smoothness of motion. This does not provide any information as to the quantitative accuracy of the methods however. To be able to compare the quantitative accuracy, a gold standard must be used in the form of a computerized phantom with known/calculable heart chamber volumes. A clinical software package that has robust algorithms to calculate the chamber volumes is also required. The one that was selected for this purpose has been already described in a previous section; it is the QGS application distributed by Cedars-Sinai.

3.2.1 Conversion of Images to DICOM Format

This next step is intended to derive a method to convert the reconstructed images into a format that may be uploaded onto clinical workstations and loaded into the clinical

software package, QGS. Images of patient data that have been acquired from the clinic are typically in DICOM format, NEMA's standard format. These images are converted to the real .im format using MATLAB programs, and image processing is done on the LINUX systems using image reconstruction algorithms coded in the C language.

It is necessary to convert reconstructed images of phantom and patient data from the .im format back to the grayscale 16-bit DICOM format with all the associated metadata changed to reflect the type of reconstructed image it is. A few DICOM converters were tested and found wanting, so a program written for MATLAB (by DS Lalush) was used to accomplish the conversion.

The following method was used for the conversion. Each of the patient datasets had been imported with a reconstructed FBP image in DICOM format. That file was used as a template where the new data was written into. It was found that these DICOM files included only the pertinent 30-35 transaxial slices with the heart. So the first step was to extract out the corresponding 30-35 transaxial slices from the reconstructed images for each time slot for the patient. With patient images, it was necessary to reorder the reconstructed images so they were oriented from feet to head within the file, while the phantom images had the correct orientation to begin with. The images were then restacked so that all the time frames for each transaxial slice were stacked together, before the next transaxial slice, and so on (i.e. the ordering was x, y, z, t). The image had to be further reshaped as MATLAB reads the pixels in a different order than programs written in C. A MATLAB program was then used to read in the array of pixels from the reconstructed .im image, convert them to a 16-bit array, open the FBP DICOM-format

37

image, and replace each of the image pixels of the old FBP image with the new reconstructed image pixels, and output back to a DICOM file.

This .DCM file was imported into the Siemens patient database, and renamed so as to change the header information to reflect the processing mode. A Siemens program to reorient the images into short-axis slices was then used to save the image files in a format recognizable by QGS. Images with hot spots that could degrade the image were put through an additional step of masking that blacked out all areas surrounding a Region of Interest (ROI) drawn around the heart. It was then possible to load all three sets of reconstructed data (i.e. from the different reconstruction methods) into QGS at the same time, so they could be viewed simultaneously in a so-called triple mode, whether as stills or in cine format. QGS could be used to analyze the data in one of several different modes, labeled Slice, Splash, Surface, Views, each of which also displays the calculated EDV, ESV, and EF. In several cases, it was found that the contours approximated around the epicardial surfaces of the left ventricle were not a proper fit, especially when it came to identifying the base of the LV. This was easily rectified with a tab page that allowed for manual curve fitting to be done; reprocessing the data with the new contours also yielded new EDV, ESV and EF values.

3.2.2 QGS Evaluation of Patient Data

Each of the 28 patients in the database had images reconstructed with each of the three processing methods, OS-EM with the 3D Gaussian filter, OS-EM followed by a 3D Gaussian and a 4D Butterworth filter, and the 4D RBI-MAP algorithm. Each set of reconstructed images was converted to the DICOM format, thus yielding 3 separate DICOM files for every patient, that were then imported onto the clinical system. Some

38

of them had hot spots that required the images to be masked, but most could just be reoriented and imported into QGS. Manual fitting was done in every case, to ensure uniformity of epicardial contour fitting especially in the case of smaller hearts or larger hearts than is the norm. It made a big difference in cases where the images were very noisy, where the pre-fit and post-fit quantitative values were vastly different.

The quantitative values calculated by the program, such as ejection fraction (EF), end diastolic volume (EDV), and end systolic volume (ESV) were recorded for each patient, for each reconstruction method. The data were compared using the paired t-test (which assumes that the differences between pairs are normally distributed), with the null hypothesis that the mean difference between the different pairs is zero (McDonald 2008). The methods were compared as follows: the OS-EM with 3D filtering, OS-EM with 4D filtering, and the 4D RBI-MAP algorithm, for each of the EDV, ESV, and EF parameters (even though EF is dependent on the EDV and ESV parameters, it is an important indicator of cardiac health used by physicians and thus worthy of being considered separately here). The paired t-tests yielded p-values that were used to accept or reject the null hypothesis.

QGS was also used to compare the three methods qualitatively across the entire database, and observations were recorded on the static and interleaved images.

3.2.3 QGS Evaluation of Phantom Data

The reconstructed phantom data from the moderately and morbidly obese male and female phantoms were also converted to DICOM as in the case of the patient data. They were imported onto the clinical workstation, hot spots masked, reorientation of the heart accomplished, and analyzed with QGS finally. The EDV, ESV and EF were

recorded from the QGS analysis. As the phantom provides a gold standard, it was possible to compare the actual left ventricular volumes and ejection fraction of the heart with what was calculated in QGS. The EDV and ESV were apparent in the log file generated during phantom creation, and the EF was calculated using the formula described earlier. Once the data were collected, each of the three parameters were compared across phantoms to the truth, and the percent error was computed in each case.

The cine mode in the QGS package enables one to view the three sets of reconstructed image side-by-side for comparison of wall motion. As with the patients, the phantom data were compared qualitatively in QGS, and observations were made on the motion. The EDV, ESV and EF values were compared across phantom populations for the three reconstruction methods, and correlation coefficients were calculated to determine if there was a relationship among the parameters in each population. Paired t-tests were done within populations to determine if there were differences between the methods, as in the patient study.

3.3 Study of Physician Preference for Reconstruction Method

Studies of this nature are most relevant when the diagnosticians' preferences are taken into account, as it is they who have to evaluate clinical gated SPECT images to make diagnoses. Toward this end, an observer preference study was performed with four physicians including three Nuclear Medicine physicians and one cardiologist.

3.3.1 Preference Study

The patient database with reconstructed data from 28 patients (processed with the OS-EM with 3D filtering, OS-EM with 4D filtering, and 4D RBI-MAP algorithm), was

used for this study. There were 18 female patients and 10 male patients, and 20 patients were diagnosed as normal while 8 cases were read as abnormal. The images were converted to DICOM format, imported onto the clinical workstations, and reoriented as described before. The resultant files were labeled Method A, Method B and Method C for the three methods (so the physicians were blinded as to which method was which), and the three files were simultaneously displayed in QGS with those labels.

Instructions were provided to each physician prior to the study. The radiology report for each of the patients was made available before beginning the reading for that patient, which included a brief history of the patient's condition and the results of any other diagnostic procedures performed prior to the gated SPECT study. The three datasets were then loaded in QGS simultaneously with the gating option turned on, so the physicians viewed interleaved images in the "Slice" display mode of QGS. The question posed was to consider which of the three reconstructed datasets most improved his confidence in the diagnosis, and each dataset was graded on a seven-point scale as being much worse, somewhat worse, slightly worse, the same, slightly better, somewhat better, and much better (-3, -2, -1, 0, +1, +2, +3 respectively) than each of the other datasets. The physicians were encouraged to use QGS as they normally would, and in a manner that most enabled them to make a decision, which included switching to other QGS display modes, the option to change color maps if they so chose (the cool metal color map was used as default), and the grayscale display settings. The sessions were kept to an hour on average, to limit the effects of fatigue, and it took 2 sessions on average per reader, to get through the entire database of images. In all, the physicians viewed 84 images (28 patients x 3 processing methods), though one patient dataset was missed due

to an initial glitch in the images that prevented proper viewing by the first two physicians to complete the study.

3.3.2 ANOVA

The data from the preference study were analyzed using a one-way ANOVA, which was performed using a MATLAB program. The null hypothesis of the study is that there is no difference in means among the three reconstruction methods tested (judged by physician preference), and a significance level of 0.05 was used. The standard ANOVA table was generated by the MATLAB program, as well as a plot of the spread of the ratings by method.

Chapter 4

Results

4.1 Development of an Obese Phantom Population for Gated Cardiac SPECT Imaging using Tc-99m Tetrofosmin

4.1.1 Reconstruction Parameter Optimization Study

The obese male blood pool phantom used in the parameter optimization study is depicted below, with a selected transaxial slice of activity and attenuation maps shown in Figure 4.1. The heart is seen prominently, and it was this slice that was compared through the reconstructed images, to judge image quality.

Figure 4.1: Selected transaxial slice of the activity and attenuation map of a blood pool image of the obese male phantom in a matrix size of 64x64, with pixel size of 0.659 cm

Projection data (the same view from 4 time frames), and OS-EM-reconstructed images of the blood pool are shown in Figures 4.2 and 4.3. The projection data were generated in 16 time frames, matrices of 64x64 with 64 views over 180° and pixel size of 6.59 mm. After the addition of Poisson noise, the noisy projection data from each of the time frames were individually reconstructed with OS-EM.
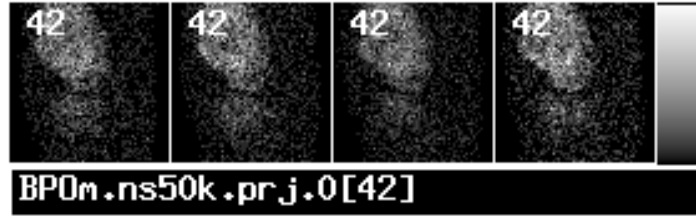
Figure 4.2: Selected angular views showing blood pool projection data from time frames 0, 4, 8, and 12, in the morbidly obese male phantom in a matrix size of 64x64, with 64 views, pixel size of 0.659 cm, and 16 time slots over the cardiac cycle
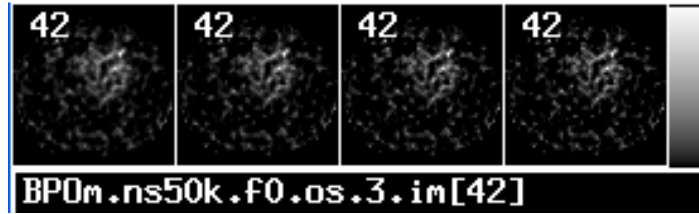
Figure 4.3: Selected transaxial slices of OS-EM-reconstructed images of the blood pool phantom in a matrix size of 64x64, with pixel size of 0.659 cm. Iterations 2, 3, 4, and 5 are shown, and no post-processing filter was applied to these images.

The 3D processing method is shown next in Figure 4.4, where the projection data from the blood pool phantom was reconstructed with OS-EM, and the 4th iteration was further processed with a 3D Gaussian filter with FWHM of 2, 4, 6, 8, 10, 12, 14, 16, 18, and 20mm. It is apparent that increasing the spread of the Gaussian function leads to greater smoothing.
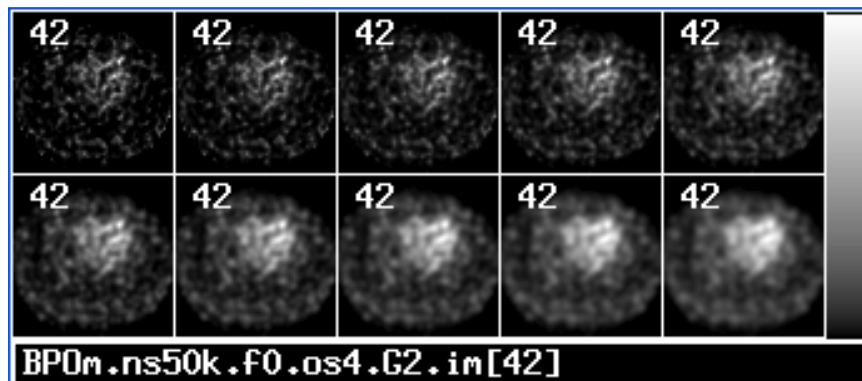
Figure 4.4: Selected transaxial slices of OS-EM-reconstructed images of the blood pool phantom, that were processed with the 3D Gaussian filter with FWHM of 2, 4, 6, 8 and 10 mm (shown in the top row), and 12, 14, 16, 18, 20 mm (shown in the bottom row)

The 4D processing method, where the iteration 4 of the OS-EM-reconstructed image was followed by a 3D Gaussian filter with 16 mm FWHM, then various filter cutoffs for an order 8 1D Butterworth filter, is depicted in Figure 4.5. The image is smoother at lower cutoffs with less noise, with better resolution and higher noise at higher filter cutoffs.
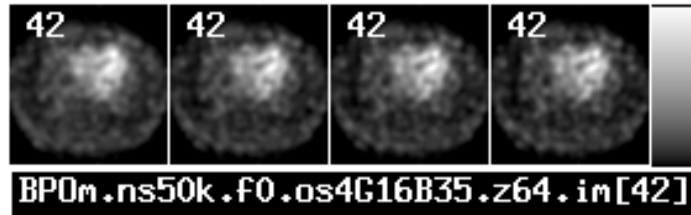
Figure 4.5: Selected transaxial slices of OS-EM-reconstructed images of the blood pool phantom, that were processed with the 3D Gaussian filter with 16 mm FWHM, followed by an order 8 1D Butterworth filter with cutoffs of 0.20, 0.30, 0.35, and 0.40 cycles/pixel, respectively
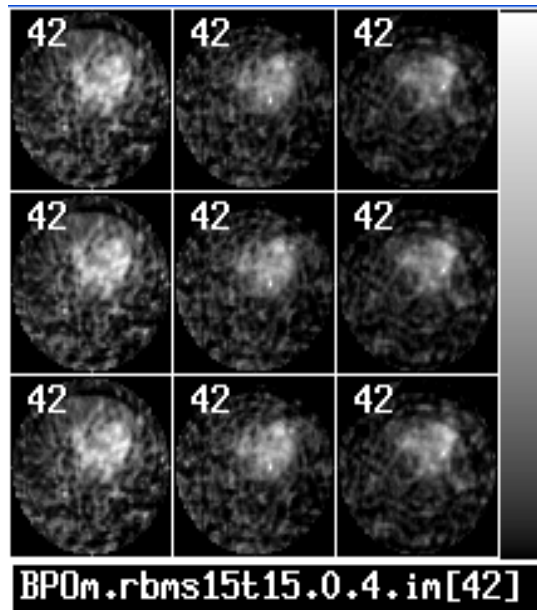
Figure 4.6: Selected transaxial slices of RBI-MAP-reconstructed images from the 4th iteration of the 0th, 2nd and 10th time slots. The three rows show transaxial slices from the 3 time slots reconstructed with the spatial δ parameter set to 3, the time δ parameter set to 12, the time β parameter fixed at 0.0015, while the spatial β parameter in the top row is 0.0015, in the middle row; 0.0020, and in the bottom row, 0.0025.

The parameters of the 4D processing method using the RBI-MAP algorithm were the next to be tested. As described in section 3.1.1, the spatial and time δ parameters and spatial and time β weighting parameters were tested in turn, and in each test case, 3 parameters were kept constant while one was varied, to judge the effects of the parameter on both noise statistics and standard deviation. Figure 4.6 shows the effect of varying the spatial β weighting parameter; there does not seem to be a marked effect on image quality, though certain point artifacts (points of greater intensity than surrounding tissue) are more apparent at lower values of the spatial β than the higher one (i.e. where there is less smoothing). Figure 4.7 addresses the effects of varying the time β weighting parameter while keeping the others constant. In the images shown, the sharp point artifacts seem even more pronounced than in the latter case, and there is a greater variance in image quality. The higher time β weighting parameter is able to suppress the point artifact due to greater smoothing in that dimension. Figure 4.8 depicts the effect of varying the spatial δ parameter with the others constant, and in this trio of images from different time slots, one can see that the lower spatial δ values lead to smoother images while leaving point artifacts of high frequency, while the higher spatial δ value results in noisier images all around. The middle value appears to be the best compromise there.
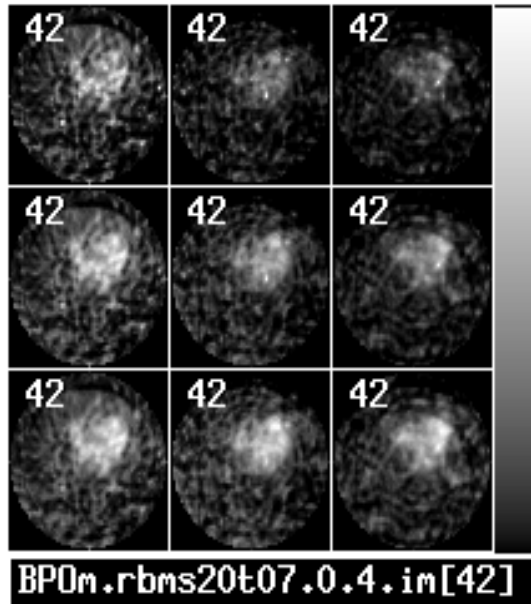
Figure 4.7: Selected transaxial slices of RBI-MAP-reconstructed images from the 4th iteration of the 0th, 2nd and 10th time slots. The three rows show transaxial slices from the 3 time slots reconstructed with the spatial δ set to 3, the time δ set to 12, the spatial β fixed at 0.0020, while the time β in the top row is 0.0007, in the middle row; 0.0015, and in the bottom row, 0.0022.
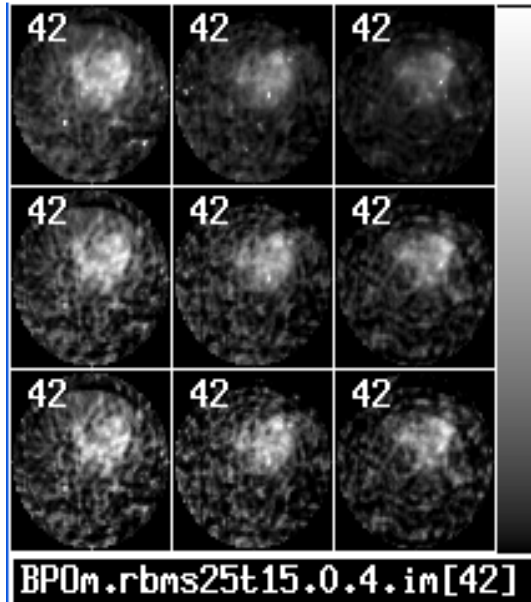
Figure 4.8: Selected transaxial slices of RBI-MAP-reconstructed images from the 4th iteration of the 0th, 2nd and 10th time slots. The three rows show transaxial slices from the 3 time slots reconstructed with the spatial β fixed at 0.0025, the time β set to 0.0015, the time δ set to 10, and the spatial δ varying from 1 in the top row, to 3 in the middle row, and 5 in the bottom row.

Varying the time δ parameter (seen in Figure 4.9) seems to have an effect on image quality that is not largely noticeable, except when one considers the point artifacts again. They are once again apparent in all of the values tested, but one must bear in mind that this could be a factor of the other δ and β values used. So, other combinations of values for β weighting and the δ parameter were tested similarly, and the noise statistics comparison also factored heavily into the choice of parameters for RBI-MAP.

Ultimately, it was found that 4th iteration images from the 3D method using the OS-EM algorithm (with 8 subsets) combined with a Gaussian filter with 18 mm FWHM, compared well with images from the first 4D processing method that used the OS-EM algorithm (with 8 subsets) followed by a 3D Gaussian filter with 16 mm FWHM, and then a 4D order 8 Butterworth filter with cutoff of 0.325 cycles/pixel. Both of these methods had similar noise statistics to the RBI-MAP processing method with spatial β value set to 0.0020, time β set to 0.0022, spatial δ set to 3 and time δ set to 12. Visually, images from the 3 methods compared well also, as seen in Figure 4.10.
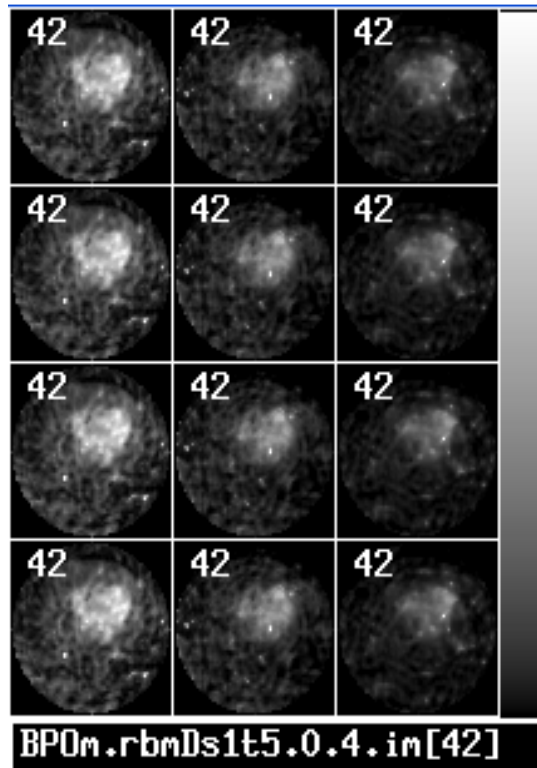
Figure 4.9: Selected transaxial slices of RBI-MAP-reconstructed images from the 4th iteration of the 0th, 2nd and 10th time slots. The three rows show transaxial slices from the 3 time slots reconstructed with the spatial β fixed at 0.0025, the time β set to 0.0015, the spatial δ set to 1, and the time δ varying from 5 in the top row, to 10 in the top middle row, 15 in the bottom middle row, and 20 in the bottom row.
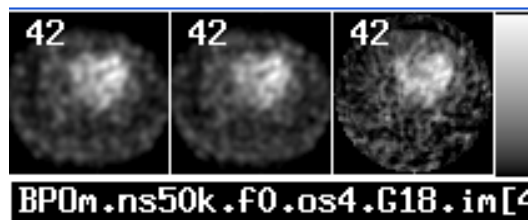
Figure 4.10: Selected transaxial slices of reconstructed images showing the visual appearance of images reconstructed using the optimal parameters found. The first image was generated by filtering a 4th iteration OS-EM-reconstructed image with a 3D Gaussian filter with 18 mm FWHM, while the second was generated by filtering a 4th iteration OS-EM-image with a 3D Gaussian filter with 16 mm FWHM and then a 4D order 8 Butterworth filter with cutoff at 0.325 cycles/pixel. The third image is from an RBI-MAP reconstruction with spatial and time β parameters set to 0.0020 and 0.0022, while the spatial and time δ were set at 3 and 12, respectively.

49

4.1.2 Patient Database

Projection data were collected from 28 obese patients imaged at UNC Hospital for the study (in matrices of 64x64 with 64 views over 180° and 16 time frames), though several tens of others were collected outside of the official study datasets, with some being gated to only 8 frames. The projection data were in DICOM format, and needed to be converted to the .im format first; this was accomplished with a MATLAB program. The .im format projection data were then reconstructed, one time frame at a time, using each of the three methods being studied, at the parameters that were chosen as optimal for each of the methods.

Figures 4.11, 4.15, and 4.19 depict sample projection datasets from three patients, where selected views are seen from a selected frame of the cardiac cycle. Key features are the heightened tetrofosmin uptake in the intestines with less activity in the other organs in the chest and abdomen, reflecting the biokinetic properties of the tetrofosmin. The heart shows up prominently in the dataset with the lowest noise level, but is not so visible in the noisier datasets. Figure 4.11 depicts the lower noise level case, while Figure 4.15 illustrates the average noise level case, and Figure 4.19 is from the patient with the highest noise level among all the study patients in the database.
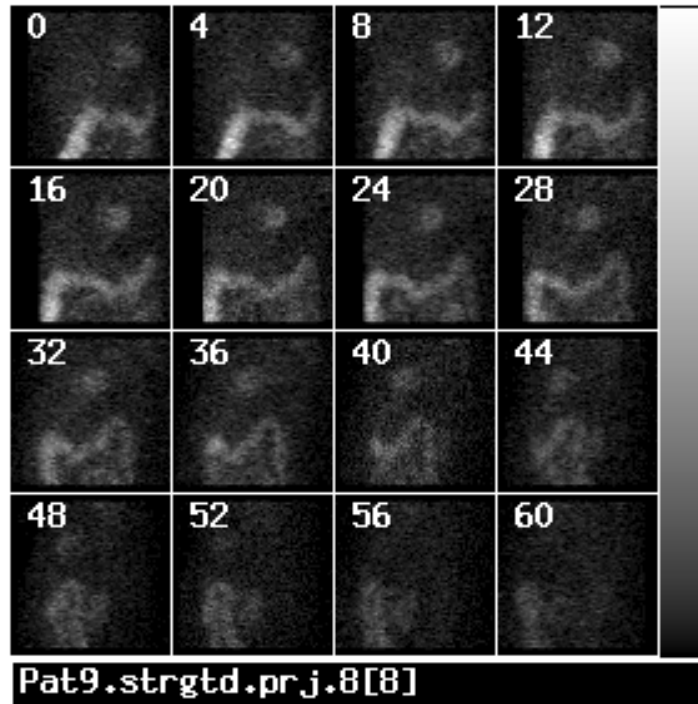
Figure 4.11: Selected views of projection data from the stress image of an obese patient (identified as GCPS 09) who was administered Tc-99m-Tetrofosmin; this dataset shows the eight frame of the cardiac cycle, out of 16 time frames. This dataset illustrates what the projection data looks like at lower noise levels.
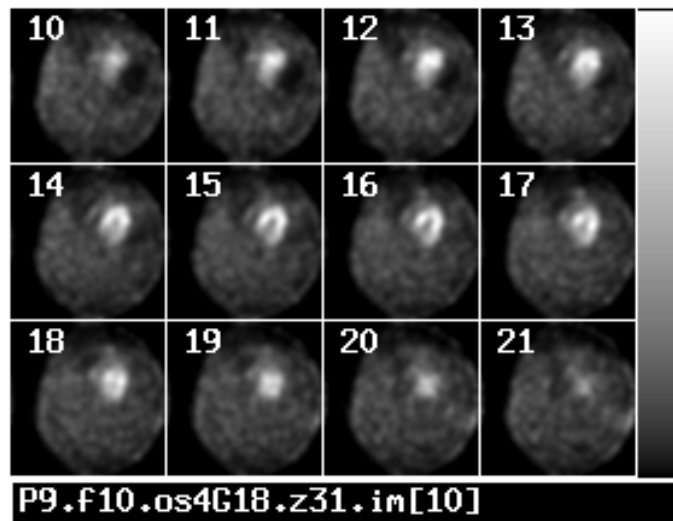
Figure 4.12: Selected transaxial slices of reconstructed images from an obese patient (GCPS 09) who was administered Tc-99m-Tetrofosmin, showing iteration 4 of the image reconstructed with the iterative OS-EM algorithm. This image was further filtered by a 3D Gaussian filter with FWHM of 18mm. The 11th frame of 16 is seen, and the noise level is on the higher side.
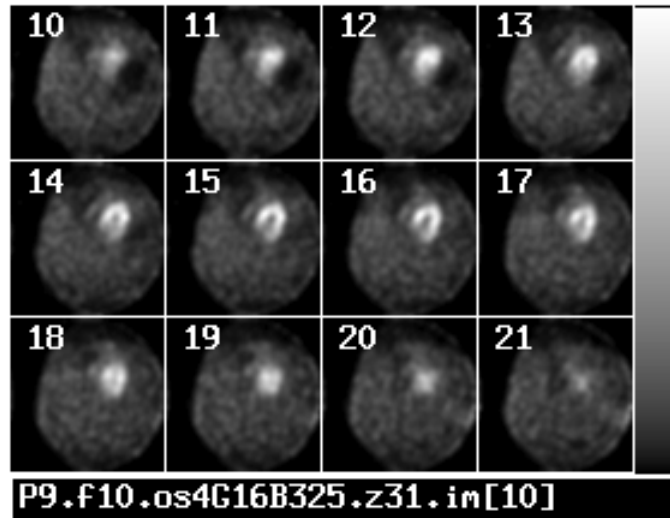
Figure 4.13: Selected transaxial slices of reconstructed images from an obese patient (GCPS 09) who was administered Tc-99m-Tetrofosmin, showing iteration 4 of the image reconstructed with the iterative OS-EM algorithm. The image was post-processed first with a 3D Gaussian filter with FWHM of 16mm, then a 4D order 8 Butterworth filter with cutoff of 0.325 cycles/pixel. The 11th frame of 16 is seen, and the noise level is on the higher side.
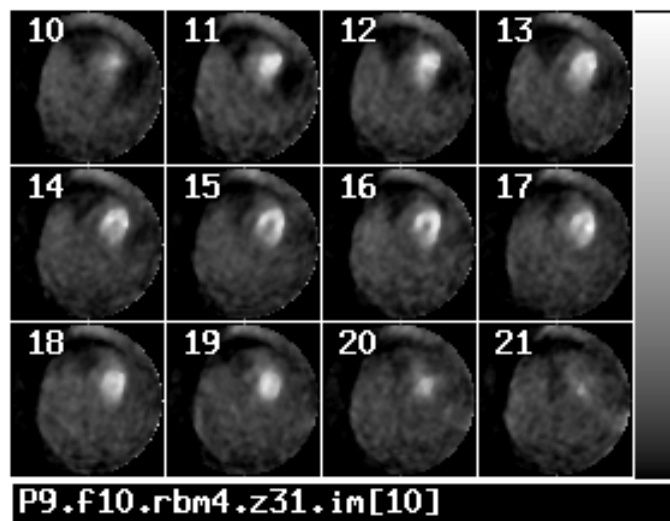
Figure 4.14: Selected transaxial slices of reconstructed images from an obese patient (GCPS 09) who was administered Tc-99m-Tetrofosmin, showing iteration 4 of the image reconstructed with the 4D RBI-MAP algorithm; the 11th frame of 16 is seen. The noise level is on the higher side.
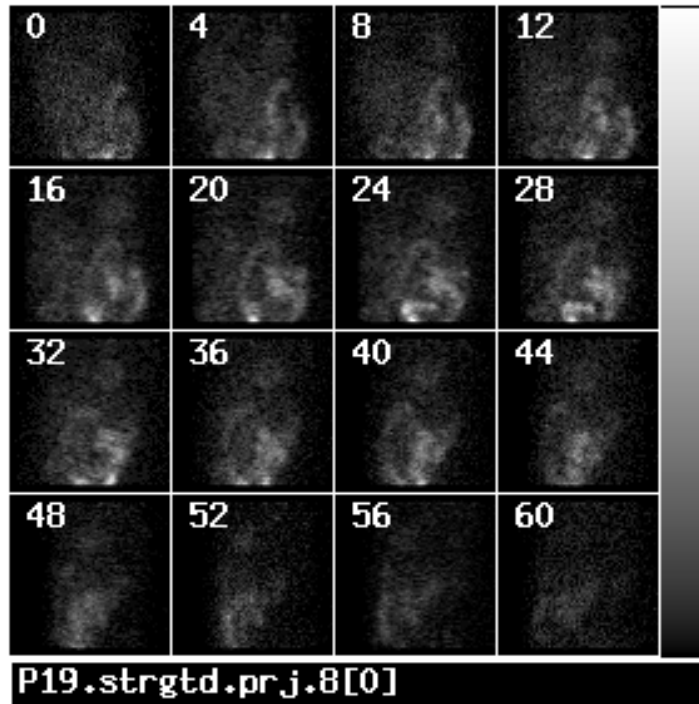
Figure 4.15: Selected views of projection data from the stress image of an obese patient (GCPS 19) who was administered Tc-99m-Tetrofosmin; this dataset shows the eight frame of the cardiac cycle, out of 16 time frames. This dataset is a noisier dataset, which was closer to the average noise level.
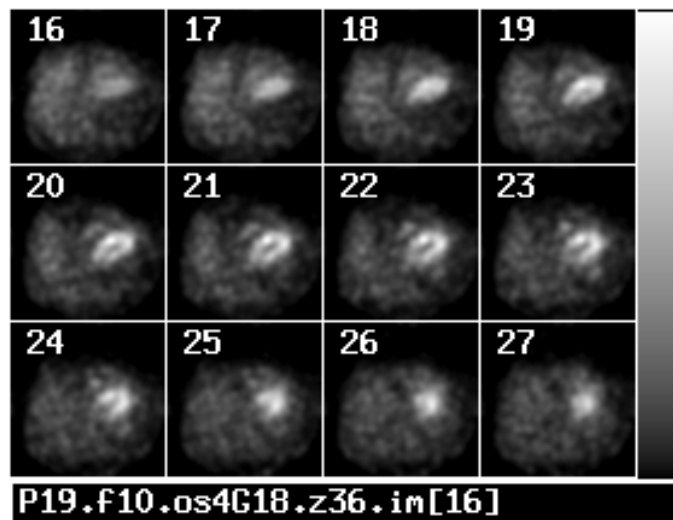
Figure 4.16: Selected transaxial slices of reconstructed images from an obese patient (GCPS 19) who was administered Tc-99m-Tetrofosmin, showing iteration 4 of the image reconstructed with the iterative OS-EM algorithm. This image was further filtered by a 3D Gaussian filter with FWHM of 18mm. The 11th frame of 16 is seen, and the noise level is at the group average.
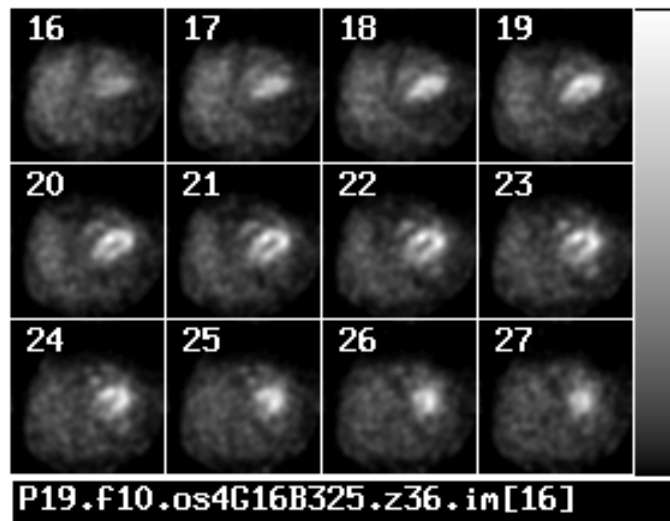
Figure 4.17: Selected transaxial slices of reconstructed images from an obese patient (GCPS 19) who was administered Tc-99m-Tetrofosmin, showing iteration 4 of the image reconstructed with the iterative OS-EM algorithm. The image was post-processed first with a 3D Gaussian filter with FWHM of 16mm, then a 4D order 8 Butterworth filter with cutoff of 0.325 cycles/pixel. The 11th frame of 16 is seen, and the noise level is at the group average.
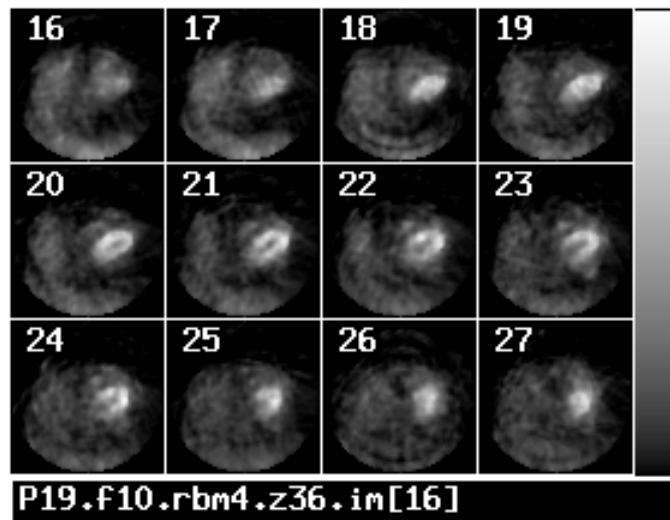
Figure 4.18: Selected transaxial slices of reconstructed images from an obese patient (GCPS 19) who was administered Tc-99m-Tetrofosmin, showing iteration 4 of the image reconstructed with the 4D RBI-MAP algorithm; the 11th frame of 16 is seen. The noise level is at the group average.

Figures 4.12, 4.16, and 4.20 show transaxial slices of reconstructed data from the three obese patients (illustrating low noise, average, and high noise cases), where OS-EM with 3D filtering was used. The heart is most prominently seen in the low noise case where the chamber surfaces appear clearly outlined, while the high noise case shows a blob-like structure to the noise, which obscures the chamber surfaces a bit. The images appear smooth.

Figures 4.13, 4.17, and 4.21 depict transaxial slices of reconstructed data from the same three obese patients, where OS-EM with 4D filtering was used. The same features can be noted about the noise when comparing these images, as in the previous case. Visually, the images reconstructed with 4D filtering appear similar to the ones reconstructed with 3D filtering included. Considering that the main difference between the two methods is the added filtering along the time dimension in the latter, it follows that this 2D medium would be limited in depicting any differences that may be present in the time domain comparison.

Figures 4.14, 4.18, and 4.22 have the transaxial slices of reconstructed data from the obese patients, using the 4D RBI-MAP reconstruction algorithm. Visually, these images show better resolution and less noise degradation than images reconstructed with the OS-EM algorithm. It appears that in the high noise case, due to the differing noise structure brought about by the application of the smoothing priors used, this algorithm is able to bring about smoother images of the heart than the OS-EM methods. The difference in the time domain smoothing will have to be judged by means of moving images.
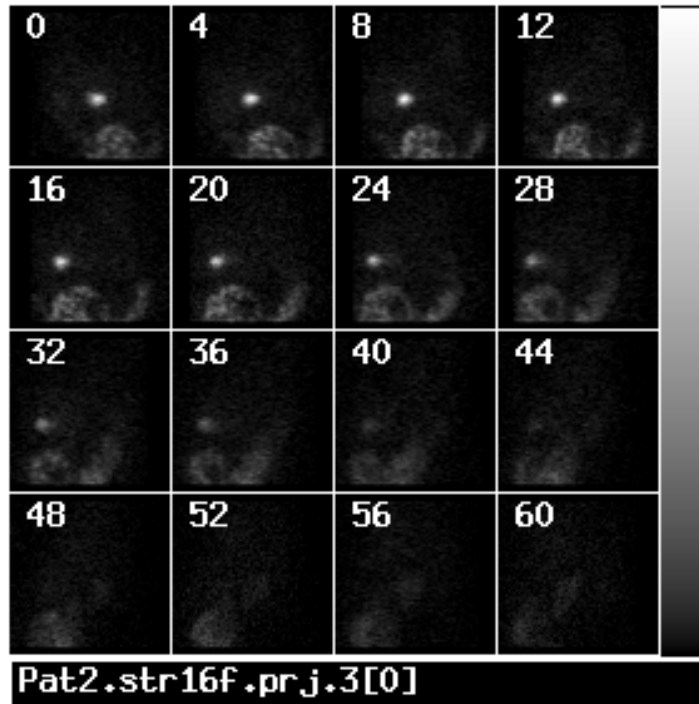
Figure 4.19: Selected views of projection data from the stress image of an obese patient (GCPS 2) who was administered Tc-99m-Tetrofosmin; this dataset shows the second frame of the cardiac cycle, out of 16 time frames. This dataset had the highest noise level out of all the patients in the study.
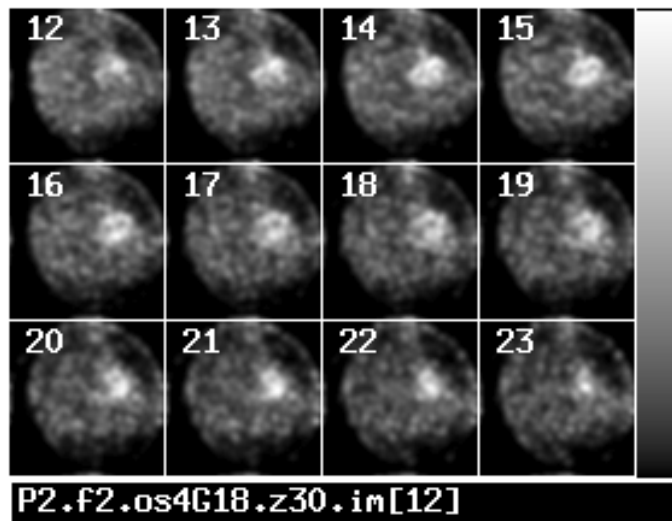
Figure 4.20: Selected transaxial slices of reconstructed images from an obese patient (GCPS 2) who was administered Tc-99m-Tetrofosmin, showing iteration 4 of the image reconstructed with the iterative OS-EM algorithm. This image was further filtered by a 3D Gaussian filter with FWHM of 18mm. The 2nd frame of 16 is seen, and the noise level is the highest of all patients in the study.

56

P2.f2.os4G16B325.z30.im[12]
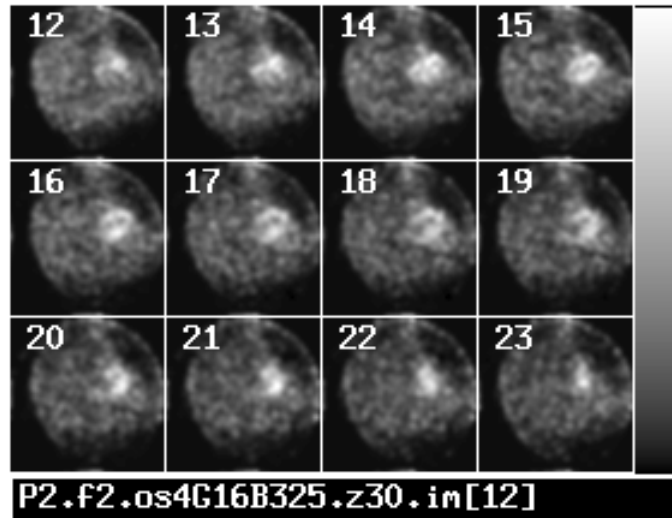
Figure 4.21: Selected transaxial slices of reconstructed images from an obese patient (GCPS 2) who was administered Tc-99m-Tetrofosmin, showing iteration 4 of the image reconstructed with the iterative OS-EM algorithm. The image was post-processed first with a 3D Gaussian filter with FWHM of 16mm, then a 4D order 8 Butterworth filter with cutoff of 0.325 cycles/pixel. The 2nd frame of 16 is seen, and the noise level is the highest out of all patients in the study.

P2.f2.rbm4.z30.im[12]
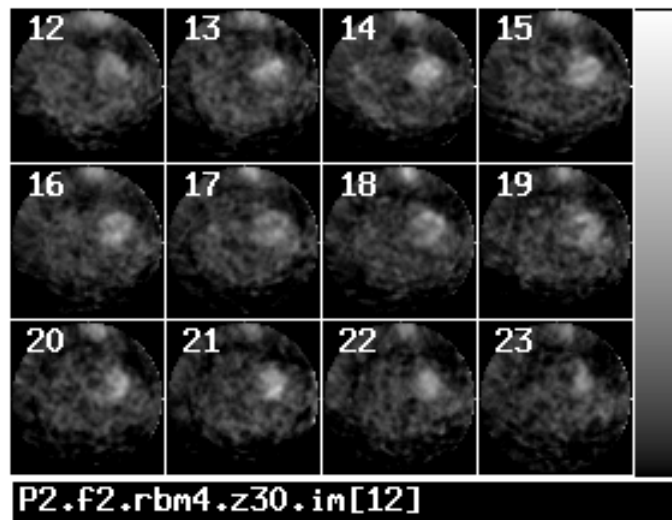
Figure 4.22: Selected transaxial slices of reconstructed images from an obese patient (GCPS 2) who was administered Tc-99m-Tetrofosmin, showing iteration 4 of the image reconstructed with the 4D RBI-MAP algorithm; the 2nd frame of 16 is seen. The noise level is highest out of all patients in the study.

It is difficult to draw too many conclusions about the images from a 2D

comparison, since 2D media are limited in displaying motion. Observations of

interleaved AVI loops of the images, however, revealed that RBI-MAP seems to provide

57

a more contiguous representation of the myocardium as compared to the noisy appearance of the non-MAP results, especially in the higher noise cases. It was also noted that though the noise variances were set comparably, the noise textures still differ a fair bit between the OS-EM-reconstructed images and the RBI-MAP-reconstructed images.

4.1.3 Phantom Simulation

Table 4.1 shows relative uptake ratios of various organs in a Tc-99m tetrofosmin model of the XCAT phantom, which attempts to model the biokinetics of the tracers in the fast blood and liver clearance, combined with high intestinal uptake.

Selected transaxial slices of attenuation maps and tetrofosmin activity distributions of the physiologically normal morbidly and moderately obese male and female phantoms are shown below in Figures 4.23, 4.24, 4.25 and 4.26. The heart sizes were scaled to be realistic in proportion to the body size, and the same was done with the breasts in the female phantoms.

Table 4.1: Tc-99m uptake ratios for the XCAT phantom that simulate a tetrofosmin activity distribution

Organ	Relative Activity Units (/voxel)
Left Ventricle Myocardium	20
Left Atrium Myocardium	20
Right Ventricle Myocardium	18
Right Atrium Myocardium	18
Blood Pool	2
Lung	2
Liver	2
Gall Bladder	2
Stomach	2
Body	2
Bone	2
Intestine	80
Other pelvic organs	2

`fz.OMSn_atn_av.im[0]`   `fz.OMSn_act_av.im[4]`
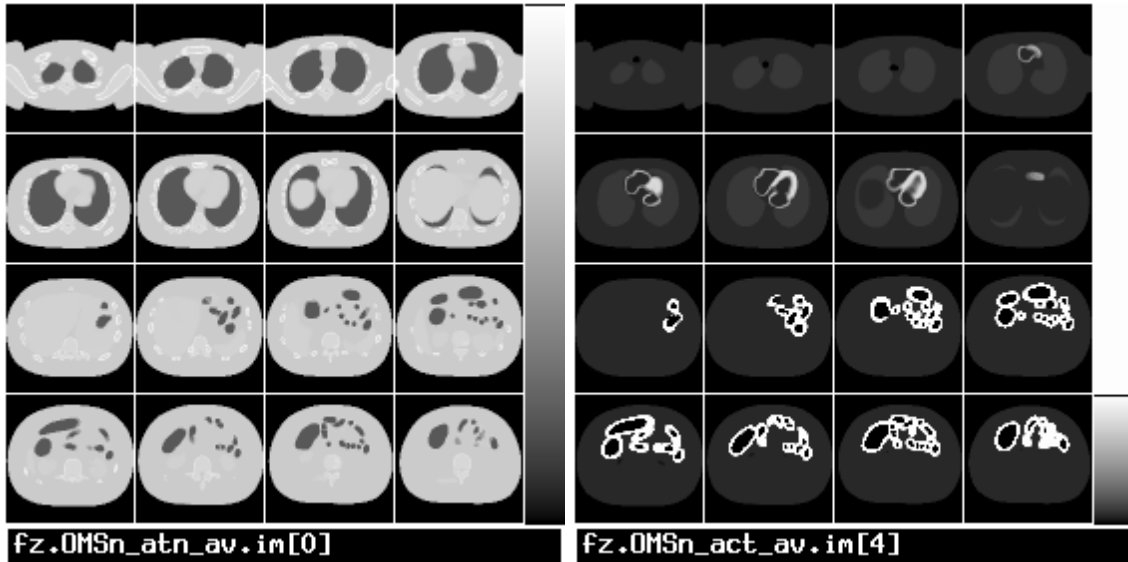
Figure 4.23: Selected transaxial slices showing the attenuation (left) and activity maps (right) of the morbidly obese male phantom, modeling a Tc-99m tetrofosmin activity distribution in a matrix size of 64x64, and a pixel size of 0.65913 cm; the average activity map (of 16 bins) is shown.

`fz.OFSn_atn_av.im[0]`   `fz.OFSn_act_av.im[8]`
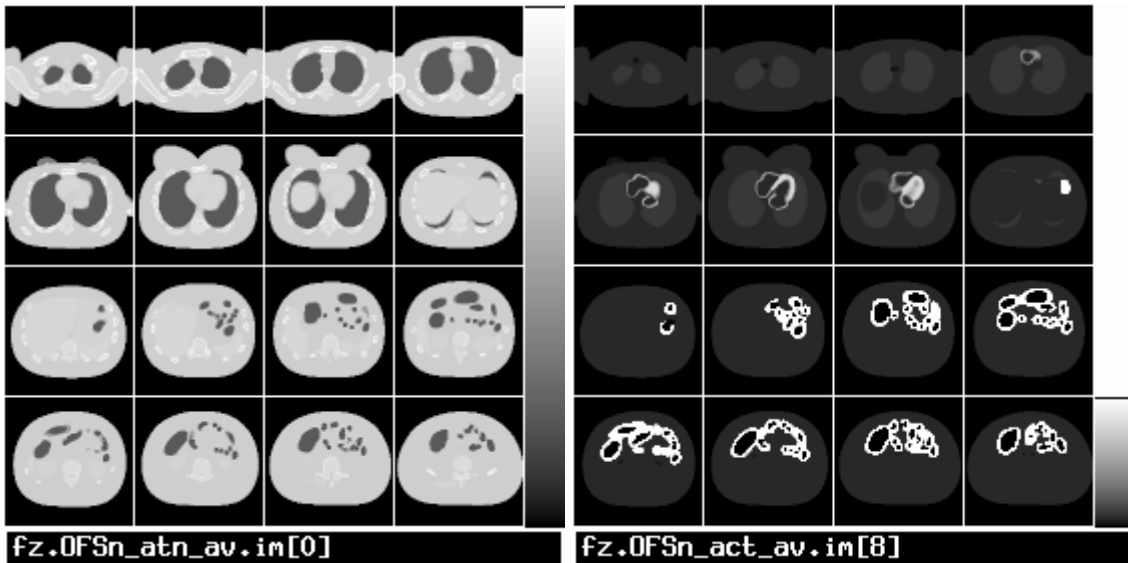
Figure 4.24: Selected transaxial slices showing the attenuation (left) and activity maps (right) of the morbidly obese female phantom, modeling a Tc-99m tetrofosmin activity distribution in a matrix size of 64x64, and a pixel size of 0.65913 cm; the average activity map (of 16 bins) is shown

`fz.mOMvH_atn_av.im[0]` `fz.mOMvH_act_av.im[0]`
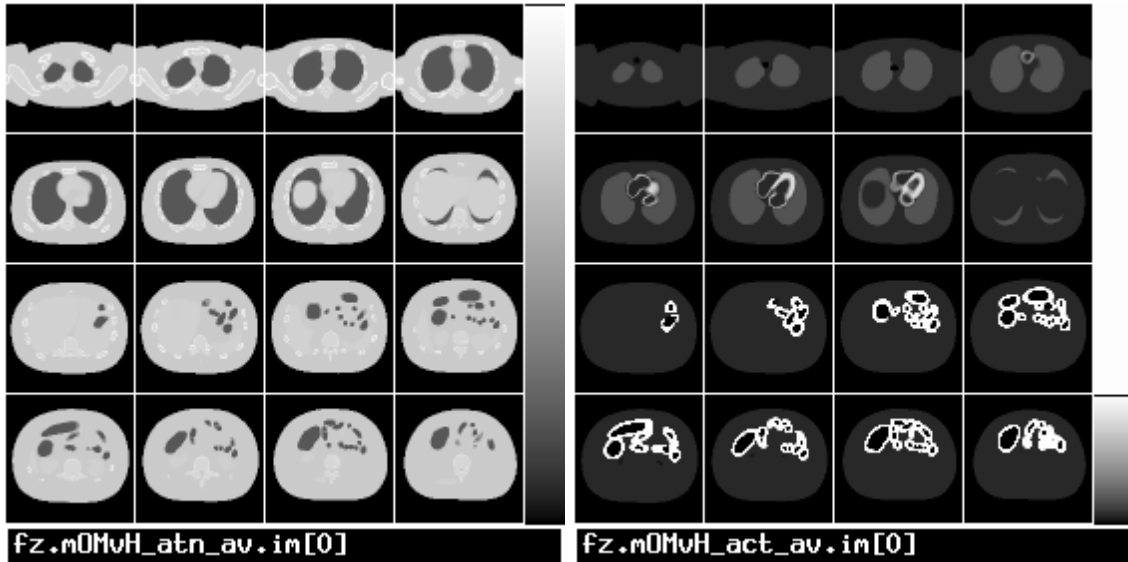
Figure 4.25: Selected transaxial slices showing the attenuation (left) and activity maps (right) of the moderately obese male phantom, modeling a Tc-99m tetrofosmin activity distribution in a matrix size of 64x64, and a pixel size of 0.65913 cm; the average activity map (of 16 bins) is shown

`fz.mOFvH_atn_av.im[0]` `fz.mOFvH_act_av.im[0]`
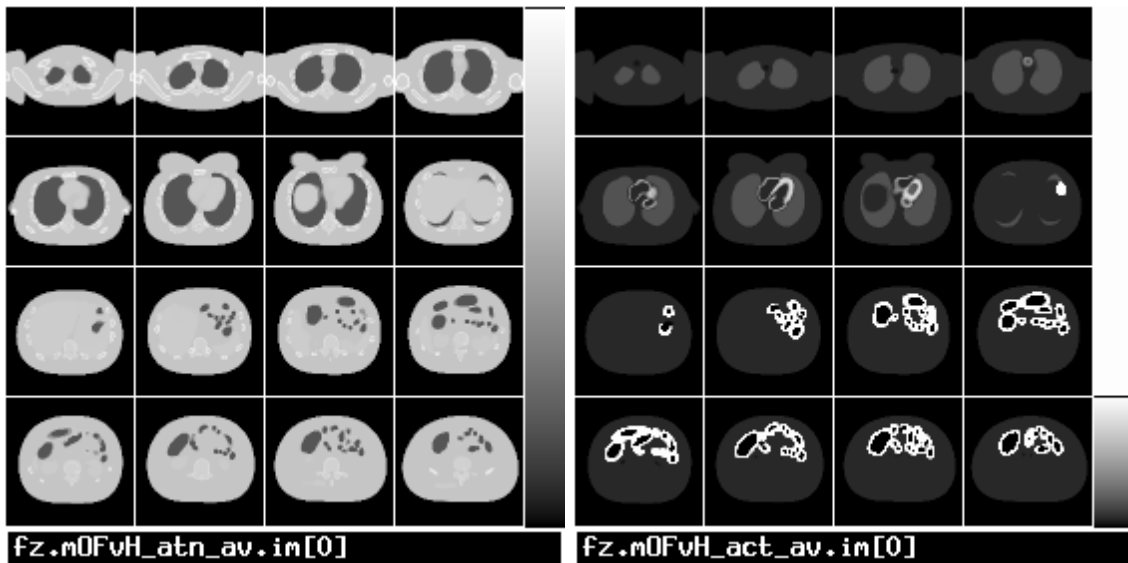
Figure 4.26: Selected transaxial slices showing the attenuation (left) and activity maps (right) of the moderately obese female phantom, modeling a Tc-99m tetrofosmin activity distribution in a matrix size of 64x64, and a pixel size of 0.65913 cm; the average activity map (of 16 bins) is shown

60

Figure 4.27: Selected transaxial view of the activity map of the physiologically normal, morbidly obese male phantom simulating Tc-99m tetrofosmin uptake. The 1st, 5th, 9th and 13th time frames of 16 are shown.

Figure 4.28: Selected transaxial view of the activity map of the mildly hypokinetic, morbidly obese male phantom simulating Tc-99m tetrofosmin uptake. The 1st, 5th, 9th and 13th time frames of 16 are shown.

Figure 4.29: Selected transaxial view of the activity map of the severely hypokinetic, morbidly obese male phantom simulating Tc-99m tetrofosmin uptake. The 1st, 5th, 9th and 13th time frames of 16 are shown.

Figures 4.27 through 4.29 show selected transaxial slices of the activity map of the three different physiological states of the phantoms, as depicted in the morbidly obese male. Figure 4.27 depicts the motion of the left ventricle in the normal heart, while Figure 4.28 shows the mildly hypokinetic case where the lateral wall was affected. In Figure 4.29, very little left ventricle motion is apparent, due to the fact that the lateral, anterior and inferior walls were fixed (i.e. no motion) in the model simulating the severely hypokinetic case.

Figures 4.30 and 4.31 depict selected views of noisy projection data from the morbidly obese male phantom and the moderately obese female phantom, respectively. It

is noted that they are very similar in appearance to the projection data from the patient in terms of organ radiopharmaceutical uptake. There is heightened uptake in the intestines combined with rapid clearance from the liver as is typical for tetrofosmin studies. The noise level was set to 120,000 counts, as it was the average noise level in the patient study. Six noise realizations were simulated for each of the phantoms in the study.
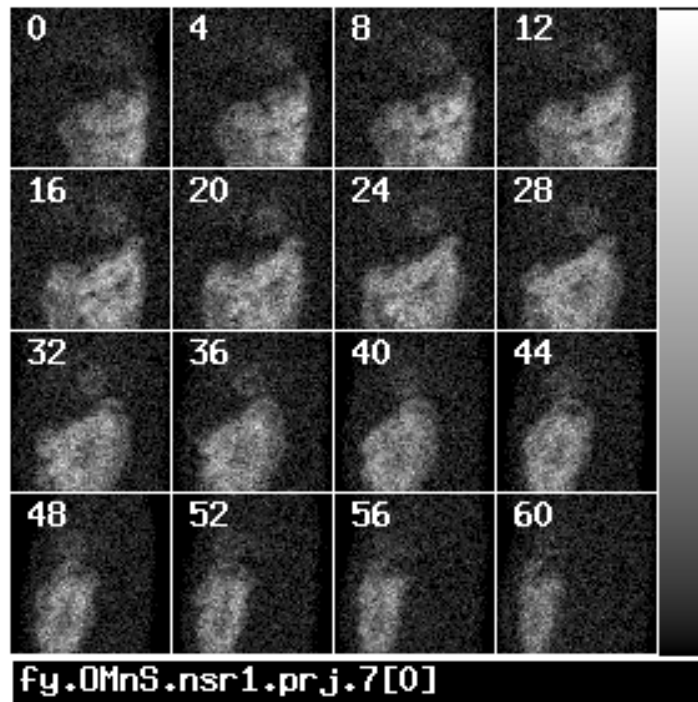
Figure 4.30: Selected views of simulated projection data from the physiologically normal morbidly obese male phantom simulating Tc-99m tetrofosmin uptake. The image was scaled to 120,000 counts before adding noise; the first noise realization is shown.

Reconstructed images from the morbidly obese male phantom are depicted in Figures 4.32 to 4.34. Similar to the patient reconstructed images, these images reconstructed with the 4D RBI-MAP algorithm show better image resolution and less noise degradation, than images reconstructed with OS-EM methods with 3D and 4D filtering. As in the case of the patients, it is not easy to distinguish differences between

62

the 3D and 4D filtered images from the OS-EM method, due to the limitations of the 2D

display.
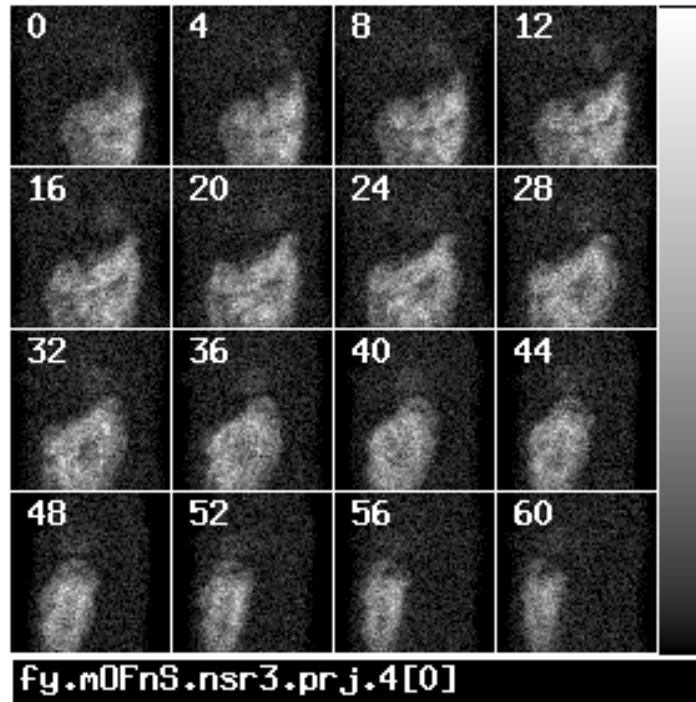
Figure 4.31: Selected views of simulated projection data from the physiologically normal morbidly obese female phantom simulating Tc-99m tetrofosmin uptake.
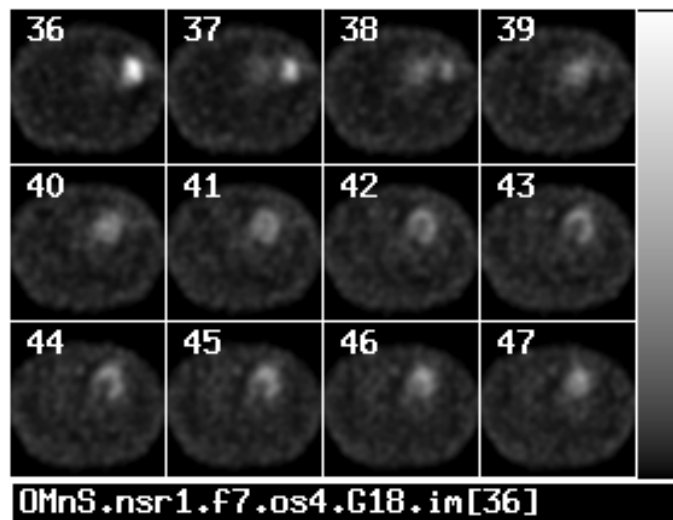
Figure 4.32: Selected transaxial slices of reconstructed images from the morbidly obese male phantom. The image was processed with the OS-EM algorithm, and the 4th iteration was further filtered with a 3D Gaussian filter with FWHM of 18mm. The 7th time slot is shown here.

63
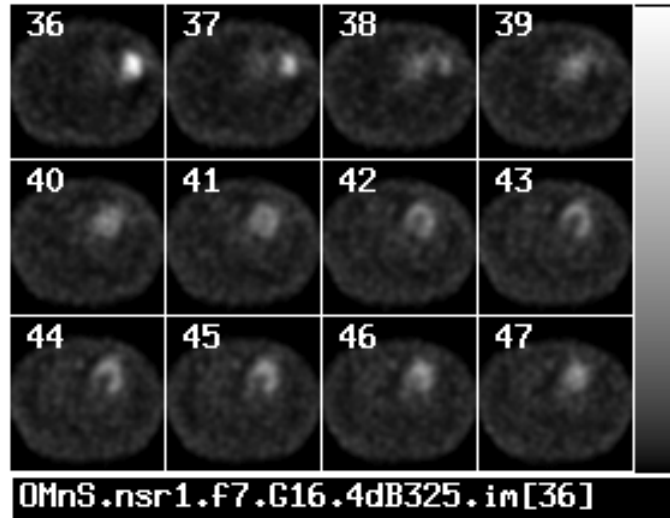
Figure 4.33: Selected transaxial slices of reconstructed images from the morbidly obese male phantom. The 4th iteration OS-EM image shown was processed with a 3D Gaussian with FWHM of 16mm, followed by an order 8 4D Butterworth filter with a filter cutoff of 0.325 cycles/pixel. The 7th time slot is shown here.
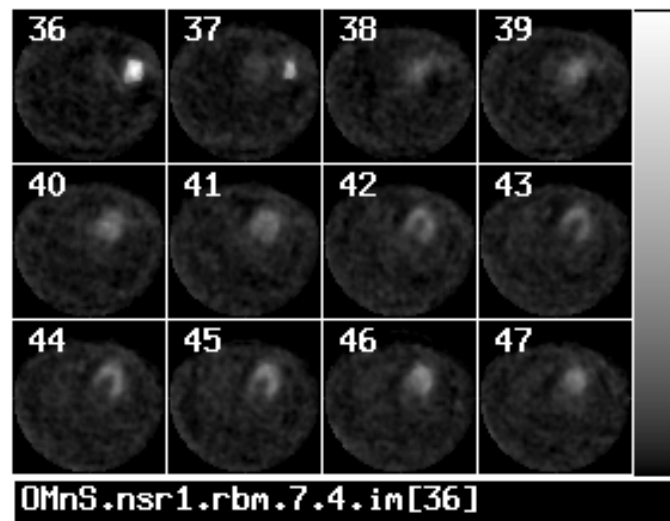
Figure 4.34: Selected transaxial slices of reconstructed images from the physiologically normal morbidly obese male phantom. The image was processed with the 4D RBI-MAP algorithm with the same parameters as the patient image. The 4th iteration of time slot 7 is shown here.

4.2 Evaluation of Quantitative Accuracy and Motion Fidelity

This next study was meant to investigate the quantitative accuracy and motion fidelity of the three reconstruction methods, using patient studies and phantoms.

64

4.2.1 Conversion of Images to DICOM Format

The reconstructed images of the patients and the phantoms were converted to DICOM using a MATLAB program, by copying the pixel data into existing DCM files. Upon importing to the clinical workstation, the metadata/headers were changed to reflect the reconstruction method actually used. The reorientation program on the clinical workstation was used to reorient the heart data to clearly display the VLA, HLA and SA slices. Masking was done in some cases if a hot spot nearby required it, and all of these operations resulted in a set of 3 files labeled Method A, B, and C in the clinical patient database list view. These files were then selected to import into QGS, and were able to be viewed simultaneously.

4.2.2 QGS Evaluation of Patient Data

Projection data from all 28 patients in the database were reconstructed with each of the three methods; OS-EM with the 3D smoothing filter, OS-EM with the 4D smoothing filter, and the RBI-MAP algorithm with different spatial & time priors for differential smoothing in those dimensions. The conversion to DICOM was accomplished as described before, and the data were imported onto the clinical workstation, and into QGS after a few operations described in the last section. The QGS software generated a set of quantitative parameters, the EDV, ESV, and LVEF, and these were further honed with manual contour fitting around the epicardial surface of the left ventricle, to ensure accuracy of fit. There was no option to fit the endocardial surface. The manual contour fitting made a difference in the noisier datasets, where the QGS left ventricle segmentation fared poorly. The EF, EDV and ESV values were recalculated after the manual-fit contours were processed, and the values were carefully recorded in

Tables 4.2, 4.3 and 4.4 below, that also capture the gender and the diagnosis recorded in

the radiology report.

Table 4.2: Table showing the LVEF values yielded by QGS on the study patients in the database. The gender and diagnosis are also recorded here.

Patient	LVEF Values in QGS (%)			Gender	Diagnosis
	OS4-3D	OS4-4D	RBM-4D		
GCPS 01	55	67	40	Male	Normal
GCPS 02	65	69	52	Female	Normal
GCPS 03	80	87	69	Female	Abnormal
GCPS 04	49	59	49	Female	Abnormal
GCPS 05	65	73	55	Male	Normal
GCPS 06	95	89	145	Female	Abnormal
GCPS 07	42	48	45	Female	Normal
GCPS 08	44	45	44	Female	Normal
GCPS 09	60	74	56	Male	Normal
GCPS 10	68	78	64	Female	Normal
GCPS 11	66	72	60	Male	Normal
GCPS 12	23	30	16	Male	Abnormal
GCPS 13	43	42	39	Male	Normal
GCPS 14	63	72	57	Female	Normal
GCPS 15	63	85	66	Female	Normal
GCPS 16	68	72	60	Female	Normal
GCPS 18	63	61	52	Male	Abnormal
GCPS 19	36	45	43	Female	Abnormal
GCPS 20	67	73	61	Female	Normal
GCPS 21	53	57	51	Female	Normal
GCPS 22	63	74	59	Male	Normal
GCPS 23	55	61	50	Female	Normal
GCPS 24	28	35	26	Male	Abnormal
gcp0016	37	44	36	Male	Normal
gcp0017	63	78	53	Female	Normal
gcp0018	47	36	56	Female	Abnormal
gcp0019	49	56	42	Female	Normal
gcp0021	29	34	30	Female	Normal

Table 4.3: Table showing the end-diastolic volumes recorded for each of the patients in the database, for each of the reconstruction methods used.

Patient	EDV Values in QGS (mL)		
	OS4-3D	OS4-4D	RBM-4D
GCPS 01	105	88	114
GCPS 02	57	94	59
GCPS 03	33	52	34
GCPS 04	99	80	92
GCPS 05	62	105	65
GCPS 06	95	89	145
GCPS 07	171	159	154
GCPS 08	115	100	102
GCPS 09	102	78	95
GCPS 10	102	86	92
GCPS 11	98	90	105
GCPS 12	352	288	387
GCPS 13	157	143	157
GCPS 14	91	81	89
GCPS 15	82	56	60
GCPS 16	83	69	84
GCPS 18	126	121	147
GCPS 19	176	148	148
GCPS 20	84	70	80
GCPS 21	138	131	132
GCPS 22	98	79	91
GCPS 23	82	63	71
GCPS 24	183	152	173
gcp0016	155	129	139
gcp0017	28	46	31
gcp0018	105	106	92
gcp0019	115	97	111
gcp0021	181	156	182

Table 4.4: Table showing the end-systolic values for each of the reconstruction methods used on each set of patient data

Patient	ESV Values in QGS (mL)		
	OS4-3D	OS4-4D	RBM-4D
GCPS 01	47	29	68
GCPS 02	20	29	28
GCPS 03	6	7	10
GCPS 04	50	33	47
GCPS 05	22	28	30
GCPS 06	47	39	94
GCPS 07	99	82	85
GCPS 08	65	55	57
GCPS 09	41	20	41
GCPS 10	33	19	33
GCPS 11	33	26	42
GCPS 12	270	203	327
GCPS 13	90	83	96
GCPS 14	34	23	38
GCPS 15	30	8	21
GCPS 16	27	19	34
GCPS 18	47	47	72
GCPS 19	112	81	84
GCPS 20	28	19	31
GCPS 21	65	57	64
GCPS 22	36	21	37
GCPS 23	37	25	36
GCPS 24	133	99	129
gcp0016	98	72	89
gcp0017	10	10	14
gcp0018	56	68	41
gcp0019	58	43	65
gcp0021	128	103	127

The paired t-tests that were performed, comparing the EDV, ESV, and EF values between OS-EM with 3D filter (OS3D), OS-EM with 4D filter (OS4D), and RBI-MAP (RBM), yielded a set of p values shown in Table 4.5 below; significant values are italicized. The null hypothesis, as stated before, is that the mean difference between paired groups is zero, and a significance level of 0.05 was used. The p values resulting from comparisons of OS3D with OS4D were very small, and thus the null hypothesis can be rejected as the two methods are very different. The p values yielded by comparisons

of OS3D with RBM were much larger, and in this case, the null hypothesis cannot be rejected. Comparing the values between OS4D and RBM yielded p values that did not follow a trend; the ESV and EF comparisons resulted in the rejection of the null hypothesis in favor of the alternative, while the EDV comparison did not give clear reason to reject the null hypothesis.

Table 4.5: P-values from paired t-test comparing pairs of the three methods, are shown below. The significance level used was 0.05.

p value	OS3D vs. OS4D	OS3D vs. RBM	OS4D vs. RBM
EDV	*0.007731*	0.608302	0.054858
ESV	*0.000090*	0.202980	*0.001066*
EF	*0.000016*	0.318878	*0.006731*

The results from the paired t-test suggest that the OS4D method is very different from both the OS3D and the RBI-MAP methods. On average, the EDV and ESV values calculated by QGS on the OS4D method tended to be lower than the others, while the LVEF values were comparable. This may be due to the 4D filtering in the OS4D method produces images that throw off the contour-finding algorithms in QGS, or it is possible that the contour fit is better on the OS4D images than the other two. The lack of knowledge about the true chamber volumes in these patients makes it difficult to draw a conclusion.

Comparing the images qualitatively brought a whole new set of considerations into the equation. At lower noise levels, all three images seemed very similar in appearance to one another when viewed in QGS, as supported by Figure 4.35 below. The cine mode however hinted at subtle differences between the methods. While the motion of the OS3D and OS4D images seemed very similar to each other, the RBM image

seemed to have smoother motion that was more realistic than in the previous two methods, which is probably due to better smoothing in the time domain.
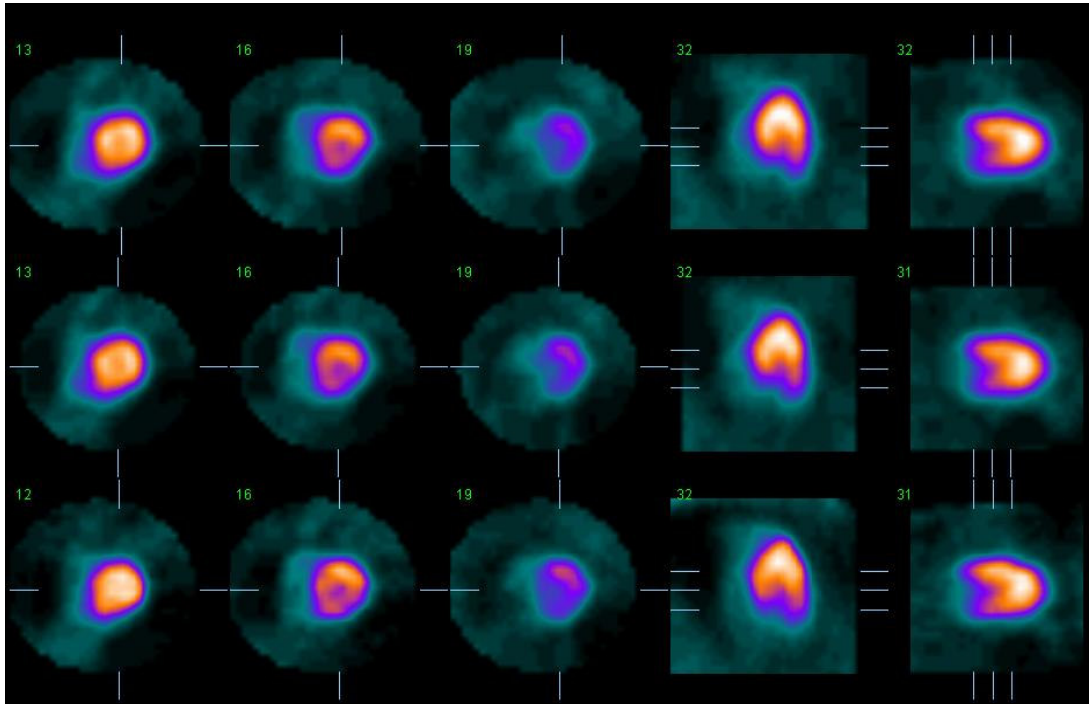
Figure 4.35: 'Slice' display mode in QGS comparing the OS3D-, OS4D- and RBM-reconstructed images for study patient GCPS09 from the database; this illustrates the low noise situation, where the static images are all very similar in appearance.

When viewing noisier images, more differences between the methods were revealed. Image 4.36 depicts the same 'Slice' comparison in a patient with a noisier dataset, where the high noise level translates into images where the entire heart is not visible, especially in the apical region. The OS3D and OS4D appear similar to one another, nearly indistinguishable, while the RBM image shows a striping artifact. The artifact is likely a function of the β parameter used to weight the spatial prior. While viewing the images in cine mode, it seemed once again that the motion of the RBM-reconstructed image was much smoother and more realistic as compared to the OS3D and OS4D images, which were similar to each other.
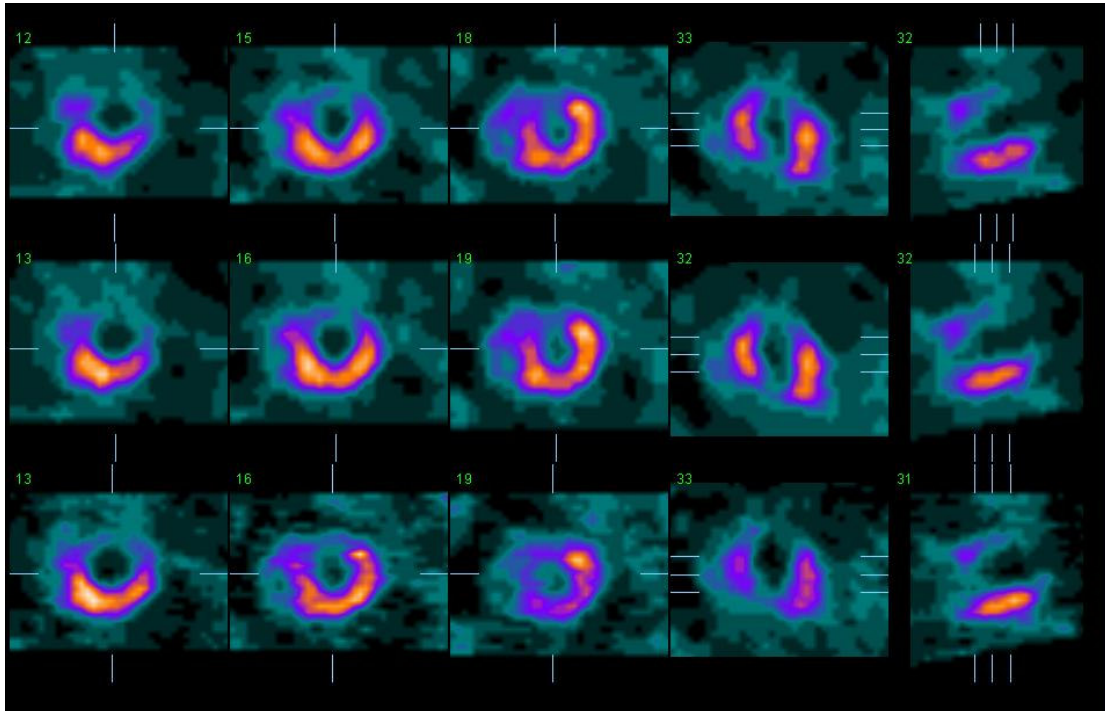
Figure 4.36: 'Slice' display mode in QGS comparing the OS3D-, OS4D- and RBM-reconstructed images for study patient GCPS12 from the database; this illustrates the higher noise situation, where OS3D and OS4D images are similar to one another, while the RBM image shows a striping artifact in the horizontal direction

Having compared the images in high-noise and low-noise situations, one must also view the average situation to be able to draw conclusions. Figure 4.37 shows the average-noise situation, where the striping artifact is once again visible in the RBM images. The images compared similarly as in the previous situations, with the OS3D and OS4D images behaving alike both spatially and temporally, while the RBM image seemed to perform better temporally with smoother motion.
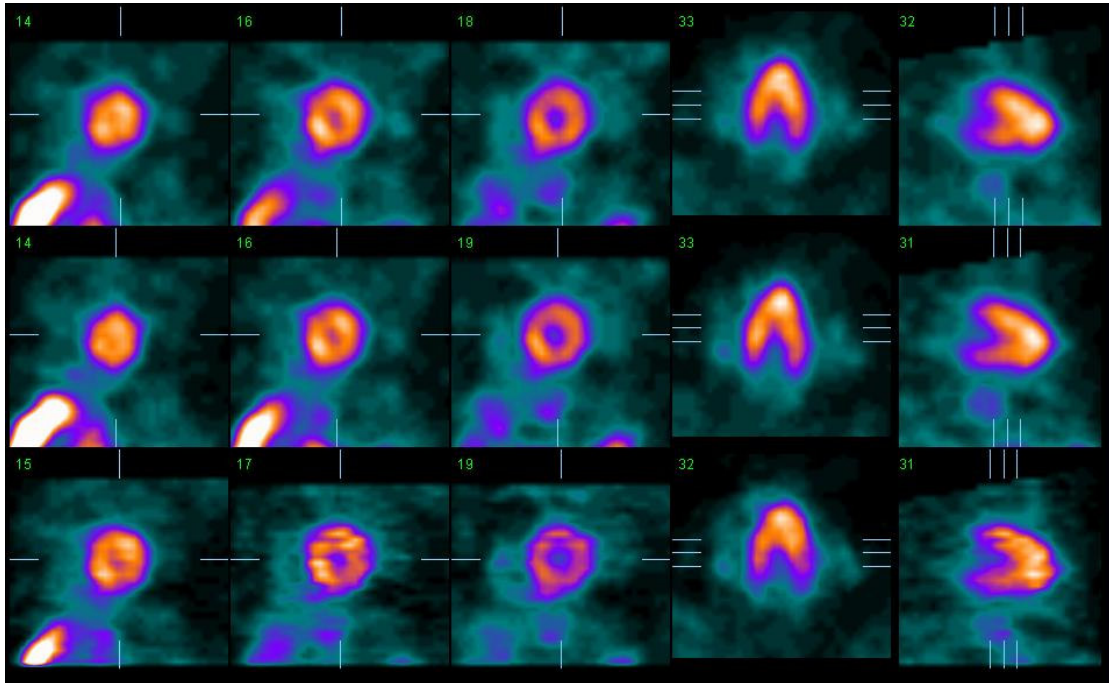
Figure 4.37: 'Slice' display mode in QGS comparing the OS3D-, OS4D- and RBM-reconstructed images for study patient GCPS19 from the database; this illustrates the average noise situation, where OS3D and OS4D images are similar to one another, while the RBM image shows a striping artifact in the horizontal direction

This study illustrates the importance of the noise level on the perceived differences between the reconstruction methods in patients. It is thus of much interest to investigate which of the methods is more quantitatively accurate through the phantom study.

4.2.3 QGS Evaluation of Phantom Data

The phantom study employed the 72 phantoms generated (2 body sizes x 2 genders x 3 different LV motion states x 6 noise realizations), from which projection data were simulated. Six noise realizations of Poisson noise were simulated in the noisefree datasets after scaling to 120,000 counts in the heart region for all the phantoms. The noisy data were reconstructed with each of the three reconstruction methods being tested, as with the patient data. The reconstructed images were converted from .im to DICOM

format, and imported onto clinical workstations. The process of reorienting and optional

masking of hot spots was followed with the phantom data, before the images were loaded

into the QGS software.

Table 4.6: LVEF values recorded from the QGS analysis of phantom data; the values for
each phantom come from an average of the values for the 6 noise realizations

	EF Values	EF Values in QGS (%)		
Phantom	TRUE (mL)	OS4-3D	OS4-4D	RBM-4D
Morbidly Obese, Normal Male	59.98	40	37	34
Mod. Obese, Normal Male	59.78	44	43	40
Morbidly Obese, Normal Female	59.74	38	39	36
Mod. Obese, Normal Female	59.01	54	49	45
Morbidly Obese, Mildly Hypo. Male	44.32	17	19	16
Mod. Obese, Mildly Hypo. Male	43.74	22	22	21
Morbidly Obese, Mildly Hypo. Female	43.89	22	22	18
Mod. Obese, Mildly Hypo. Female	43.12	21	20	20
Morbidly Obese, Very Hypo. Male	27.81	6	6	4
Mod. Obese, Very Hypo. Male	27.3	8	10	8
Morbidly Obese, Very Hypo. Female	27.46	7	8	6
Mod. Obese, Very Hypo. Female	26.75	12	13	11

Table 4.7: EDV values recorded from the QGS analysis of phantom data; the values for
each phantom reflect an average from the 6 noise realizations

	EDV Values	EDV Values in QGS (mL)		
Phantom	TRUE (mL)	OS4-3D	OS4-4D	RBM-4D
Morbidly Obese, Normal Male	155.71	103	125	120
Mod. Obese, Normal Male	112.22	74	78	70
Morbidly Obese, Normal Female	119.56	92	93	86
Mod. Obese, Normal Female	85.66	49	53	51
Morbidly Obese, Mildly Hypo. Male	155.71	124	118	118
Mod. Obese, Mildly Hypo. Male	112.22	85	85	82
Morbidly Obese, Mildly Hypo. Female	119.56	88	101	98
Mod. Obese, Mildly Hypo. Female	85.66	55	53	50
Morbidly Obese, Very Hypo. Male	155.71	126	121	126
Mod. Obese, Very Hypo. Male	112.22	80	83	78
Morbidly Obese, Very Hypo. Female	119.56	80	88	84
Mod. Obese, Very Hypo. Female	85.66	57	56	48

Table 4.8: ESV values recorded from the QGS analysis of phantom data; the values for each phantom reflect an average from the 6 noise realizations

Phantom	ESV Values TRUE (mL)	ESV Values in QGS (mL) OS4-3D	OS4-4D	RBM-4D
Morbidly Obese, Normal Male	62.32	63	80	80
Mod. Obese, Normal Male	45.14	42	44	42
Morbidly Obese, Normal Female	48.14	58	57	55
Mod. Obese, Normal Female	35.14	23	27	33
Morbidly Obese, Mildly Hypo. Male	86.7	103	96	99
Mod. Obese, Mildly Hypo. Male	63.14	67	66	65
Morbidly Obese, Mildly Hypo. Female	67.08	69	79	80
Mod. Obese, Mildly Hypo. Female	48.72	43	43	42
Morbidly Obese, Very Hypo. Male	112.4	119	115	122
Mod. Obese, Very Hypo. Male	81.58	74	76	72
Morbidly Obese, Very Hypo. Female	86.73	75	81	79
Mod. Obese, Very Hypo. Female	62.75	51	49	43

The EF, EDV and ESV values were recorded for each phantom, for each noise realization, and the average values (from the noise realizations) are tabulated above in Tables 4.6 through 4.8. The OS-EM with 3D filtering method tended to yield EDV, ESV and EF values that were closer to the true values than the other methods, though there were fluctuations in individual cases that did not always follow this trend, due to differing noise structures. This is possibly due to the noise structure of OS-EM-reconstructed images, which may allow QGS to more precisely identify the endocardial surface contours. The algorithms in QGS may be written to work with a certain type of noise structure.

The data were also analyzed by means of computing the percent error between known values of EDV, ESV and calculated EF, and measured values using QGS. From the % error calculations for the EDV, ESV, and EF values across the phantom populations, it was seen that the RBI-MAP method (abbreviated RBM) tended to yield lower EF values on the average than the other two methods. It may be that the different

noise structure of the RBI-MAP algorithm challenges the ability of the QGS software algorithm to identify the endocardial surface accurately. It was not possible to rectify this as the manual fit in QGS can be applied only to the epicardial surface of the left ventricle. The % error values for the EF tended to be consistently high as compared to those for the EDV and ESV values, probably due to the dependence of that parameter on the other two.

Figures 4.38 through 4.40 depict the variance of EDV across members of the normal and two hypokinetic populations. Every one of charts shows an underestimation of EDV by the QGS software, ranging from 40-80 mL. In general, the values estimated by the three methods are clustered together on the chart, all showing roughly the same amount of underestimation of chamber volume. The RBI-MAP method varied slightly differently from the other two, as seen in Figure 4.39, and this can be attributed to the different noise structure having an effect on the accurate identification of the endocardial surface by QGS.
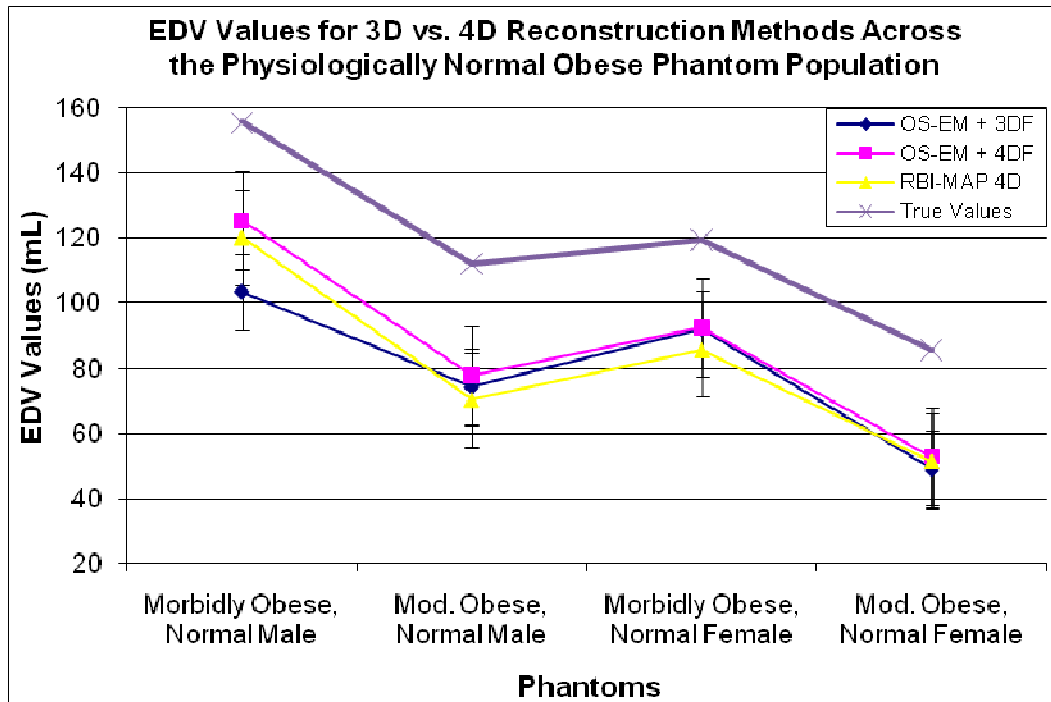
Figure 4.38: Chart showing the EDV values calculated by QGS plotted against the true values, for the physiologically normal obese phantom population. Error bars indicate +/- one standard error.
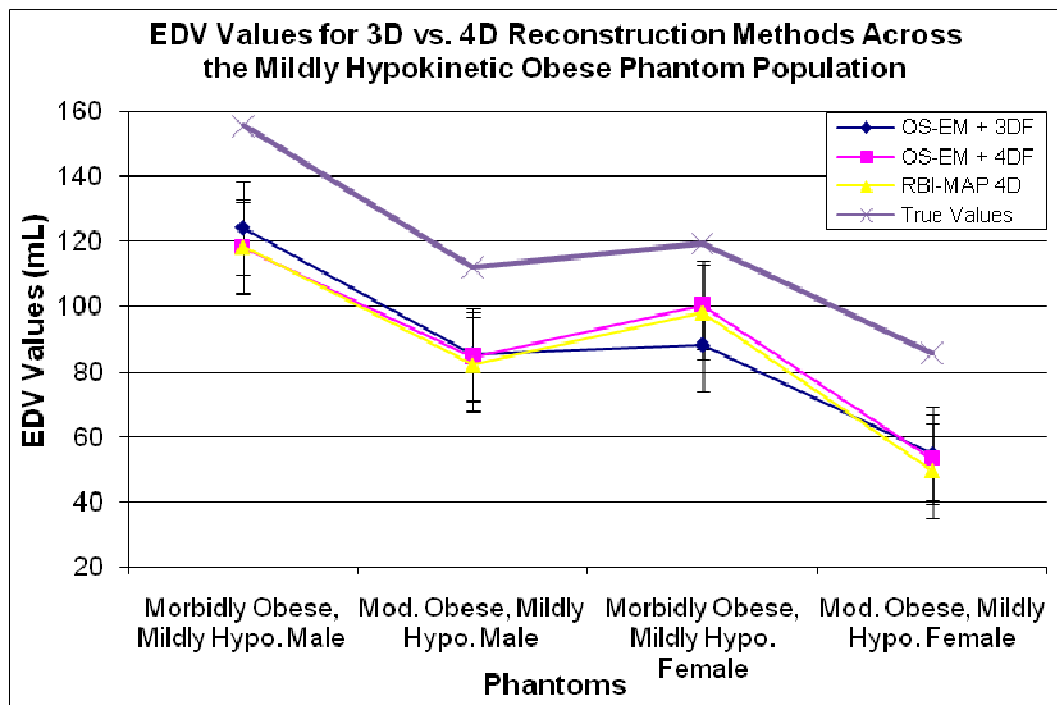
Figure 4.39: Chart showing the EDV values calculated by QGS plotted against the true values, for the mildly hypokinetic obese phantom population. Error bars indicate +/- one standard error.
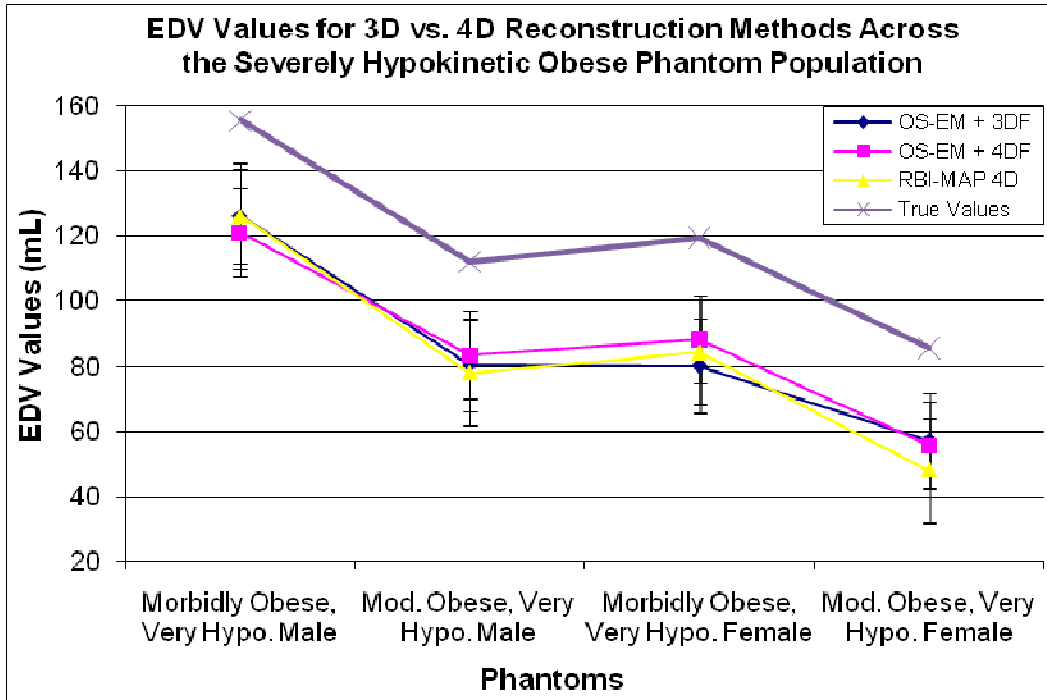
Figure 4.40: Chart showing the EDV values calculated by QGS plotted against the true values, for the severely hypokinetic obese phantom population. Error bars indicate +/- one standard error.
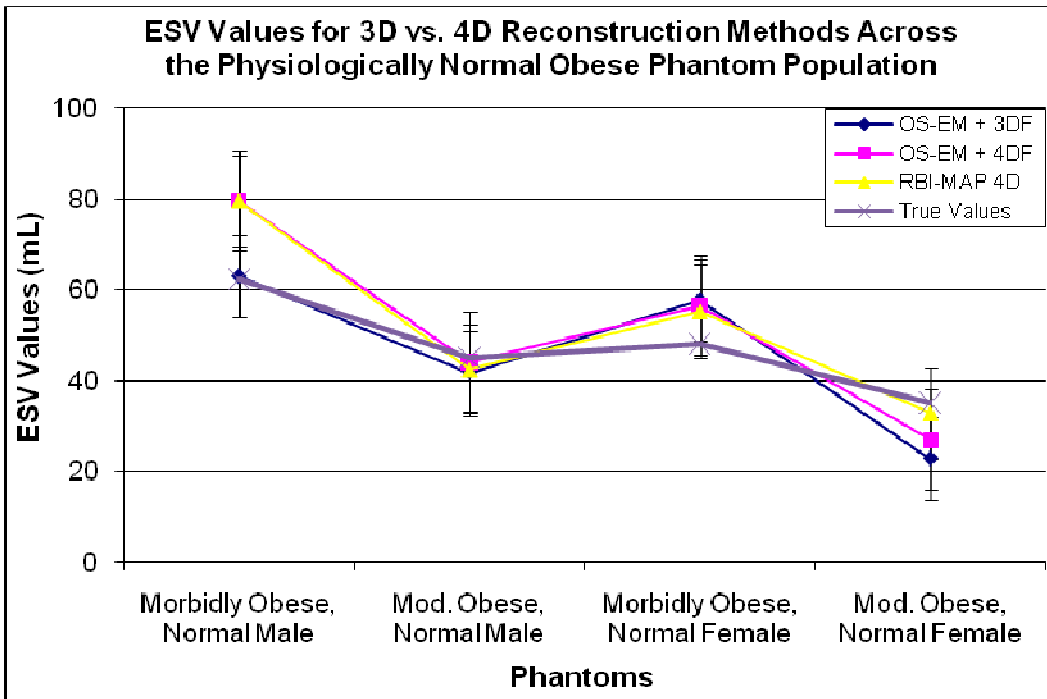
Figure 4.41: Chart showing the ESV values calculated by QGS plotted against the true values, for the physiologically normal obese phantom population. Error bars indicate +/- one standard error.
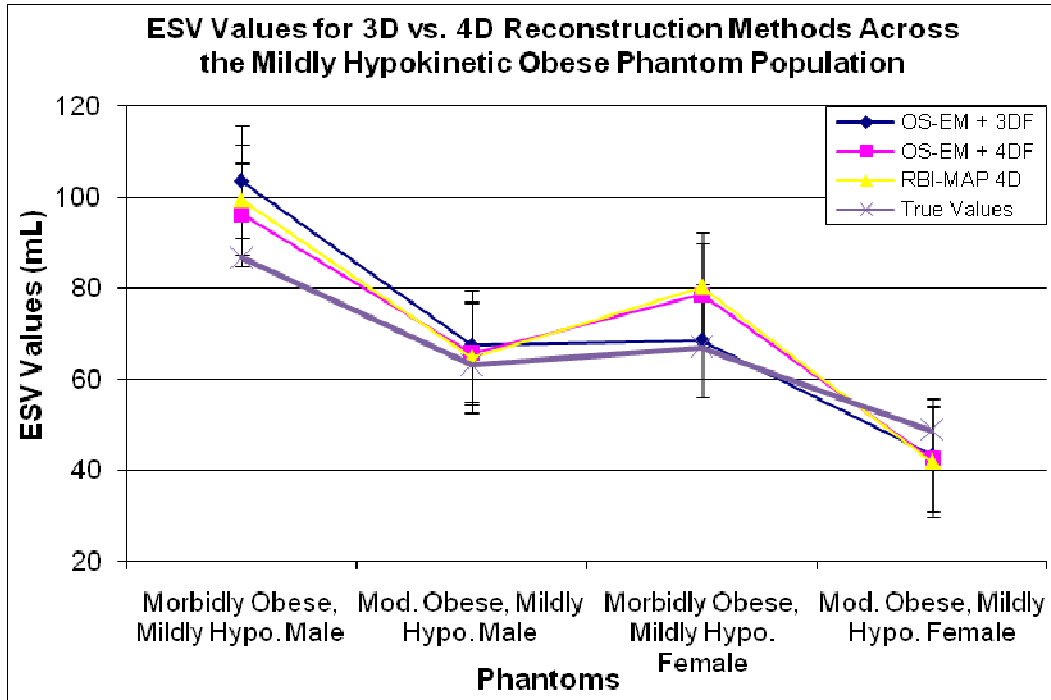
Figure 4.42: Chart showing the ESV values calculated by QGS plotted against the true values, for the mildly hypokinetic obese phantom population. Error bars indicate +/- one standard error.
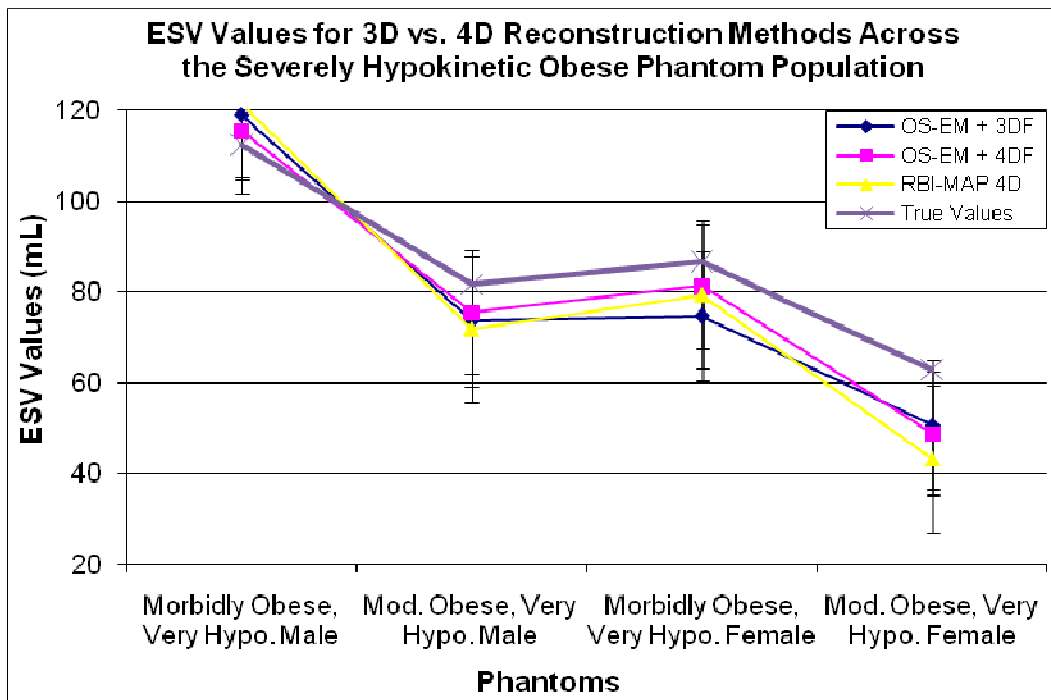
Figure 4.43: Chart showing the ESV values calculated by QGS plotted against the true values, for the severely hypokinetic obese phantom population. Error bars indicate +/- one standard error.

Figures 4.41 through 4.43 show the variance of ESV values across each of the phantom populations, plotted against the true value as calculated from the phantom. QGS appears to have fared much better in estimating ESV values, as the estimated values all vary about the true value, with differences being between 5-20 mL, in contrast to the EDV values. The reason could be that endocardial contours were easier to find for the algorithm at end-systole where counts are concentrated, as opposed to end-diastole when the counts are spread out so there are fewer counts per pixel in the heart. Figure 4.47 illustrates the contour fit in QGS, where it is apparent the endocardial surface fit seems to be clearly erroneous.   The methods once again seemed to differ by roughly equal amounts from the true values, and while there was not a clear distinction, OS-EM with 3D filtering appears to yield values slightly closer to the truth.
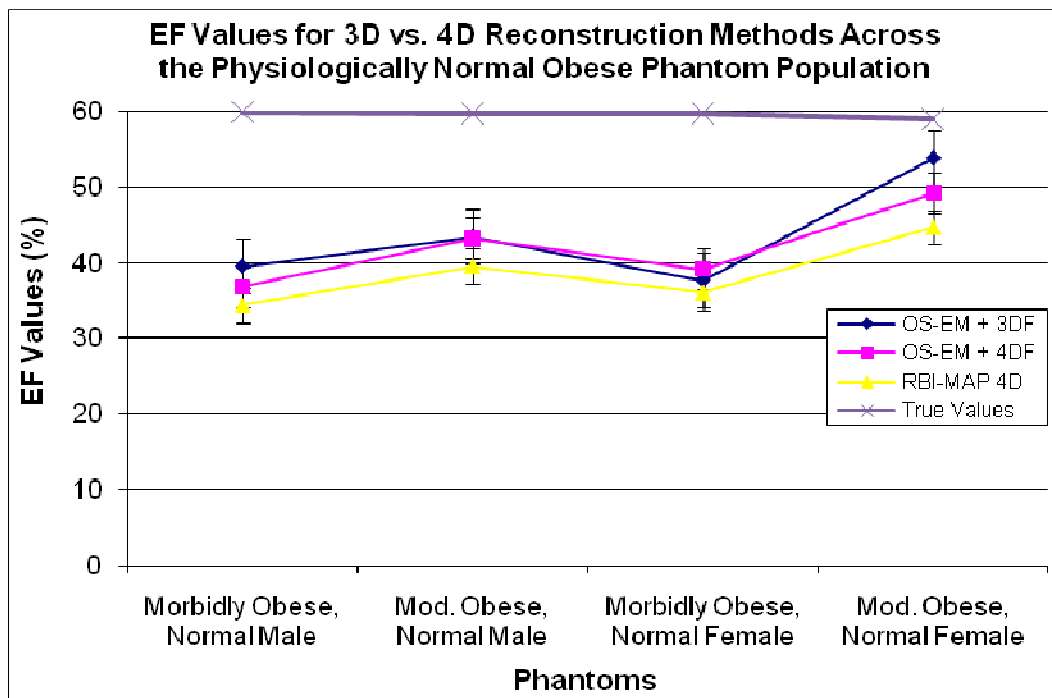
Figure 4.44: Chart showing the EF values calculated by QGS plotted against the true values, for the physiologically normal obese phantom population. Error bars indicate +/- one standard error.
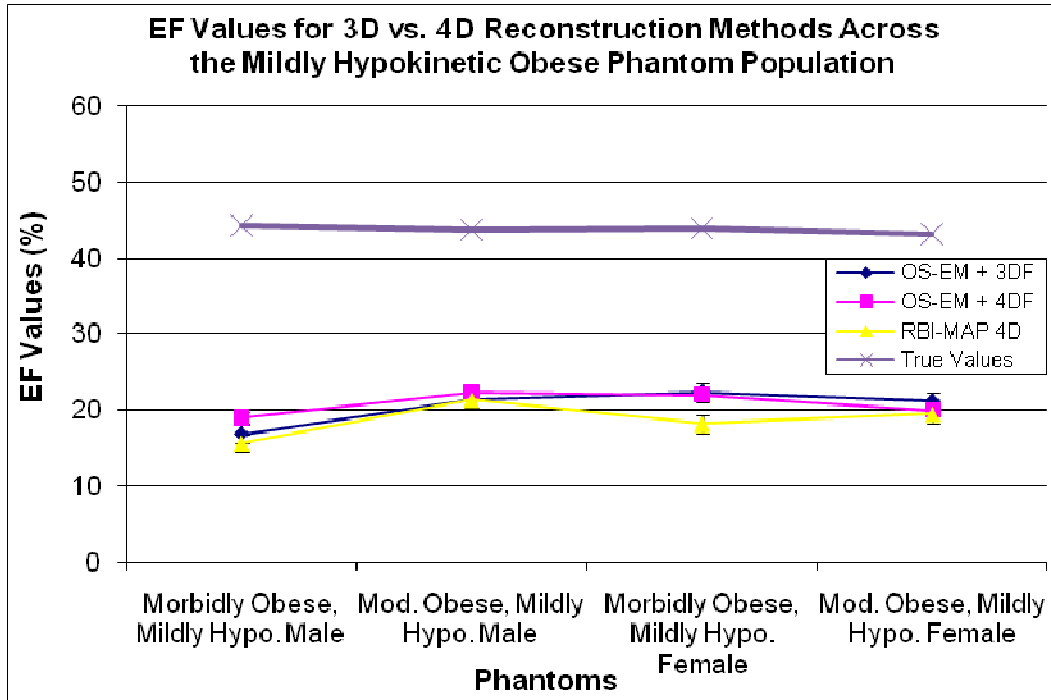
Figure 4.45: Chart showing the EF values calculated by QGS plotted against the true values, for the mildly hypokinetic obese phantom population. Error bars indicate +/- one standard error.
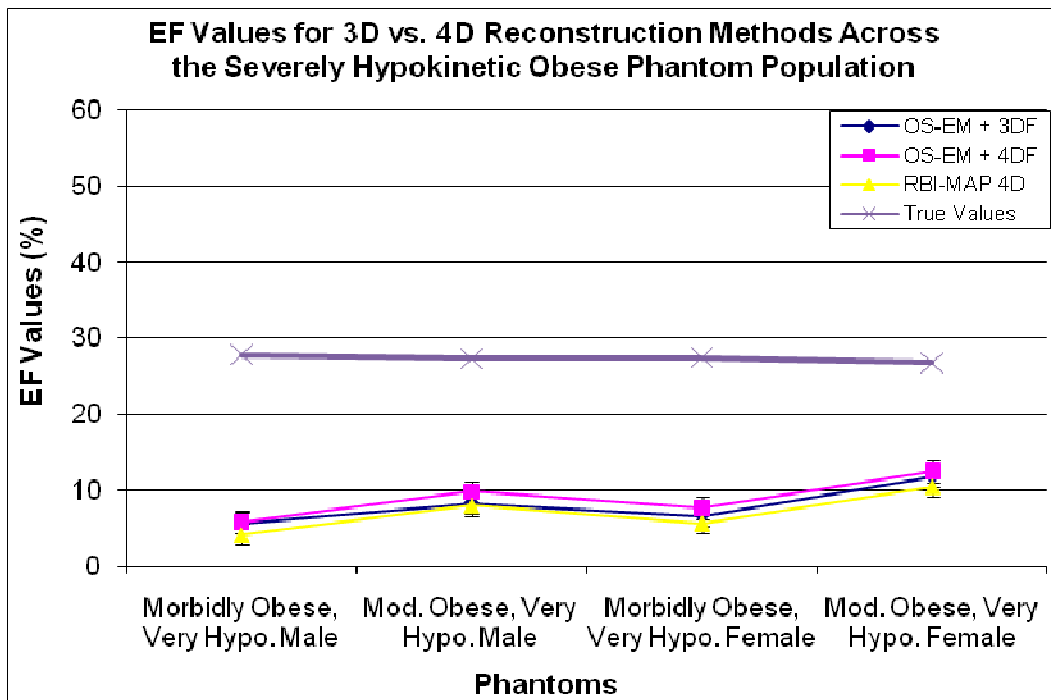
Figure 4.46: Chart showing the EF values calculated by QGS plotted against the true values, for the severely hypokinetic obese phantom population. Error bars indicate +/- one standard error.

Figures 4.44 through 4.46 show QGS-calculated EF values versus true values across the phantom populations in the study. It was in the case of the EF calculation that the greatest % error values were obtained, and that is seen in the chart. The calculated EF values were underestimated in every case, and ranged from 20-30% lower than the true value on average. EF is calculated from the EDV and ESV values, and the size of the error in this case clearly reflects the compounding of the error in the estimation of the two other parameters. The RBI-MAP algorithm seemed to yield the lowest EF values among the three methods, as noted before.

Finally, paired t-tests as in the case of the patient data, were done with the data from the phantom study for each of the quantitative parameters. Tables 4.9 through 4.11 show the breakdown by population (i.e. normal, mildly hypokinetic, and severely hypokinetic); the significant p-values are italicized.

Table 4.9: Results of the paired t-test comparing EDV, ESV, and EF values for the physiologically normal obese phantom population

p value	OS3D vs. OS4D	OS3D vs. RBM	OS4D vs. RBM
EDV	*0.009603*	0.417106	*0.000943*
ESV	*0.017900*	0.051034	0.755848
EF	*0.106890*	*0.000787*	*0.000023*

Table 4.10: Results of the paired t-test comparing EDV, ESV, and EF values for the mildly hypokinetic obese phantom population

p value	OS3D vs. OS4D	OS3D vs. RBM	OS4D vs. RBM
EDV	0.743742	0.678355	0.482481
ESV	0.976096	0.727803	0.761771
EF	0.595362	*0.009037*	*0.009856*

Table 4.11: Results of the paired t-test comparing EDV, ESV, and EF values for the severely hypokinetic obese phantom population

p value	OS3D vs. OS4D	OS3D vs. RBM	OS4D vs. RBM
EDV	0.628799	0.446347	*0.189593*
ESV	0.695743	0.841861	0.561316
EF	*0.049713*	*0.025494*	*0.000043*

The null hypothesis for the paired t-tests was that the mean difference between paired groups is zero, and a significance level of 0.05 was used. It was noted that in both the hypokinetic populations, most of the p values were large (except in the case of the EF values, which are derived from the EDV and ESV), indicating that there is no reason to reject the null hypothesis. By contrast, the p values yielded by the comparison in the normal population revealed significant differences between the 3D OS-EM method and 4D OS-EM method, as well as the 4D OS-EM method and RBI-MAP. Only the EF value was significantly different in the 3D OS-EM and RBI-MAP methods, but due to it being a derived value, it is perhaps not that significant after all. Overall, it appears that the OS-EM method with 4D filtering stands out, as it did in the patient study. There also appears to be a trend in decreasing p-value with decreasing severity of motion defect. These results suggest that the choice of reconstruction method is more important when there is greater heart motion, alluding to the differences being due to the varied time dimension processing parameters. The processing method thus has the potential to have a greater effect on the diagnosis in the normal or borderline cases, than in cases that may be far gone in terms of disease progression.

Visually, the phantom images appeared similar to the patient images in QGS, as seen in Figures 4.48 and 4.49. The OS-EM with 3D and 4D filtering methods yield images that appeared similar to one another spatially, while the RBI-MAP method had a different noise structure. The striping artifact observed with the patient data was not seen here, however, and this is thought to be due to the fact that the RBI-MAP parameters

were optimized for this particular noise level (calculated as the average noise level in the

patient study), and no such noise correlations occurred with the optimization.
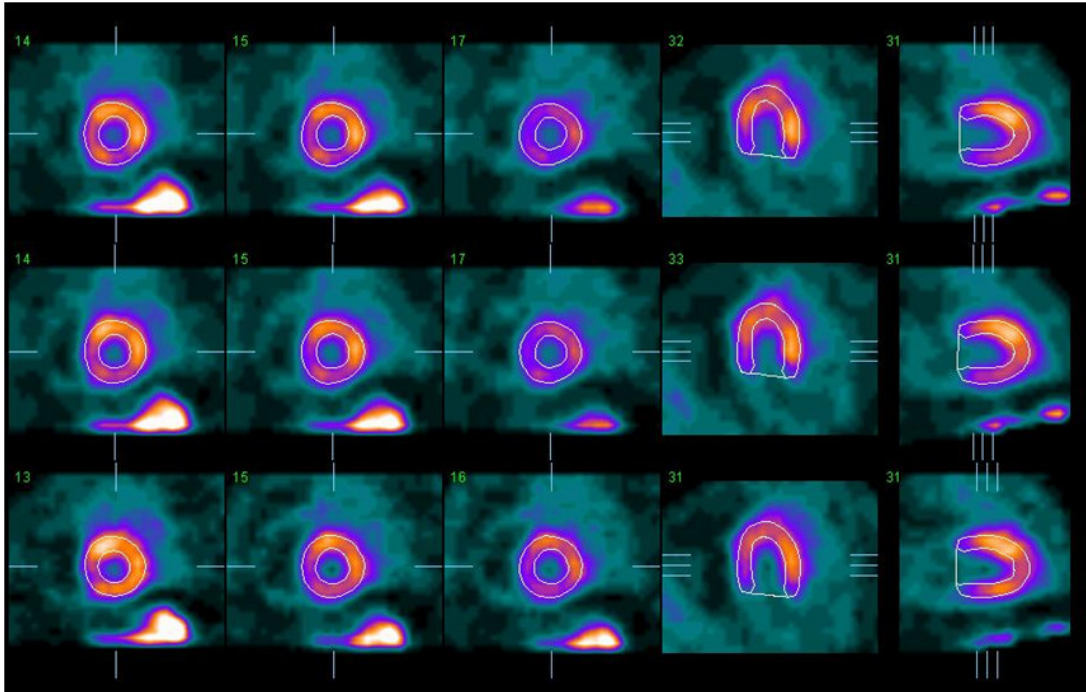
Figure 4.47: 'Slice' display mode in QGS comparing the OS3D-, OS4D- and RBM-reconstructed images for a severely hypokinetic morbidly obese female phantom. The contours generated by the QGS program to the endocardial and epicardial surfaces of the heart are seen here. While the epicardial surface fit may be manually modified, there is no such option for the endocardial surface fit.
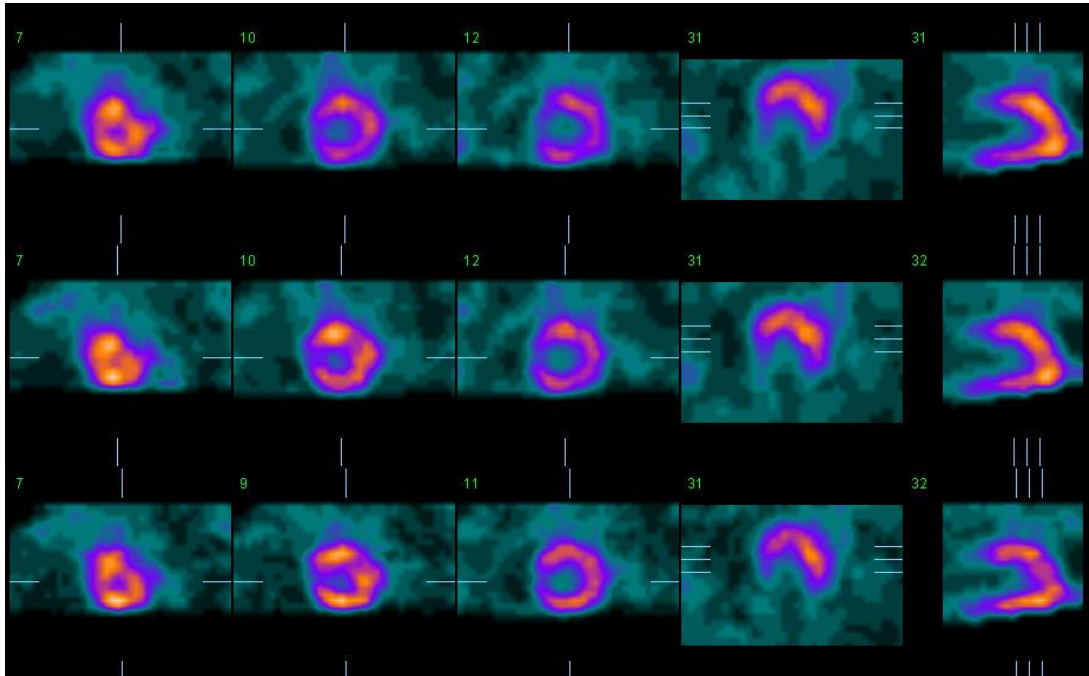
Figure 4.48: 'Slice' display mode in QGS comparing the OS3D-, OS4D- and RBM-reconstructed images for a severely hypokinetic morbidly obese female phantom; this illustrates the average noise level. The OS3D and OS4D images are similar to one another, while the RBM image does not show the striping artifact as unlike the patient images.
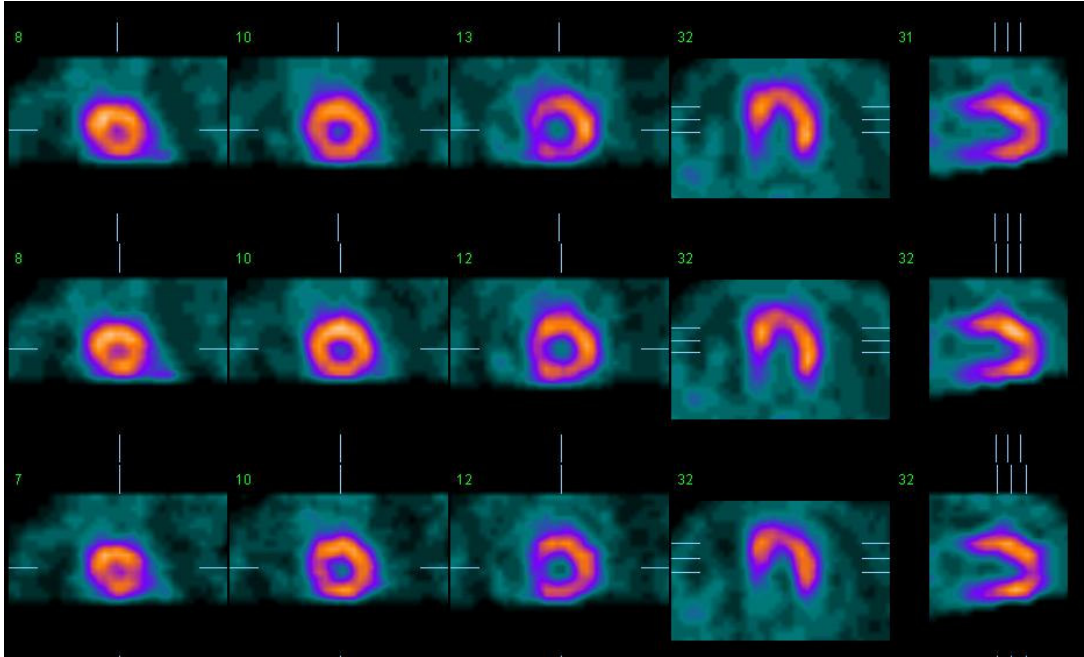
Figure 4.49: 'Slice' display mode in QGS comparing the OS3D-, OS4D- and RBM-reconstructed images for a severely hypokinetic moderately obese male phantom; this illustrates the average noise level. The OS3D and OS4D images are similar to one another, but in this case, the RBM image does not show the striping artifact as unlike the patient images.

4.3 Study of Physician Preference for Reconstruction Method

4.3.1 Preference Study

The physician preference study factored in the input of the 4 physicians into the evaluation of the reconstruction methods. Two to three one-hour sessions were scheduled with the physicians for completing the study over a two to three week period. The physicians were provided the patient's radiology report prior to the reading of each patient dataset in QGS, and reminded of the task at hand, which was to consider which of the images (from the 3 reconstruction methods) gave them the most confidence in the diagnosis. They were encouraged to make full use of the rating scale; however, it was noted that they were all reluctant to use the extremes of the scale (i.e. much worse and

much better). In several cases, the physicians were hard-pressed to decide which of the images was better, and opted to go with a rating of 0 (to indicate they were the same). Of all the display and analysis modes available in QGS, it was noted that they tended to choose either the 'Slice' or the 'Splash' modes as the basis of their diagnoses almost exclusively, perhaps because the display is most efficient in layout, displaying the VLA, HLA and SA slices simultaneously. They occasionally used the 'Blur' mode to smooth out the noise in the spatial dimension, and very rarely, the 'Smear' mode that did temporal smoothing. The physicians paid no attention to the calculated EDV, ESV, and EF values output by the QGS program.

In the low-noise situations, the physicians tended to rate the 3 methods as being 'the same', and sometimes preferred the OS-EM with 3D filtering or OS-EM with 4D filtering to the other methods. It is likely that they preferred the smoother appearance of the OS-EM images (spatially) to the RBI-MAP images when the images were not terribly degraded by noise. However, in high-noise datasets, when all 3 images displayed incompletely in QGS (with missing apices or other parts of the heart), they tended to choose the RBI-MAP method over the others. It is hypothesized that the smoother motion of the RBI-MAP might help the eye average the slices, even with the missing data, to provide a more complete picture of both the perfusion and motion information.

4.3.2 ANOVA

An analysis of variance helped determine if the population means among the physician ratings of the different reconstruction methods were different.
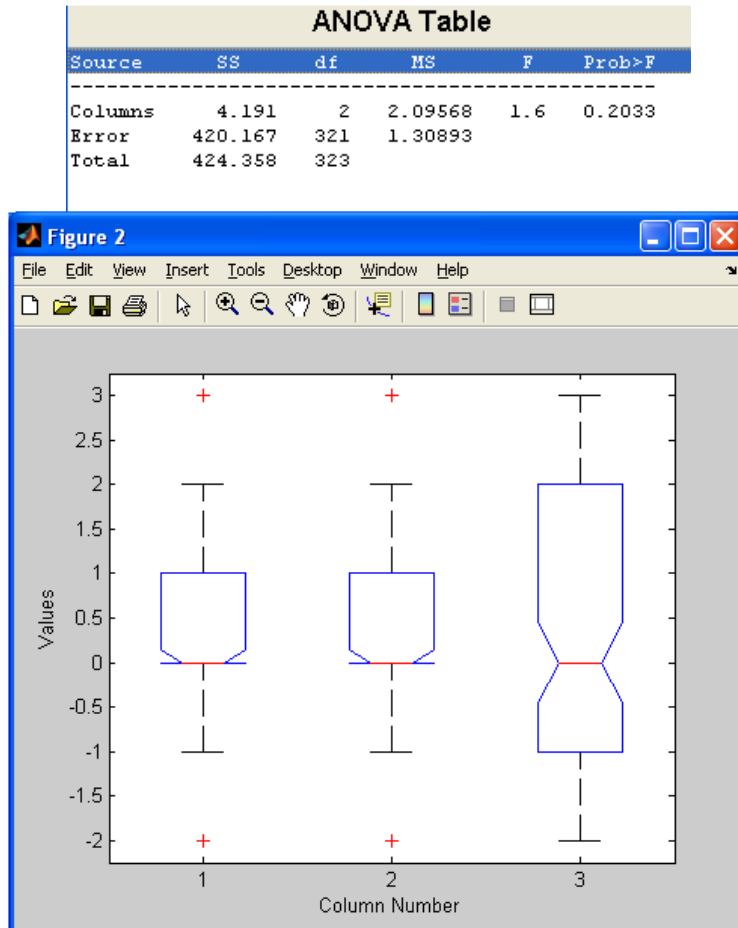
Figure 4.50: Results of the ANOVA exploring the differences between the ratings for the OS3D, OS4D and RBM methods (1, 2, 3, respectively). Group 1 shows the physician ratings comparing OS3D and OS4D, group 2 shows ratings between OS3D and RBM, while the last group compares the two 4D methods. The red lines depict the means of the groups, while the whisker lines lead to the 25th and 75th percentiles.

The one-way ANOVA performed in MATLAB yielded the results shown in Figure 4.50. The standard ANOVA table is seen, with columns displaying the source of variability, the sum of squares (SS) due to each source, the degrees of freedom (df) associated with each source, the mean squares (MS) for each source (which is the ratio SS/df), the F-statistic, which is the ratio of the mean squares, and finally, the p-value, which is derived from F. The p value is very high in this case, resulting in the conclusion that there is not a significant difference among the physican ratings for the 3 processing

methods. Thus, there is not enough reason to reject the null hypothesis. What this translates to, is that the physician preference study revealed no preference in particular for any of the three methods over the other.

From the plot showing the range of values for the 3 methods, it is apparent that the ratings comparing the OS-EM with 3D filtering and OS-EM with 4D filtering methods, and the ratings for the OS-EM with 3D filtering and RBI-MAP methods had similar means and smaller spreads than the ratings comparing the two 4D methods, where there was much more variance above and below the mean. The greater variation in the latter case is probably due to the response to the 4D images being more subjective, with ratings reflective of individual preference, and perhaps some variance on a case-by-case basis.

Chapter 5

Conclusions

This chapter attempts to tie in all the results from the studies in this dissertation, and draw conclusions from them. The goal of this project has been to evaluate 3D versus 4D reconstruction methods for reconstructing noisy gated SPECT images from obese patients, namely OS-EM with 3D filtering, OS-EM with 4D filtering, and the RBI-MAP algorithm employing different Gibbs priors for spatial and time domain smoothing.

5.1 Development of Obese Phantom Population

The first step toward the evaluation studies was the optimization of reconstruction parameters in an attempt to standardize the methods being compared. Blood pool SPECT images were simulated using an obese male phantom, and filter cutoffs with different iteration numbers of the OS-EM algorithm were tested for the 3D Gaussian filter and the 4D Butterworth filter. The prior weighting parameters and other parameters influencing the shape of the derivative potential functions of the RBI-MAP algorithm were evaluated simultaneously. The result was a set of filter cutoffs for the OS-EM method with 3D and 4D filters, and fixed parameters for the RBI-MAP algorithm, which allowed for some standardization despite the fact that it was not possible to select the most optimal set of parameters that would allow the methods to perform at their best under a given set of circumstances.

Patient data were collected from patients imaged with Tc-99m tetrofosmin in the clinic for the study database and the projection data were reconstructed. The data were used in conjunction with anthropomorphic data, and a duo of body sizes and organ sizes (primarily the heart, and breasts in the female) were chosen for the phantoms in the study. Motion defects were also created to simulate phantoms with left ventricle moving either at normal speed or one of two hypokinetic speeds. Noise levels assessed in the patients, were used to generate realistic noisy projection data from the phantoms for a total of three noise realizations per phantom, and reconstruction was performed using the 3 methods being evaluated in the study. Comparisons of patient data to phantom data revealed that the phantoms make for a realistic model of Tc-99m tetrofosmin uptake in obese patients, and would provide a solid vehicle for further studies.

5.2 Quantitative Accuracy and Motion Fidelity

The next step in the process involved the conversion of the reconstructed data from the .im format (which was used for reconstruction) to the standard DICOM format to enable the use of the clinical Quantitative Gated SPECT software (distributed by Cedars-Sinai and commonly used in the clinic) for the analysis of the images. Once this method was developed, the reconstructed images in the patient database and the phantom database were all converted to DICOM format and imported to the clinical workstations.

The quantitative parameters describing the function of the left ventricle, namely the end-diastolic volume, end-systolic volume and ejection fraction, were recorded for each of the sets of images for the patients and phantoms in the study. Analysis of the quantitative factors in the patient study suggested that there is a difference in 'population'

means when comparing the OS-EM with 3D filtering to OS-EM with 4D filtering, while OS-EM with 3D filtering seemed to be very similar to the RBI-MAP images. There were conflicting results comparing OS-EM with 4D filtering and RBI-MAP. OS-EM with 4D filtering stood out from the other two methods in the paired t-tests; it produced slightly more precise results. The qualitative analysis of the patient images did not uncover much at the lower noise level, where all three methods produced images that appeared similar in the QGS viewer spatially. When viewed in interleave mode, the images demonstrated smoother motion with the RBI-MAP algorithm as compared to the OS-EM methods, but this was a subtle difference. At higher noise levels that caused portions of the heart to be missing, the OSEM 3D- and 4D-filtered images appeared similar to one another and smoother than the RBI-MAP image which demonstrated a striping artifact thought to be caused by the weighting of the spatial prior. The heart motion appeared smoother and more realistic with the RBI-MAP algorithm once again.

The results from the phantom study revealed that QGS tends to severely underestimate the EDV parameter, thus also affecting the EF value calculated by the algorithm in the software. QGS performed better at estimating ESV, possibly due to the easier identification of the endocardial and epicardial LV surfaces with higher counts concentrated in the heart region at end-systole. QGS, while providing the user the option of manually correcting the fit of the epicardial contours, does not allow the same for the fit to the endocardial surface. This limits the ability of the user to improve quantitation in QGS.

Other analyses on the phantom study data revealed that, on average, the EDV, ESV and EF values calculated by QGS for each of the three methods were very similar to

91

each other (across methods and across populations), though it was noted that the EF values calculated for the RBI-MAP reconstructed-images were slightly lower while the OS-EM with 3D filtering method appeared to have slightly greater accuracy than the other two methods at estimating the quantitative parameters. It is thought that this is due to the differing noise structures between the OS-EM and the RBI-MAP reconstructed images, which can affect the identification of the LV surfaces by QGS.

Paired t-tests on the phantom data, again calculated for the different populations (classified by physiological states) yielded interesting results. It appeared that for the hypokinetic populations, there are no significant differences in EDV, ESV, and EF values among reconstruction methods, unlike in the normal population. The results suggest that for those obese patient populations who are normal or borderline diseased, the choice of reconstruction method may make a greater difference. As in the patient study, the OS-EM method with 4D filtering stood out from the other two methods.

Visually, the images compared similarly as in the patient study. However, no striping artifact as in the case of the RBI-MAP reconstructed patient images, were seen in the phantom study. This is due to the optimization of the RBI-MAP parameters for the noise level selected for the phantom study, while the patient study illustrated the performance of that algorithm under very different noise condition.

5.3 Physician Preference for Reconstruction Method

The images in the patient database were masked as to the method of reconstruction, and read by 4 physicians who participated in a preference study that set out to evaluate which of the methods provided images that gave them the most

confidence in their diagnoses. While the ANOVA technique analyzing the results of this preference study indicated that there was no method that was preferred over the other by the physicians, the mechanics of doing the study with the experts was revealing. Reinforcing the results of the prior studies, it was found that the physicians were hard-pressed in low-noise cases to choose one method over another (due to their similar appearance), and in several such cases, they actually preferred the OS-EM images with 3D or 4D filters to the RBI-MAP ones. This may well be due to their preference for images they are used to working with on a regular basis (as OS-EM with the 3D Gaussian filter is frequently employed in the clinic). It is also possible that in doing a controlled study of this nature (where the physicians were not provided the projection data nor the ungated data they compare the gated datasets to while reading the cases in the clinic), the emphasis was subtly shifted from the temporal value of the methods to the spatial appearance and smoothness of the images, until a high-noise case shifted the emphasis back. In such cases, they generally tended to prefer the RBI-MAP method for its smoother motion that seems able to make up for the missing image content despite the spatial artifacts, due to temporal averaging by the eye. This theory would have to be tested further with psychophysical studies, to be substantiated.

5.4 Concluding Remarks

This dissertation was a foray into the complexities surrounding the type of reconstruction method that would be the best choice for processing noisy images from gated cardiac SPECT studies in obese patients. It revealed that the choice of reconstruction method may affect the images of patients who are normal or borderline

hypokinetic much more than patients who are further along in disease stage. The results of the patient and phantom study lead us to conclude that the OS-EM method with 4D filtering may make the greatest difference to the quantitation of LV chamber volumes, as compared to the other methods. However, it is clear that the RBI-MAP method brings very different advantages into the mix as compared to the other methods. The preference study indicated that though there was no clear preference for one method over the other, that the response to the 4D algorithms was very subjective, and highly variable as compared to the response to the OS-EM methods.

Further work should aim to explore this in more detail. A pilot observer study would be of benefit in optimizing parameters native to the reconstruction methods, in the interests of comparing the best performing incarnation of each one to the others, as opposed to selecting parameters that may place one or more methods at a disadvantage. The RBI-MAP algorithm parameters in particular should be optimized for various noise levels. A motion observer study utilizing those parameters and methods might then provide concrete answers to the question of which processing method will provide the physician of the obese patient with the best tools for diagnosis and treatment planning, ultimately improving the patient prognosis.

Chapter 6

Appendix A

MATLAB CONVERSION CODE (DICOM TO .IM)

```
function return_value = Convert_dcm_to_im()

% Converts a 4D 16 frame DICOM fileset to a series of .im files (16, one for
% each frame of the cardiac cycle)

% Read the DICOM fileset
image = dicomread('Pat9.strs.prj.dcm');

% Convert to single precision:
image2 = single(image);

% Reshape into 32 views and 32 gates-cameras:
image2 = reshape(image2, 64, 64, 32, 32);

% Split into cameras:
cam1 = image2(:, :, :, 1:16);
cam2 = image2(:, :, :, 16:32);

% Combine cameras and frames by concatenating in the proper direction:
for i = 1:16
    frame (:,:,:,i) = cat(3, cam1(:,:,:,i), cam2(:,:,:,i));
end

% Compose filenames and write out in .im format:
for i = 1:16
    writeimfile(frame(:,:,:,i), strcat('Pat9.strgtd.prj.',num2str(i)));
end

return_value=0;
return
```

MATLAB CONVERSION CODE (.IM TO DICOM)

```
function return_value = Convert_im_to_dicom(im_input, dicom_prefix, output_prefix)

% Converts a 3D .im file to a DICOM fileset by borrowing header
%  from an existing DICOM fileset

% Read the input image
```

```matlab
image = readimfile(im_input);

% Find number of slices (z * t)
numslices = size(image,3);

% Convert to 16-bit array
image2 = int16(image);

% Get dicom info fields
info = dicominfo([dicom_prefix,'.dcm']);

% Find header length
header_length = info.StartOfPixelData + 12;

% Open dicom file
filein = fopen([dicom_prefix,'.dcm'],'r');

% Read header
header = fread(filein, header_length, 'uint8');

% Close file
fclose(filein);

% Open output file
fileout = fopen([output_prefix,'.dcm'],'w');

% Write header
count = fwrite(fileout, header, 'uint8');
if (count ~= header_length)
  error('Problem writing header in Convert_im_to_dicom');
end

% For each slice
for i = 1:numslices

  % Extract the slice and transpose
  imagetemp = image2(:,:,i);

  % Write pixels
  count = fwrite(fileout, image2(:,:,i)', 'int16');
  if (count ~= prod(size(image(:,:,i))))
    error('Problem writing pixels in Convert_im_to_dicom');
  end

end
```

```
% Close file
fclose(fileout);

return_value=0;
return
```

References

1.   Baur L. Evaluation of left ventricular function: does the imaging technique matter? *Intl J Cardiovasc Imag.* 2008-12-01 2008;24(8):803-805.

2.   Beekman F, Slijpen E, and Niessen W. Selection of task-dependent diffusion filters for the post-processing of SPECT images. *Phys Med Biol.* 1998;43(6):1713-1730.

3.   Berman D, Kang X, Nishina H, Slomka P, Shaw L, Hayes S, Cohen I, Friedman J, Gerlach J, and Germano G. Diagnostic accuracy of gated Tc-99m sestamibi stress myocardial perfusion SPECT with combined supine and prone acquisitions to detect coronary artery disease in obese and nonobese patients. *Journal of Nuclear Cardiology.* March-April 2006;13(2):191-201.

4.   Bigaard J, Tjonneland A, Thomsen B, Overvad K, Heitmann B, and Sorensen T. Waist circumference, BMI, smoking, and mortality in middle-aged men and women. *Obesity Research.* 2003;11(7):895-903.

5.   Brankov J, Yang Y, and Wernick M. Spatiotemporal processing of gated cardiac SPECT images using deformable mesh modeling. *Med Phys.* 2005;32(9):2839-2949.

6.   Cacciabaudo J, and Szulc M. Gated Cardiac SPECT: Has the addition of function to perfusion strengthened the value of myocardial perfusion imaging? *J Nucl Med.* 2001;42(7):1050-1052.

7.   Cao Z, Gilland D, Mair B, and Jaszczak R. Three-dimensional motion estimation with image reconstruction for gated cardiac ECT. *IEEE Trans Nucl Sci.* 2003;50(3):384-388.

8.   Cherry S, Sorenson J, and Phelps M. *Physics in Nuclear Medicine*. 3rd ed. ed. Philadelphia, PA: Saunders; 2003.

9.   Committee TDS. Strategic Document. Version 8.1 ed; 2008.

10.   Defrise M, and Gullberg G. Image reconstruction. *Phys Med Biol.* 2006;51:R139-R154.

11.   Devi S, Clackdoyle R, and Christian P. Torso and heart dimensions of cardiac SPECT patients. Paper presented at: IEEE Nuclear Science Symposium, 1997.

12.   Duvall W, Croft L, Corriel J, Einstein A, Fisher J, Haynes P, Rose R, and Henzlova M. SPECT myocardial perfusion imaging in morbidly obese patients: image quality, hemodynamic response to pharmacologic stress, and diagnostic and prognostic value. *J Nucl Cardiol.* 2006;13(2):202-209.

13.   Faber T, Cooke C, Folks R, Vansant J, Nichols K, DePuey E, Pettigrew R, and Garcia E. Left Ventricular Function and Perfusion from Gated SPECT Perfusion Images: An Integrated Method. Vol 40; 1999:650-659.

14.   Farncombe T, Feng B, King M, and Leppo J. Investigating acquisition protocols for gated, dynamic myocardial imaging in PET and SPECT. *IEEE Nuclear Science Symposium and Medical Imaging Conference*. Rome, Italy; 2004.

15.   Ficaro E, Quaife R, Kritzman J, and Corbett J. Accuracy and reproducibility of 3D-MSPECT for estimating left ventricular ejection fraction in patients with severe perfusion abnormalities [abstract]. *Circulation.* 1999;100(suppl):126.

16.   Ficaro EP, Fessler JA, Shreve PD, Kritzman JN, Rose PA, and Corbett JR. Simultaneous Transmission/Emission Myocardial Perfusion Tomography : Diagnostic Accuracy of Attenuation-Corrected 99mTc-SestamibiSingle-Photon Emission Computed Tomography. Vol 93; 1996:463-473.

17.   Florack L. /usr/image. Chapel Hill, NC: University of North Carolina at Chapel Hill; 2007:1-36.

18.   Germano G, Erel J, Lewin H, Kavanagh P, and Berman D. Automatic quantitation of regional myocardial wall motion and thickening from gated Technetium-99m sestamibi myocardial perfusion single-photon emission computed tomography. *J Am Coll Cardiol.* 1997;30(5):1360-1367.

19.   Germano G, Kavanagh P, Slomka P, Van Kriekinge S, Pollard G, and Berman D. Quantitation in gated perfusion SPECT imaging: the Cedars-Sinai approach. *J Nucl Cardiol.* 2007;14(4):433-454.

20.   Germano G, Kiat H, Kavanagh P, Moriel M, Mazzanti M, Su H, VanTrain K, and Berman D. Automatic quantification of ejection fraction from gated myocardial perfusion SPECT. *J Nucl Med.* 1995;36(11):2138-2147.

21.   Gilland D, Tsui B, McCartney W, Perry J, and Berg J. Determination of the optimum filter function for SPECT imaging. *J Nucl Med.* 1988;29:643-650.

22.   Go V, Bhatt M, and Hendel R. The diagnostic and prognostic value of ECG-gated SPECT myocardial perfusion imaging. *J Nucl Med.* 2004;45:912-921.

23.   Good W, Sumkin J, Dash N, Johns C, Zuley M, Rockette H, and Gur D. Observer sensitivity to small differences: a multipoint rank-order experiment. *Am J Roentgenology.* 1999;173:275-278.

24.   Gravier E, and Yang Y. Motion-compensated reconstruction of tomographic image sequences. *IEEE Trans Nucl Sci.* 2005;52(1):51-55.

25.   Gravier E, Yang Y, King M, and Jin M. Fully 4D motion-compensated reconstruction of cardiac SPECT images. *Phys Med Biol.* 2006;51:4603-4619.

26.   Green P. Bayesian reconstruction from emission tomography data using a modified EM algorithm. *IEEE Trans Med Imag.* 1990;9(1):84-93.

27.   Gremillet E, Champailler A, and Soler C. Fourier temporal interpolation improves electrocardiograph-gated myocardial perfusion SPECT. *J Nucl Med.* 2005;46:1769-1774.

28.   Hansen CL, Woodhouse S, and Kramer M. Effect of patient obesity on the accuracy of thallium-201 myocardial perfusion imaging. *The American Journal of Cardiology.* 2000;85(6):749-752.

29.   Hendee W, and Ritenour R. *Medical Imaging Physics*. 3rd ed. ed. St. Louis, MO: Mosby - Year Book, Inc.; 1992.

30.   Higley B, Smith FW, Smith T, Gemmell HG, Gupta PD, Gvozdanovic DV, Graham D, Hinge D, Davidson J, and Lahiri A. Technetium-99m-1,2-bis[bis(2-Ethoxyethyl) Phosphino]Ethane: Human Biodistribution, Dosimetry and Safety of a New Myocardial Perfusion Imaging Agent. Vol 34; 1993:30-38.

31.   Hudson H, and Larkin R. Accelerated image reconstruction using ordered subsets of projection data. *IEEE Trans Med Imag.* 1994;13(4):601-609.

32.   Iskandrian A, Germano G, VanDecker W, Ogilby J, Wolf N, Mintz R, and Berman D. Validation of left ventricular volume measurements by gated SPECT 99mTc-labeled sestamibi imaging. *J Nucl Cardiol.* 1998;5(6):574-578.

33.   Jain D. Technetium-99m labeled myocardial perfusion imaging agents. *Sem Nucl Med.* 1999;29:221-236.

34.   Kadrmas D, and Gullberg G. 4D maximum *a posteriori* reconstruction in dynamic SPECT using a compartmental model-based prior. *Phys Med Biol.* 2001;46(5):1553-1574.

35.   Kapur A, Latus K, Davies G, Dhawan R, Eastick S, Jarritt P, Roussakis G, Young M, Anagnostopoulos C, Bomanji J, Costa D, Pennell D, Prvulovich E, Ell P, and Underwood S. A comparison of three radionuclide myocardial perfusion tracers in clinical practice: the ROBUST study. *Eur J Nucl Med Mol Imag.* 2002;29(12):1608-1616.

36.   Keeping E. *Introduction to Statistical Inference*. Mineola, NY: Dover Publications, Inc.; 1995.

37.   Kelly JD, Forster AM, Higley B, Archer CM, Booker FS, Canning LR, Chiu KW, Edwards B, Gill HK, McPartlin M, Nagle KR, Latham IA, Pickett RD, Storey AE, and

Webbon PM. Technetium-99m-Tetrofosmin as a New Radiopharmaceutical for Myocardial Perfusion Imaging. Vol 34; 1993:222-227.

38. Lalush D, Frey E, and Tsui B. Fast maximum entropy approximation in SPECT using the RBI-MAP algorithm. *IEEE Trans Med Imag.* 2000;19(4):286-294.

39. Lalush D, Jatko M, and Segars W. An observer study methodology for evaluating detection of motion abnormalities in gated myocardial SPECT. *IEEE Trans Biomed Engg.* 2005;52(3):480-485.

40. Lalush D, Segars W, and Tsui B. A unified approach to 4D gated myocardial SPECT reconstruction. Paper presented at: IEEE Nuclear Science Symposium and Medical Imaging Conference, 1999; Seattle, WA.

41. Lalush D, and Tsui B. Simulation evaluation of Gibbs prior distributions for use in maximum *a posteriori* SPECT reconstructions. *IEEE Trans Med Imag.* 1992;11(2):267-275.

42. Lalush D, and Tsui B. Space-time Gibbs priors applied to gated SPECT myocardial perfusion studies. *Three-dimensional Image Reconstruction in Radiology and Nuclear Medicine*; 1996:209-226.

43. Lalush D, and Tsui B. Block-iterative techniques for fast 4D reconstruction using *a priori* motion models in gated cardiac SPECT. *Phys Med Biol.* 1998;43:875-887.

44. Lalush D, and Tsui B. Mean-variance analysis of block-iterative reconstruction algorithms modeling 3D detector response in SPECT. *IEEE Trans Nucl Sci.* 1998;45(3):1280-1287.

45. Lalush D, and Tsui B. Performance of ordered-subset reconstruction algorithms under conditions of extreme attenuation and truncation in myocardial SPECT. *J Nucl Med.* 2000;41(4):737-744.

46. Lange K, and Carson R. EM reconstruction algorithms for emission and transmission tomography. *J Comp Asst Tomography.* 1984;8(2):306-316.

47. Larsson A, Mo S, Sundstrom T, and Riklund K. Gaussian prefiltering of 123I DAT SPECT images when using depth-independent resolution recovery. *Phys Med Biol.* 2007;52(18):N393-399.

48. Lavie CJ, and Milani RV. Obesity and cardiovascular disease: the hippocrates paradox? *Journal of the American College of Cardiology.* 2003;42(4):677-679.

49. Lee T-S, and Tsui BMW. Evaluation of a 4D MAP-RBI-EM Image Reconstruction Method for Gated Myocardial SPECT using a Human Observer Study. *World Congress on Medical Physics and Biomedical Engineering 2006*; 2007:1663-1666.

50. Lee T, Segars W, and Tsui B. A study of the effect of cardiac gating in myocardial SPECT using the 4D NCAT. *IEEE Nuclear Science Symposium and Medical Imaging Conference*. Portland, OR; 2003.

51. Lee T, Segars W, and Tsui B. Application of 4D MAP-RBI-EM with space-time Gibbs priors to gated myocardial SPECT. *J Nucl Med.* 2005;46:162P.

52. Lee T, Segars W, and Tsui B. Study of parameters characterizing space-time Gibbs priors for 4D MAP-RBI-EM in gated myocardial perfusion SPECT. *IEEE Nuclear Science Symposium and Medical Imaging Conference*. Fajardo, Puerto Rico; 2005.

53. Lee T, Segars W, and Tsui B. The development and application of a realistic simulation dataset for simultaneous cardiac and respiratory gated ECT/CT. *IEEE Nuclear Science Symposium and Medical Imaging Conference*. Honolulu, HI; 2007.

54. Lima RSL, Watson DD, Goode AR, Siadaty MS, Ragosta M, Beller GA, and Samady H. Incremental value of combined perfusion and function over perfusion alone by gated SPECT myocardial perfusion imaging for detection of severe three-vessel coronary artery disease. *Journal of the American College of Cardiology.* 2003;42(1):64-70.

55. Links J, DePuey E, Taillefer R, and Becker L. Attenuation correction and gating synergistically improve the diagnostic accuracy of myocardial perfusion SPECT. *J Nucl Cardiol.* 2002;9(2):183-187.

56. Manka-Waluch A, Palmedo H, Reinhardt M, Joe A, Manka C, Guhlke S, Biersack H, and Bucerius J. Myocardial uptake characteristics of three 99mTc-labeled tracers for myocardial perfusion imaging one hour after rest injection. *Ann Nucl Med.* 2006;20(10):663-670.

57. Manson JE, and Bassuk SS. Obesity in the United States: A Fresh Look at Its High Toll. Vol 289; 2003:229-230.

58. Marie P, Djaballah W, Franken P, Vanhove C, Muller M, Boutley H, Poussier S, Olivier P, Karcher G, and Bertrand A. OSEM reconstruction, associated with temporal Fourier and depth-dependant resolution filtering, enhances results from sestamibi and 201Tl 16-interval gated SPECT. *J Nucl Med.* 2005;46:1789-1795.

59. Montgomery D. *Design and Analysis of Experiments*. 4th ed. ed. New York, NY: John Wiley & Sons, Inc.; 1997.

60. Motulsky H. *Intuitive Biostatistics*. New York, NY: Oxford University Press; 1995.

61. Nakajima K, Higuchi T, Taki J, Kawano M, and Tonami N. Accuracy of Ventricular Volume and Ejection Fraction Measured by Gated Myocardial SPECT: Comparison of 4 Software Programs. Vol 42; 2001:1571-1578.

62. Nakajima K, Kusuoka H, Nishimura S, Yamashina A, and Nishimura T. Normal limits of ejection fraction and volumes determined by gated SPECT in clinically normal patients without cardiac events: a study based on the J-ACCESS database. *Eur J Nucl Med Mol Imag.* 2007;34:1088-1096.

63. Nakajima K, and Nishimura T. Inter-institution preference-based variability of ejection fraction and volumes using quantitative gated SPECT with 99mTc-tetrofosmin: a multicentre study involving 106 hospitals. *Eur J Nucl Med Mol Imag.* 2006;33(2):127-133.

64. Nakajima K, Taki J, Higuchi T, Kawano M, Taniguchi M, Maruhashi K, Sakazume S, and Tonami N. Gated SPET quantification of small hearts: mathematical simulation and clinical application. *Eur J Nucl Med.* 2000;27:1372-1379.

65. Narayanan M, King M, Pretorius P, Dahlberg S, Spencer F, Simon E, Ewald E, Healy E, MacNaught K, and Leppo J. Human-observer receiver-operating characteristic evaluation of attenuation, scatter, and resolution compensation strategies for (99m)Tc myocardial perfusion imaging. *J Nucl Med.* 2003;44(11):1725-1734.

66. Narayanan M, King M, Soares E, Byrne C, Pretorius P, and Wernick M. Application of the Karhunen-Loeve Transform to 4D Reconstruction of Cardiac Gated SPECT Images. *IEEE Nuclear Science Symposium and Medical Imaging Conference.* Seattle, WA; 1999.

67. Narayanan M, King M, Wernick N, Byrne C, Soares E, and Pretorius P. Improved image quality and computation reduction in 4-D reconstruction of cardiac-gated SPECT images. *IEEE Trans Med Imag.* 2000;19(5):423-433.

68. Orlov SS. Theory of three dimensional reconstruction. I. Conditions for a complete set of projections. *Sov Phys Crystallogr.* 1975;20(3):312-314.

69. Paeng JC LD, Cheon GJ, Lee MM, Chung JK, and MC Lee. Reproducibility of an automatic quantitation of regional myocardial wall motion and systolic thickening on gated 99mTc-sestamibi myocardial SPECT. *J Nucl Med.* 2001;42(5):695-700.

70. Paul A, and Nabi H. Basic principles, technical aspects, and clinical applications. *J Nucl Med Technol.* 2004;32(4):179-187.

71. Perault C LA, Liehn JC, Wampach H, Gibold C, Ouzan J, Pron T, Fortier A, and A Bouchard. Quantitative comparison of prone and supine myocardial SPECT MIBI images. *Clin Nucl Med.* 1995;20(8):678-684.

72. Pfisterer ME BA, and BL Zaret. Range of normal values for left and right ventricular ejection fraction at rest and during exercise assessed by radionuclide angiography. *Eur Heart J.* 1985;6:647-655.

73. Pheasant S. *Bodyspace: Anthropometry, Ergonomics and the Design of Work.* 2nd ed. ed. Bristol, PA: Taylor & Francis; 1996.

74. Pisano ED CE, Major S, Zong S, Hemminger BM, Muller KE, Johnston RE, Walsh R, Conant E, Fajardo LL, Feig SA, Nishikawa RM, Yaffe RJ, Williams MB, and SR Aylward. Radiologists' preferences for digital mammographic display. *Radiology.* 2000;216:820-830.

75. Prvulovich E. Myocardial perfusion scintigraphy. *Clin Med.* 2006;6(3):263-266.

76. Reyes E LC, Harbinson M, Rahman S, Prvulovich E, Ell PJ, Anagnostopoulos C, and SR Underwood. A comparison of Tl-201, Tc-99m sestamibi, and Tc-99m tetrofosmin myocardial perfusion scintigraphy in patients with mild to moderate coronary stenosis. *J Nucl Cardiol.* 2006;13(4):488-494.

77. Schaefer WM LC, Nowak B, Kaiser H, Reinartz P, Buecker A, Kromback GA, Buell U, and HP Kuhl. Validation of QGS and 4D-MSPECT for quantification of left ventricular volumes and ejection fraction from gated 18F-FDG PET: Comparison with cardiac MRI. *Journal of Nuclear Medicine.* 2004;45:75-79.

78. Schaefer WM, Lipke CSA, Standke D, Kuhl HP, Nowak B, Kaiser H-J, Koch K-C, and Buell U. Quantification of Left Ventricular Volumes and Ejection Fraction from Gated 99mTc-MIBI SPECT: MRI Validation and Comparison of the Emory Cardiac Tool Box with QGS and 4D-MSPECT. Vol 46; 2005:1256-1263.

79. Sciagra R. The expanding role of left ventricular functional assessment using gated myocardial perfusion SPECT: the supporting actor is stealing the scene. *Eur J Nucl Med Mol Imag.* 2007;34:1107-1122.

80. Segars W. *Development of a new dynamic NURBS-based cardiac-torso (NCAT) phantom.* Chapel Hill, NC: Biomedical Engineering Department, University of North Carolina at Chapel Hill; 2001.

81. Segars W, Lalush D, and Tsui B. Modeling respiratory mechanics in the MCAT and spline-based phantoms. *IEEE Trans Nucl Sci.* 2001;48(1):89-97.

82. Sheng J, and Ying L. A fast image reconstruction algorithm based on penalized-likelihood estimate. *Med Eng Phys.* 2005;27:679-686.

83. Shepp L, and Vardi Y. Maximum likelihood reconstruction for emission tomography. *IEEE Trans Med Imag.* 1982;1:113-122.

84. Slomka PJ NH, Berman DS, Kang X, Akincioglu C, Friedman JD, Kayes SW, Aladl UE, and G Germano. "Motion-frozen" display and quantitation of myocardial perfusion. *J Nucl Med.* 2004;45(7):1128-1134.

85. Sorenson J, and Phelps M. *Physics in Nuclear Medicine*. 2nd ed. ed. New York, NY: Grune&Stratton, Inc.; 1987.

86. Takahashi N, Reinhardt CP, Marcel R, and Leppo JA. Myocardial Uptake of 99mTc-Tetrofosmin, Sestamibi, and 201Tl in a Model of Acute Coronary Reperfusion. Vol 94; 1996:2605-2613.

87. Tonge CM AI, Arumugam P, James JM, Al-Bahraini GI, Lawson RS, Shields RA, and MC Prescott. Changes in the appearance of attenuation artefacts due to change in posture in myocardial perfusion imaging. *Nucl Med Commun.* 2008;29(5):441-447.

88. Utsunomiya D TS, Awai K, Shiraishi S, Nakaura T, and Y Yamashita. Multidetector-row CT and quantitative gated SPECT for the assessment of left ventricular function in small hearts: the cardiac physical phantom study using a combined SPECT/CT system. *Eur Radiol.* 2006;16:1818-1825.

89. Vanhove C FP, Defrise M, Deconinck F, and A Bossuyt. Reconstruction of gated myocardial perfusion SPET incorporating temporal information during iterative reconstruction. *Eur J Nucl Med Mol Imag.* 2002;29(4):465-472.

90. Veress AI SW, Weiss JA, Tsui BM, and GT Gullberg. Normal and pathological NCAT image and phantom data based on physiologically realistic left ventricle finite-element models. *IEEE Trans Med Imag.* 2006;25(12):1604-1616.

91. Wang W, and Gindi G. Noise analysis of MAP-EM algorithms for emission tomography. *Phys Med Biol.* 1997;42(11):2215-2232.

92. Wells RG KM, Gifford HC, and PH Pretorius. Single-slice versus multi-slice display for human-observer lesion-detection studies. *IEEE Trans Med Imag.* 2000;47(3):1037-1044.